UNIVERSITY OF NAPLES FEDERICO II

UNIVERSITY OF BERGAMO

Ph.D. Program in

Technology, Innovation and Management (TIM)

XXXVIII Cycle

SSD: ING-IND/05 Aerospace Equipments and Systems

Exploring Edge Surveillance Solutions for Technology Innovation in Advanced Air Mobility

Ph.D. Advisors

Chiar.mo Prof. Domenico Accardo

Chiar.mo Prof. Antonio De Maio

Ph.D. Candidate

Fausta Mattei

ID:1086483

Ph.D. Course Coordinator

Chiar.mo Prof. Paolo Gaiardelli

Blank Page

Abstract

The rapid proliferation of Unmanned Aerial Systems, commonly named as drones, and the emergence of Urban and Advanced Air Mobility concepts have fundamentally transformed the contemporary aviation landscape. Originally conceived for military applications, drones have evolved into versatile platforms deeply integrated within civil, industrial, and societal frameworks, generating unprecedented challenges in safety assurance, security protocols, and surveillance capabilities. The existing communication, navigation, and surveillance infrastructures, architecturally designed for high-altitude and low-density air traffic operations, prove inadequate for the dense, low-altitude operational paradigms anticipated in future urban environments. This paradigmatic shift necessitates the development of innovative, adaptive, and edge-capable surveillance solutions that ensure resilient and sustainable integration of heterogeneous manned and unmanned traffic flows.

This dissertation systematically addresses the multifaceted challenges through the investigation of multi-layered detection solutions, with particular emphasis on radar-based systems and cooperative multi-agent detection approaches. Central to this research is the comprehensive analysis of radar cross-section characteristics across conventional and unmanned platforms, substantiated through rigorous simulation studies and extensive experimental validation campaigns. The investigation encompasses both passive and active enhancement strategies designed to optimize drone detectability within complex urban environments characterized by electromagnetic interference, multipath propagation, and adverse meteorological conditions.

Beside technological contributions, this research adopts an interdisciplinary approach by integrating socio-economic perspectives through innovation and entrepreneurship pathways, demonstrating how advanced surveillance technologies can serve as catalysts for regional economic development and environmental sustainability. The work also incorporates applied case studies, notably UAS-based environmental monitoring in high-risk geological contexts such as the Campi Flegrei bradyseismic area, effectively illustrating both the operational potential and

the regulatory complexities of surveillance-dependent missions. Another case study is the multi-agent cooperative detection system, which involves the development and testing of a cooperative framework composed of drones and ground robots for the autonomous detection and interception of targets in semi-structured urban environments.

The research culminates in a comprehensive theoretical and practical framework that synthesizes advanced modeling techniques, experimental validation methodologies, and socio-technical innovation strategies. This integrated approach contributes significantly to the foundational knowledge required for the safe, efficient, and sustainable deployment of Advanced Air Mobility solutions within the emerging paradigm of smart urban environments, establishing a pathway toward the harmonious coexistence of diverse aerial mobility solutions in future metropolitan contexts.

Keywords: *Advanced Air Mobility, Drone Surveillance, Radar Cross Section , Unmanned Aerial Systems,*

List of Contents

1. Introduction 18

1.1. UAV Classification 20

1.2. Research objectives and framework 22

2. Advanced Air Mobility Systems and Surveillance Requirements 24

2.1. The Paradigm Shift Toward Advanced Air Mobility 24

2.1.2. Technological Convergence and Innovation Drivers 29

2.2. Surveillance Systems in Urban Air Mobility and Advanced Air Traffic Management 30

2.3. Drone Detection and Radar-Cross Section issues 34

2.3.1. Signal-to-Noise Ratio Impact and Detection Range Constraints . 35

3. Pathways to Innovation and Entrepreneurship 37

3.1. Structure of Training Activities 38

3.1.1. Transatlantic Collaboration: New York Summer School. 39

3.2. Innovation Challenges in the Campania Region 40

3.3. Case Study: Technological Innovation and Sustainability in Irpinia DOCG Regions 42

3.3.1. Integrated Technological Solution Framework 45

3.3.2. Socio-Economic Impact Assessment Framework 49

3.4. case study outcomes 49

4. Radar-Cross Section Analysis: Theoretical Framework and Simulation Studies 51

4.1. Theoretical Framework 52

4.2. Methodology and Simulation Setup 54

4.2.1. POFACETS 54

4.2.2. F-35 Aircraft Model and Simulation Configuration 56

4.2.3. Statistical analyses by moment matching 63

4.3. Results and Statistical Analysis 65

5. Multi-Platform Detection Systems Simulation: 75

5.1. System Architecture and Design Framework 76

5.1.1. Architecture Selection: Centralized vs Decentralized 76

5.1.2. System Design Overview 80

5.1.3. BlueSky ATC Simulator Platform 81

5.2. Experimental Setup and Implementation Framework 82

5.2.1. Phase 1 Implementation: Plugin Development and Scenario Configuration 86

5.2.2. Trajectory Implementation 87

5.2.3. Radar Plugin Development 91

5.2.4. Acoustic Sensor Plugin Implementation 96

5.2.5. Simulation Scenario 101

6. Experimental Validation: Real-world Drone Detection and RCS Characterization 104

6.1. Overview 106

6.1.1. Factors Influencing Radar Cross Section 106

6.1.2. *Radar Cross Section Estimation Procedure* 107

6.1.3. *FMCW Radar Systems* 108

6.1.4. *Experimental Setup and Methodology* 110

6.1.5. *Results and Discussion* 116

6.1.6. *X- Band Results* 116

6.1.7. *L-Band Results* 120

6.1.8. *Cramér-von Mises Distance Analysis* 124

6.1.9. *Comparative Analysis of RCS behavior in X- and L-Band* 131

6.2. Experimental Test Results 133

7. RCS Enhancement Strategies: Passive and Active Systems 134

7.1. RCS Enhancement Solutions 134

7.1.1. *Advantages and Disadvantages both of Active and Passive solutions* 136

7.2. Experimental Setup and Methodology: Passive System 137

7.3. Passive System Radar Configuration 139

7.3.1. *Passive Tests Protocol* 141

7.4. Passive System Results 143

7.5. Experimental Setup and Methodology: Active System 146

7.5.1. *Active System Principle for RCS Estimation* 149

7.5.2. Software Defined Radio Principle 150

7.5.3. Results with Active System 151

8. Cooperative Multi-Agent System for Autonomous Detection of Target in Semi-Structured Urban Environments 154

8.1. Swarm Robotic Systems 154

8.2. Experimental Setup 157

8.2.1. Team 158

8.3. Methodology and Work 160

8.3.3. Phase 1: Autonomous Exploration 162

8.3.4. Phase 2: Multi-Modal Cooperative Target Engagement 163

8.3.5. Phase 3: Dynamic Target Interception 164

8.4. Final Consideration 165

9. Case Study: Surveillance-Dependent Operations in Campi Flegrei Area 167

9.1. Background and Regulatory Framework 168

9.2. Equipment Configuration 170

9.3. Navigation Challenges in Urban Surveillance Operations 173

9.3.2. Urban Geometry Classification for Error Analysis 176

9.4. Case Study Analysis: Positioning Accuracy in Case VIII Urban Configuration 179

10. Conclusion 183

LIST OF FIGURES

FIGURE 1. PROJECT LOGICAL FRAMEWORK. 45

FIGURE 2. HYDROGEL APPLICATION METHODOLOGY. 48

FIGURE 3. EXAMPLE OF DEPLOYMENT OF DRONES SPRAYING HYDROGELS ONTO LEAVES. 48

FIGURE 4. POFACETS V4.5 MAIN SCREEN. 55

FIGURE 5. REFERENCE SYSTEM (SUBPLOT A) AND X-Y VIEW (SUBPLOT) OF THE F-35 OVERLAPPED WITH THE POLAR PLOT OF ITS RCS IN DBSM. THE RCS IS EVALUATED FOR ELEVATION ANGLES IN THE INTERVAL [98, 100] DEGREES AND AT AN L-BAND OPERATING FREQUENCY OF 1 GHZ. 57

FIGURE 6. RCSS (DBSM) (BLUE LINE) AND ITS MEAN VALUE (RED LINE) VERSUS AZIMUTH (IN DEGREES) OF THE F-35 AIRCRAFT, FOR THE THREE CONSIDERED FREQUENCY BAND (I.E., VHF, L, AND X, FROM TOP TO BOTTOM) UNDER THE SR REGIME. 60

FIGURE 7. RCSS (DBSM) (BLUE LINE) AND ITS MEAN VALUE (RED LINE) VERSUS AZIMUTH (IN DEGREES) OF THE F-35 AIRCRAFT, FOR THE THREE CONSIDERED FREQUENCY BAND (I.E., VHF, L, AND X, FROM TOP TO BOTTOM) UNDER THE MR REGIME. 61

FIGURE 8. RCSS (DBSM) (BLUE LINE) AND ITS MEAN VALUE (RED LINE) VERSUS AZIMUTH (IN DEGREES) OF THE F-35 AIRCRAFT, FOR THE THREE CONSIDERED FREQUENCY BAND (I.E., VHF, L, AND X, FROM TOP TO BOTTOM) UNDER THE LR REGIME. 62

FIGURE 9. THEORETICAL CDF AND ECDF VERSUS $\sigma\ of$ THE F-35AIRCRAFT, FOR THE THREE CONSIDERED FREQUENCY BANDS (I.E., VHF, L, AND X, FROM TOP TO BOTTOM) UNDER THE SR REGIME. 68

FIGURE 10. THEORETICAL CDF AND ECDF VERSUS σ OF THE F-35AIRCRAFT, FOR THE THREE CONSIDERED FREQUENCY BANDS (I.E., VHF, L, AND X, FROM TOP TO BOTTOM) UNDER THE MR REGIME. 69

FIGURE 11. THEORETICAL CDF AND ECDF VERSUS σ OF THE F-35AIRCRAFT, FOR THE THREE CONSIDERED FREQUENCY BANDS (I.E., VHF, L, AND X, FROM TOP TO BOTTOM) UNDER THE LR REGIME. 70

FIGURE 12. NORMALIZED AVERAGE AUTOCORRELATION OF THE RCS OF THE F-35AIRCRAFT, FOR THE THREE CONSIDERED FREQUENCY BANDS (I.E., VHF, L, AND X, FROM TOP TO BOTTOM) UNDER THE SR REGIME. 72

FIGURE 13. NORMALIZED AVERAGE AUTOCORRELATION OF THE RCS OF THE F-35AIRCRAFT, FOR THE THREE CONSIDERED FREQUENCY BANDS (I.E., VHF, L, AND X, FROM TOP TO BOTTOM) UNDER THE MR REGIME. 73

FIGURE 14. NORMALIZED AVERAGE AUTOCORRELATION OF THE RCS OF THE F-35AIRCRAFT, FOR THE THREE CONSIDERED FREQUENCY BANDS (I.E., VHF, L, AND X, FROM TOP TO BOTTOM) UNDER THE LR REGIME....74

FIGURE 15. EXAMPLE OF CENTRALIZED ARCHITECTURE FOR UTM....77

FIGURE 16. EXAMPLE OF DECENTRALIZED ARCHITECTURE FOR UTM. 78

FIGURE 17. PROJECT SYSTEM DESIGN....81

FIGURE 18. RESPEAKER MIC ARRAY V2.0. 85

FIGURE 19. ORIGINAL AND REDUCED TRAJECTORY IMPORTED FOR DRONE 1: (A) 3D PLOT, (B) 2D PLOT. 89

FIGURE 20. COMPARISON OF THE ORIGINAL AND SCALED TRAJECTORIES FOR DRONE 1 IN A TWO-DIMENSIONAL (2D) CONFIGURATION. 90

FIGURE 21. EXAMPLE OF AIRCRAFT CREATION IN BLUESKY ATC SIMULATOR....91

FIGURE 22. RADAR-BASED SIMULATION SCENARIO IN THE BLUESKY ATC ENVIRONMENT....102

FIGURE 23. ZOOM ON THE DRONE'S TRAJECTORIES IN THE RADAR-BASED SIMULATION SCENARIO IN THE BLUESKY ATC ENVIRONMENT. 102

FIGURE 24. ACOUSTIC SENSOR-BASED SIMULATION SCENARIO IN THE BLUESKY ATC ENVIRONMENT. 103

FIGURE 25. EXAMPLE ON GOOGLE EARTH OF THE FLIGHT AREA FOR DRONES AND LOCATION OF THE SURVEILLANCE SYSTEM (MIPS RADAR SYSTEM). 110

FIGURE 26. MIPS SYSTEM'S RACK....111

FIGURE 27. EXAMPLE OF THE GEOMETRIC CONFIGURATION OF THE TRANSMIT AND RECEIVE ANTENNAS USED IN THE MEASUREMENT CAMPAIGN. (A) X-BAND INTERFEROMETRIC CONFIGURATION. (B) L-BAND FULLY POLARIMETRIC....112

FIGURE 28. DJI MATRICE 300 (LEFT), DJI MAVIC 2 ENTERPRISE DUAL (RIGHT). 114

FIGURE 29. NOMINAL DRONE RANGE, DETERMINED FROM TELEMETRY DATA AND THE RADAR'S PRECISE GEOGRAPHIC COORDINATES, DURING MIPS SYSTEM OPERATION IN THE X-BAND (A) AND L-BAND (B) 115

FIGURE 30. RANGE-TIME MAPS (IN DB) OBTAINED FROM X-BAND DATA USING THE FIRST (A) AND SECOND (B) HALVES OF THE BEAT SIGNAL SAMPLES FOR EACH SLOW-TIME INDEX. 117

FIGURE 31. BEHAVIOR OF THE ECDFS OF BOTH THE DJI MATRICE 300 (RED CURVES) AND DJI MAVIC 2 DUAL ENTERPRISE (BLUE CURVES) USING THE RCS OBSERVATIONS IN THE X-BAND. 118

FIGURE 32. BOX-AND-WHISKER PLOTS FROM X-BAND DATA OF THE MATRICE 300 (A) AND MAVIC (B) DRONES. EACH BOX SHOWS THE STATISTICAL DISTRIBUTION OF NORMALIZED RCS VALUES FOR DIFFERENT AREAS AND SEGMENTS 120

FIGURE 33. RANGE-TIME MAPS (IN DB) DERIVED FROM L-BAND DATA USING THE SECOND HALF OF THE BEAT SIGNAL SAMPLES FOR EACH SLOW-TIME INDEX, SHOWN FOR THE FOUR POLARIZATION CONFIGURATIONS: (A) VV, (B) HH, (C) VH, AND (D) HV 121

FIGURE 34. BEHAVIOR OF THE ECDFS OF BOTH THE DJI MATRICE 300 (RED CURVES) AND DJI MAVIC 2 DUAL ENTERPRISE (BLUE CURVES) USING THE RCS OBSERVATIONS IN THE L-BAND. 122

FIGURE 35. BOX-AND-WHISKER PLOTS FROM L-BAND DATA OF THE MATRICE 300 (A) AND MAVIC (B) DRONES. EACH BOX SHOWS THE STATISTICAL DISTRIBUTION OF NORMALIZED RCS VALUES FOR POLARIZATION. 124

FIGURE 36. COMPARISON BETWEEN EMPIRICAL AND THEORETICAL CDFS OF NORMALIZED RCS OBSERVATIONS FOR THE MATRICE 300 DRONE IN THE X-BAND. EACH SUBPLOT CORRESPONDS TO A SPECIFIC AREA AND SEGMENT: (A) AREA 1 – SEGMENT 1, (B) AREA 1 – SEGMENT 2, (C) AREA 2 – SEGMENT 1, (D) AREA 2 – SEGMENT 2. 127

FIGURE 37. COMPARISON BETWEEN EMPIRICAL AND THEORETICAL CDFS OF NORMALIZED RCS OBSERVATIONS FOR THE MAVIC DRONE IN THE X-BAND. EACH SUBPLOT CORRESPONDS TO A SPECIFIC AREA AND SEGMENT: (A) AREA 1 – SEGMENT 1, (B) AREA 1 – SEGMENT 2, (C) AREA 2 – SEGMENT 1, (D) AREA 2 – SEGMENT 2. 128

FIGURE 38. COMPARISON BETWEEN EMPIRICAL AND THEORETICAL CDFS OBTAINED FROM DIFFERENT STATISTICAL MODELS (EXPONENTIAL, GAMMA, LOG-NORMAL, WEIBULL, AND GENERALIZED PARETO) FOR NORMALIZED RCS OBSERVATIONS IN THE L-BAND ACQUIRED FROM THE MATRICE 300 DRONE. RESULTS ARE SHOWN FOR THE FOUR POLARIZATION CHANNELS: (A) VV, (B) HH, (C) VH, AND (D) HV 130

FIGURE 39. COMPARISON BETWEEN EMPIRICAL AND THEORETICAL CDFS OBTAINED FROM DIFFERENT STATISTICAL MODELS (EXPONENTIAL, GAMMA, LOG-NORMAL, WEIBULL, AND GENERALIZED PARETO) FOR NORMALIZED RCS OBSERVATIONS IN THE L-BAND ACQUIRED FROM THE MATRICE 300 DRONE. RESULTS ARE SHOWN FOR THE FOUR POLARIZATION CHANNELS: (A) VV, (B) HH, (C) VH, AND (D) HV. 130

FIGURE 40. PICTURE OF THE NETTED AREA AT UNIVERSITY OF NAPLES FEDERICO II IN SAN GIOVANNI A TEDUCCIO. 139

FIGURE 41. PLATISMO 16"™ OCTAHEDRAL CORNER REFLECTOR. 141

FIGURE 42. CONFIGURATION OF TEST5 (LEFT) AND TEST6 (RIGHT). 143

FIGURE 43. COMPARISON BETWEEN THE RANGE PROFILE OF THE EMPTY NETTED-AREA WITH TEST2, TEST3 AND TEST5 144

FIGURE 44. COMPARISON BETWEEN THE RANGE PROFILE OF DRONE WITH AND WITHOUT THE CORNER REFLECTOR: (A) DRONE IN STATIC MODE (TEST3 & TEST5), (B) DRONE IN HOVERING TEST4 & TEST6). 145

FIGURE 45. SYSTEM CONFIGURATION OF THE EXPERIMENT WITH THE ACTIVE SYSTEM. 146

FIGURE 46. TEST DEVELOPMENT AND PROCEDURES WITH THE ACTIVE SYSTEM. 148

FIGURE 47. EXPERIMENTAL SETUP FOR THE TESTS WITH THE ACTIVE SYSTEM: (A) CONFIGURATION WITH THE FIRST COMPUTER CONNECTED TO THE SDR TRANSCEIVER INSTALLED ON-BOARD THE DRONE; (B) CONFIGURATION WITH THE SECOND COMPUTER CONNECTED TO THE ANCORTEK. 149

FIGURE 48. PEAKS OF THE SPECTRAL *AMPLITUDE* DISTRIBUTION FOR EACH TEST WITH THE ACTIVE SYSTEM ON-BOARD 153

FIGURE 49. MULTI-AGENT SYSTEM DESIGNED TO SIMULATE REALISTIC OPERATIONAL SCENARIOS: (A) DRONE STANIS EQUIPPED WITH CAMERA ZED 2I, (B) DRONE TARGET, (C) TERRESTRIAL ROBOT EQUIPPED BOTH WITH CAMERA ZED 2I AND ONE IR CAMERA OPTRIS PI 640I, (D) DJI MAVIC ENTERPRISE 158

FIGURE 50. DEMO SCENARIO SET-UP 159

FIGURE 51. IMAGES ACQUIRED TO TRAIN THE ZED 2I FOR THE AUTONOMOUS TARGET RECOGNITION ALGORITHM. 160

FIGURE 52. SCENARIO EXAMPLE OF THE FIRST PHASE OF THE EXPERIMENT 163

FIGURE 53. SCENARIO EXAMPLE OF THE SECOND PHASE OF THE EXPERIMENT. 164

FIGURE 54. SCENARIO EXAMPLE OF THE THIRD PHASE OF THE EXPERIMENT. 165

FIGURE 55. DIFFERENT PHASES OF PROCESS DEVELOPMENT 169

FIGURE 56. DRONE DJI MAVIC 3T AND GROUND CONTROL STATION. 170

FIGURE 57. EXAMPLE OF (A) POINT CLOUD OF FACADE (B) ORTHOPHOTO OF THE SAME FACADE. .. 173

FIGURE 58. FLOW CHART OF THE APPLIED METHODOLOGY. 179

FIGURE 59. URBAN ENVIRONMENT IN CASE VIII SCENARIO. 180

FIGURE 60. COMPARISON OF HDOP VALUE AT DIFFERENT FLIGHT HEIGHT LEVELS 181

FIGURE 61. COMPARISON BETWEEN THE POSITIONING ERROR IN THE LOCAL REFERENCE FRAME AND THE FLIGHT ALTITUDE VARIATION: (A) ANALYSIS OF THE X-AXIS ERROR COMPONENT; (B) ANALYSIS OF THE Y-AXIS ERROR COMPONENT. 182

LIST OF TABLES

TABLE 1.ONGOING SESAR JU PROJECTS FOR UAM.....29

TABLE 2. THEORETICAL CDF AND THEIR PARAMETERS 64

TABLE 3. BEST FIT THEORETICAL CDF AND THEIR PARAMETERS OF THE RCS DATA 66

TABLE 4. ADVANTAGES AND DISADVANTAGES OF CENTRALIZED ARCHITECTURE FOR UTM.....78

TABLE 5. ADVANTAGES AND DISADVANTAGES OF DECENTRALIZED ARCHITECTURE FOR UTM.....79

TABLE 6. SGR_RDR-216SR-1S10K-3D DATASHEET 85

TABLE 7. DJI MAVIC DUAL ENTERPRISE SPECIFICATIONS. 86

TABLE 8. COMMAND INTERFACE SUMMARY.....96

TABLE 9. RESPEAKER MIC ARRAY V2.0 TECHINCAL SPECIFICATIONS.....97

TABLE 10. MAIN FEATURES OF MIPS RADAR SYSTEM BOTH IN L- AND X-BAND.....113

TABLE 11. COMPARISON BETWEEN MAIN CHARACTERISTICS OF DJI MATRICE 300 AND DJI MAVI 2 DUAL ENTERPRISE.....114

TABLE 12. DISPERSION INDICES OF NORMALIZED RCS FOR BOTH DRONES ACROSS DIFFERENT AREAS AND SEGMENTS.....119

TABLE 13.DISPERSION INDICES OF NORMALIZED RCS FOR EACH DRONE AND POLARIZATION 123

TABLE 14. (A) CVM DISTANCES COMPUTED FROM THE AVAILABLE RCS OBSERVATIONS IN THE X-BAND FOR BOTH DRONES ACROSS DIFFERENT AREAS AND SEGMENTS. (B) PARAMETERS OF THE BEST-FITTING DISTRIBUTIONS ARE ALSO REPORTED: FOR THE GENERALIZED PARETO DISTRIBUTION, THE SHAPE AND SCALE PARAMETERS ARE DENOTED BY ξ AND σ, RESPECTIVELY, WHILE FOR THE GAMMA DISTRIBUTION THEY ARE DENOTED BY k AND θ. ...129

TABLE 15. (A) CVM DISTANCES COMPUTED FROM THE AVAILABLE RCS OBSERVATIONS IN THE L-BAND FOR BOTH DRONES ACROSS DIFFERENT POLARIZATION CHANNELS. (B) PARAMETERS OF THE BEST-FITTING DISTRIBUTIONS: FOR THE LOG-NORMAL, THE MEAN AND STANDARD DEVIATION OF THE LOGARITHM, DENOTED BY μ ANDΣ; FOR THE GAMMA, THE SHAPE AND SCALE PARAMETERS, k AND θ; FOR THE WEIBULL, THE SCALE AND SHAPE PARAMETERS, λ AND k; AND FOR THE GENERALIZED PARETO, THE SHAPE AND SCALE PARAMETERS, ξ AND σ. 131

TABLE 16. SUMMARY OF ADVANTAGES AND DISADVANTAGES OF BOTH PASSIVE AND ACTIVE SYSTEMS. 137

TABLE 17. ANCORTEK SDR-KIT 240B 140

TABLE 18. CONFIGURATION OF THE TEST PERFORMED WITH THE PASSIVE SYSTEM 142

TABLE 19. SUMMARY OF RESULTS OBTAINED DURING TESTS WITH PASSIVE SYSTEM. 146

TABLE 20. GNU RADIO PARAMETER SETTING FOR THE EXPERIMENT OF ACTIVE SYSTEM. 147

TABLE 21. ACTIVE SYSTEM TEST CONFIGURATIONS 152

TABLE 22. WORK PACKAGE STATUS MATRIX SHOWING COMPLETION STATUS, RESPONSIBILITIES, AND REQUIREMENTS FOR EACH WP. 161

TABLE 23. CLASSIFICATION OF URBAN ENVIRONMENTS CONSIDERING THE NUMBER OF BUILDING FLOORS AND THE STREET GEOMETRY. 177

LIST OF EQUATIONS

Eq.1 ---------- 35

Eq.2 ---------- 35

Eq.3 ---------- 64

Eq.4 ---------- 71

Eq. 5 ---------- 88

Eq. 6 ---------- 90

Eq. 7 ---------- 91

Eq. 8 ---------- 94

Eq. 9 ---------- 94

Eq.10 ---------- 94

Eq. 11 ---------- 95

Eq.12 ---------- 95

Eq.13 ---------- 95

Eq.14 ---------- 95

Eq.15 ---------- 95

Eq.16 ---------- 95

Eq.17 ---------- 98

Eq.18 ---------- 99

Eq.19 ----------107

Eq. 20 ----------107

Eq. 21 ----------107

Eq.22 ----------108

Eq.23 ----------125

Eq.24 ----------125

Eq.25 ----------149
Eq.26 ----------149
Eq.27 ----------149
Eq.28 ----------150
Eq.29 ----------150

1. Introduction

In contemporary times, Unmanned Aircraft Systems (UASs), better known as drones, emerged as one of the most prominent component of the technological revolution of the past decade.

Originally developed for military purposes, UAVs have progressively established a significant presence within the civilian domain, where they are now employed in a diverse array of applicants, ranging from precision agriculture to emergency medical response, reshaping how society approaches mobility, logistics, and data collection.

This widespread adoption has been made possible primarily due to the rapid and exponential technological growth of the past fifty to seventy years, which surged even further with the advent of the internet in the early 2000s. Indeed, this period marks what is commonly referred to as the "Unmanned Aircraft Systems (UAS) Golden Era" [1].

More precisely, the aviation industry is undergoing a fundamental paradigm shift toward Sustainable Air Mobility (SAM) and Urban Air Mobility (UAM) and drones in particular are increasingly regarded as central pillar of the Internet of Things (IoT), a paradigm shift that has redefined traditional modes of living, These emerging domains envision dense networks of both manned and unmanned aircraft sharing low-altitude urban and peri-urban airspace, with applications ranging from air taxis to autonomous delivery fleets. Such visions are deeply embedded in the broader framework of Smart Cities, where mobility, communication, and energy infrastructures converge to support a safer, cleaner, and more efficient quality of life. Moreover, their low-cost nature made these objects highly accessible and scalable. For these reasons and more, recent market reports estimate that the global UAV industry will reach between $27 billion and $100 billion by 2030 [2]. More detailed forecasts project the global drone market will grow from $30.6 billion in 2022 to $55.8 billion by 2024, with a compound annual growth rate (CAGR) of 7.8%. Looking further ahead, Morgan Stanley predicts the global Advanced Air Mobility (AAM) market will reach approximately $6.7 billion in 2025, $33 billion

in 2030, and grow to $1.2 trillion by 2050[3].

Nevertheless, UAM is confronted with a number of key challenges [4]. Unlike traditional aviation, which relies on well-structured air corridors and sparse high-altitude traffic, UAM will require highly accurate, redundant, and resilient surveillance systems capable of operating in complex environments characterized by obstacles, interference, and unprecedented traffic density. Ensuring safe and efficient integration of UAVs into shared airspace is therefore a cornerstone challenge for both regulators and technologists.

In dense and dynamic environments such as UAM, fundamental is the ability to reliably detect, track, and manage UAVs in dense and dynamic environments. Traditional Communication, Navigation, and Surveillance (CNS) infrastructures, designed for large aircraft, face inherent limitations when applied to small drones. Most notably, the Radar Cross Section (RCS) of small UAVs is orders of magnitude smaller than that of conventional aircraft making them nearly invisible to standard radar systems. Typical small UAVs, often constructed from plastics and carbon-fiber composites, exhibit RCS values in the range of 0.01–0.1 m^2, compared to 1–10 m^2 for light aircraft. This dramatic reduction translates directly into diminished Signal-to-Noise Ratio (SNR) and shortened detection ranges. Consequently, drones may remain undetected until they pose a direct risk to critical infrastructure or airspace safety. In addition, urban environments introduce unique electromagnetic (EM) challenges: multipath reflections caused by buildings, clutter from ground vehicles, and interference from dense communication networks further complicate reliable detection. At the same time, the growing threat of unauthorized or malicious drone use, which range from privacy violations to potential attacks, heightens the urgency of developing resilient, multi-modal surveillance systems.

From a scientific standpoint, the investigation of UAV RCS behavior advances our fundamental knowledge of EM scattering phenomena in unconventional, complex platforms. Small drones often exhibit stealth-like characteristics; these arise not from deliberate design but rather as an inherent by-product of their compact size, lightweight construction, and the extensive use of non-metallic composite materials. Consequently, the rigorous characterization of their scattering signatures

contributes significantly not only to the domain of UAV surveillance but also to the broader disciplines of radar target modeling and the development of counter-stealth methodologies.

From a practical standpoint, the implications are considerable. The seamless integration of drones into civil airspace necessitates that regulators and air navigation service providers establish frameworks to ensure safety, security, and system scalability [5]. A failure to develop dependable surveillance capabilities would erode public trust and ultimately impede the widespread adoption of UAM technologies. Conversely, the deployment of robust, multi-layered detection systems, which synergistically integrate radar, acoustic, optical, and cooperative surveillance technologies, is pivotal to unlocking the transformative potential of UAVs across critical sectors:

- *Public Safety and Security*: Enabling the rapid detection and mitigation of unauthorized drones in proximity to airports, critical infrastructure, or public gatherings.

- *Environmental Monitoring and Disaster Response*: Ensuring the reliable and safe coordination of large drone fleets for missions in response to wildfires, earthquakes, and other natural disasters.

- *Commercial Applications*: Facilitating the safe scaling of drone delivery services and automated industrial inspection processes without compromising the integrity of shared airspace.

Hence, this dissertation research aims to bridge the critical gap between the inherent limitations of traditional radar system applications and the stringent demands of nascent urban surveillance paradigms. It seeks to address this challenge through the dual contribution of theoretical predictive models and their empirical experimental validation.

1.1. UAV Classification

UAVs can be classified according to various criteria, including maximum take-off

weight (MTOW), size, propulsion systems, sensors, range and endurance, altitude, operating conditions, and capabilities, or any combination of these characteristics. It should be noted that some of these metrics affect the safety and performance requirements of the system, while others are relevant from operational, commercial, legal, or regulatory perspectives [6].

Small UAVs, also referred to as mini-UAVs, operate at Very Low Altitudes (VLA/LOS) in Class G airspace (uncontrolled airspace), typically below 400–500 ft, with the operator maintaining visual contact (Line of Sight, LOS) at all times. They are generally characterized by a maximum endurance of a few hours, a mass below 20 kg, and a range up to 30 km [6] The combination of small size, high versatility, design flexibility, ease of handling, and low cost makes these platforms particularly suitable for the objectives of this research.

UAVs can also be categorized by their propulsion and airframe type:

- Multi-Rotor Drones: High maneuverability, capable of carrying multiple payloads per flight, suitable for operations close to structures, though limited in endurance and speed.

- Fixed-Wing Drones: Capable of higher altitudes and longer flight durations, covering larger areas; often require a launcher system and can be more expensive. In some cases, endurance can reach 16 hours or more.

- Single-Rotor Drones: Strong and durable platforms, often complex and costly.

- Fixed-Wing Hybrid VTOL: Emerging technology combining vertical take-off capabilities with fixed-wing efficiency; autopilot systems manage stability, reducing pilot workload.

From a systems perspective, it is important to distinguish between system, architecture, and configuration, as these terms are frequently used in UAV research but with distinct meanings:

- System: The complete integration of hardware, software, and operational

procedures designed to perform a specific mission or function. For example, a UAV surveillance system integrating sensors, data fusion algorithms, and control interfaces constitutes a system .

- Architecture: The conceptual or logical organization of a system, describing the relationships and interactions between its components without specifying concrete implementations. Examples include centralized versus decentralized UAV traffic management architectures.

- Configuration: The concrete setup or arrangement of a system's components in a specific operational context. This includes parameters such as sensor placement, flight path planning, payload selection, and software settings during a mission.

Understanding these distinctions is critical for designing, analyzing, and deploying UAV operations, as they influence both technical performance and operational planning.

1.2. Research objectives and framework

The main aim of this dissertation is to investigate and propose innovative solutions for UAV detection and tracking in the context of AAM and UAM. The overarching research objective is to develop a comprehensive framework for edge enabled, multi-modal surveillance system capable of overcoming the challenges posed by small UAVs in semi-structured urban environments.

The specific research questions guiding this work are:

i. How can the RCS of UAVs be characterized and modeled under different operational conditions?

    - What statistical distributions best describe RCS fluctuations?

    - How does RCS vary across frequency bands and angular orientations?

ii. What role can multi-platform surveillance systems play in mitigating the

detection limitations of small RCS targets?

- How can different surveillance systems, such as radar and acoustic sensors, be integrated in simulation environments?
- What are the architectural trade-offs between centralized and decentralized detection systems?

iii. How can simulation findings be validated in real-world experimental setups?

- What methodologies ensure accurate measurement of UAV RCS in controlled and open-field conditions?
- Which can be the possible strategies to enhance the RCS of small drones and how they affect detection performance?

iv. How can cooperative multi-agent systems extend surveillance capabilities in complex urban settings?

- What role do autonomous exploration, target recognition, and cooperative engagement play in real-time detection?
- How can multi-modal sensor fusion be applied to enhance resilience?

By investigating the mentioned questions, this dissertation seeks to contribute both theoretical insights about UAV EM behavior and detection models, and practical tools, including simulation frameworks, experimental validation procedures, and case studies in real operational environments.

2. Advanced Air Mobility Systems and Surveillance Requirements

As mentioned before, the aviation sector is undergoing a paradigm shift toward AAM driven not only by technological innovation, but also by the pressing need for scalable and resilient surveillance, also considering sustainability drivers. Traditional CNS infrastructures were designed for high-altitude, low-density traffic and are ill-suited for dense, low-altitude operations in complex urban environments. This chapter establishes the state of the art in surveillance for UAM and AAM, highlighting the regulatory, technological, and operational drivers that motivate the exploration of edge-enabled surveillance solutions.

2.1. The Paradigm Shift Toward Advanced Air Mobility

The integration of unmanned and manned aircraft systems within urban airspace presents different challenges that extend far beyond simple traffic coordination. Indeed, the integration of UAVs in the airspace demands a comprehensive approach to safety and security assessment that encompasses not only traditional aviation safety principles but also addresses emerging cybersecurity threats, unauthorized airspace penetrations, and the unique operational characteristics of small-unmanned aircraft systems operating in proximity to critical infrastructure and populated areas.

The Unmanned Traffic Management (UTM) framework represents the foundational architecture upon which these future operations will be built. These systems must establish a well-connected airspace environment that enables efficient integration between traditional manned aviation and the emerging fleet of unmanned vehicles, while maintaining the highest standards of safety, security, and operational efficiency that the aviation industry has achieved over decades of development.

Central to this transformation is the evolution of CNS systems, which form the technological backbone of modern air traffic management. These three pillars work synergistically to create a robust operational environment that can accommodate the increasing complexity of mixed traffic scenarios, ensuring a correct, efficient and secure integration of drones in the urban scenarios.

2.1.1. U-Space & Regulatory Frameworks

The rapid expansion of the UAS market has necessitated the development of a regulatory framework capable of ensuring a safe and orderly integration of diverse platforms, both manned and unmanned, within a common airspace. This framework must also account for the emerging demands of UAM and commercial applications such as package delivery. In response to these challenges, the European Union Aviation Safety Agency (EASA) introduced a harmonized set of regulations in 2019, establishing new standards for certification, design, manufacturing, and licensing procedures. More in particular, in order to develop standard processes and procedures to enable UAM operations, several projects were developed thanks to the Single European Sky ATM Research Program (SESAR) Joint Undertaking [7]to investigate the core enabling technologies and operative solutions. U-space is one of the most prominent projects within the SESAR initiative. U-space is the European framework for the safe and efficient integration of drones into airspace, conceived as a set of new services that rely on a high degree of digitalization and automation of functions. Its purpose is to enable large-scale, secure, and sustainable drone operations, particularly in urban environments where traffic density and operational complexity are expected to be unprecedented [8].

First of all, must be noticed that the cornerstone of the regulatory advancement is represented by Regulation (EU) 2019/945 and Regulation (EU) 2019/947 [8,9], which adopt a risk-based classification of UAS operations into three categories:

i. Open category, addressing low-risk operations with minimal regulatory requirements;
ii. Specific category, covering medium-risk operations requiring operational authorization based on a risk assessment; and
iii. Certified category, encompassing high-risk operations that demand certification comparable to manned aviation, including airworthiness approval and type certification [8–10]

In the certified category, both the remote pilot and the operator must obtain appropriate licenses, ensuring compliance with the highest safety standards. The first operational domains subject to investigation within this framework include:

- Cargo UAS operations,
- UAM and package delivery operations, and
- UAS operations with an onboard pilot.

To complement these measures, U-space establishes a harmonised regulatory foundation throughRegulation (EU) 2021/664, 2021/665, and 2021/666 [11–13], which apply to all UAS, operators, and service providers, with the exception of operations involving sub-250 g platforms or drones belonging to the C0 class.

The regulation defines a series of mandatory services that form the core of the framework: network identification, geo-awareness, flight authorization, traffic and weather information, and conformance monitoring. Collectively, these services are designed to ensure accountability, situational awareness, and operational safety in dense environments. The implementation of U-space is structured into four progressive stager (U1-U4) :

- U1 – Foundation services, covering electronic registration, electronic identification, and geofencing (already deployed).
- U2 – Initial services, including flight planning, approval, tracking, and interaction with conventional air traffic control.
- U3 – Advanced services, supporting more complex operations in dense areas through conflict detection and automated detect-and-avoid functions.
- U4 – Full services, providing highly automated and digitized operations for both drones and the U-space system, envisioned for full deployment by 2030.

To support this roadmap, several large-scale projects have been developed under the SESAR Joint Undertaking. Initiatives such as CORUS XUAM, AMU-LED, and Uspace4UAM investigate enabling technologies and operational solutions, providing validation through simulations, demonstrations, and real-flight trials, as

summarized in Table 1. These projects not only accelerate the technological maturity of U-space services but also contribute to regulatory harmonization and societal acceptance.

These regulatory frameworks, while enabling the safe deployment of UAS and UAM, implicitly shift surveillance requirements toward architectures that are adaptive, distributed, and edge-capable, given the density and risk profile of future urban operations.

Ultimately, U-space and UTM reflect a global consensus: the successful deployment of Urban and Advanced Air Mobility cannot rely solely on technological innovation but must be grounded in standardized, interoperable, and adaptive frameworks. These frameworks also shape future surveillance architectures, demanding resilient, edge-enabled solutions that can integrate cooperative and non-cooperative detection methods in increasingly complex operational environments.

Project	Starting Date	Objective	Focus Area	Expected Contribution
CORUS XUAM [14]	01/12/2020	Development of a Concept of Operations (ConOps) and services for UAM.	Operational concepts, service architecture	Provides the reference ConOps framework for UAM integration.
AURA - ATM [15]	01/01/2021	Identification of requirements for U-space interface with ATM	U-space/ATM interoperability, requirements definition	Ensures seamless integration between U-space and traditional ATM.
AMU-LED [16]	01/01/2021	Large-scale demonstration of UAM ConOps.	Simulation, validation, real-flight demonstrations	Validates UAM operations through large-scale trials
GOF2.0 [17]	01/01/2021	Assurance of safe separation for integrated UAM and manned operations.	Separation management, mixed traffic scenarios	Develops methods and tools for conflict detection and resolution.
Uspace4UAM [18]	01/02/2021	Definition of system requirements and automated services for UAM.	Automation, system integration, service deployment	Lays the foundation for UAM-specific U-space services.
EUREKA [19]	2023	Vertiport infrastructure and IAM deployment; arrival/departure, turnaround, emergencies.	Vertiports, traffic / network flow, disruption management, regulatory & infrastructure	Impacts surveillance at vertiports, sensor systems/capabilities, ATM/CNS integration for vertiport operations.
OperA [20]	2023	Pilot & unmanned UAM operations validated in real-ATC, focus on autonomy & environmental metrics.	Autonomy, piloted vs unpiloted, sustainability, routing, air/ground interface	Advances surveillance (air/ground), navigation accuracy, safety in non-nominal conditions.
ENSURE [21]	2023	Interface & services between U-space and ATM; dynamic airspace reconfiguration.	Data architecture, safety, interface standards, ATM-U-space separation	Enhances CNS definitions, communication & surveillance data exchange; ATM/U-space synergy.
SPATIO[22]	2023	Separation management in U-space; capacity vs safety trade-offs.	Strategic & tactical conflict resolution, capacity planning	Key surveillance / conflict detection; navigation & separation assurance modules.

SAFIR-Ready [23]	2023	Enable rapid, critical drone missions; advanced U-space services; drone cargo ports.	Detect & avoid, dynamic capacity, drone port infrastructure, emergency missions	High-demand on surveillance & communications, especially for critical & time-sensitive operations.
ImAFUSA [24]	~2024	Societal acceptance of UAM; tools & indicators for public perception.	Public perception, stakeholder engagement, social acceptance metrics	Indirectly related to surveillance: impacts how surveillance / CNS deployment is perceived & regulated.

Table 1.Ongoing SESAR JU projects for UAM.

2.1.2. Technological Convergence and Innovation Drivers

Technological convergence is not only transforming vehicle capabilities but also reshaping how surveillance data are generated, processed, and acted upon. The integration of compact high-performance sensors with onboard guidance, navigation, and control (GN&C) functions provides a data-rich environment that, however, requires real-time processing close to the source. Edge computing architectures, leveraging Artificial Intelligence (AI)-driven fusion of radar, electro-optical, and communication data, emerge as a key enabler for predictive surveillance and autonomous deconfliction in UAM scenarios [25].

The rapid advancement of drone technologies has driven the development of sophisticated surveillance strategies within CNS systems, which are essential for the safe integration of UAVs into shared airspace. The International Civil Aviation Organization (ICAO) highlights the need for coordinated frameworks that address emerging operational scenarios, including mixed manned and unmanned traffic, UAM, and cargo delivery

Drone surveillance relies on the integration of onboard and ground-based CNS systems to provide accurate, real-time situational awareness. More in particular, modern UAVs are equipped with compact, high-performance sensors, such as micro electro-mechanical systems (MEMS) devices, supporting GN&C functions. Surveillance systems must interface with these sensors to enable critical tasks, including sense-and-avoid, trajectory tracking, and fault detection. AI algorithms,

data fusion, and advanced image processing can further enhance situational awareness, enabling predictive analytics and autonomous decision support [26].

In complex urban airspace, adaptive CNS-enabled flight management allows dynamic monitoring of vehicle positions, velocities, and intentions, ensuring safe deconfliction in vertiports, low-altitude corridors, and on-demand operations. Trajectory-Based Operations (TBO) and real-time airspace management enable efficient routing, conflict prediction, and adaptive allocation, accommodating heterogeneous UAV fleets [27].

Overall, effective UAV surveillance requires modular, interoperable CNS systems capable of integrating diverse data sources. These systems support semi-autonomous and autonomous operations, ensuring safe coexistence with manned aircraft while maintaining operational efficiency and situational awareness in increasingly complex airspace [28].

2.2. Surveillance Systems in Urban Air Mobility and Advanced Air Traffic Management

Surveillance is a fundamental component of the CNS system, essential for supporting Urban Air Traffic Management (UATM) and AAM [29,30] .

Traditional surveillance approaches, developed for conventional aviation operations, face significant challenges when applied to urban air mobility scenario. The sheer volume of anticipated traffic, the low-altitude operational environment, the presence of numerous obstacles and EM interference sources, and the diverse operational characteristics of various aircraft types create a surveillance challenge of remarkable complexity [29,30].

Urban environments introduce unique challenges that affect surveillance strategies. The dense concentration of buildings, communication towers, and other infrastructure creates complex EM environments that can interfere with traditional radar systems and satellite-based navigation. The presence of multiple flight levels operating simultaneously within relatively confined airspace volumes demands

surveillance systems with exceptional accuracy, reliability, and real-time processing capabilities [31].

Furthermore, the operational paradigm of urban air mobility introduces concepts such as vertiports, dynamic air corridors, and on-demand flight operations that require surveillance systems capable of managing rapidly changing traffic patterns and flight intentions. Moreover, the integration of autonomous and semi-autonomous aircraft adds another layer of complexity, requiring surveillance systems that can effectively monitor and verify the performance of artificial intelligence-based flight management systems.

The complexity of urban air mobility operations necessitates a comprehensive understanding of the various surveillance system architectures available and the strategic considerations that guide their selection and deployment. Modern surveillance systems can be categorized across multiple dimensions, each offering distinct operational characteristics and capabilities that must be carefully matched to specific operational requirements and environmental constraints.

Surveillance Systems (SS) can be classified in two primary configurations [32]:

- *Air-to-air systems*: which represent a distributed approach to airspace monitoring, where individual aircraft are equipped with onboard sensors capable of detecting and tracking nearby vehicles. These systems provide enhanced situational awareness directly to flight crews or autonomous flight management systems, reducing dependency on ground-based infrastructure and enabling operations in areas with limited ground surveillance coverage. The primary advantages include reduced latency in threat detection, enhanced operational flexibility in remote areas, and improved redundancy through distributed sensing capabilities.
- *Ground-to-Air System*: employ centralized monitoring infrastructure, typically consisting of radar stations, communication nodes, and processing centers that provide comprehensive airspace coverage from fixed or mobile ground installations. These systems excel in providing coordinated airspace management, centralized threat assessment, and

integration with existing air traffic control infrastructure. They offer superior coverage consistency and the ability to maintain operational continuity even when individual aircraft experience equipment failures.

Furthermore, SS can be categorized as:

- **Non-Cooperative**, which means that they operate independently without requiring active participation from target aircraft, relying instead on passive detection methods such as primary radar reflections, electro-optical sensors, or acoustic signatures. These systems provide essential capabilities for detecting unauthorized or non-compliant aircraft that may not be equipped with standard aviation transponders or may be attempting to operate covertly. Their independence from target cooperation makes them particularly valuable for security applications and regulatory enforcement.
- **Independent Cooperative**, so they leverage standardized transponder responses and broadcast signals to calculate target positions through triangulation and time-of-arrival analysis. Technologies such as Secondary Surveillance Radar (SSR) and traditional ADS-B implementations fall into this category, providing reliable position information while maintaining independence from onboard navigation system accuracy. They offer a balance between cooperative efficiency and system autonomy.
- **Dependent Cooperative**, which relies heavily on the accuracy and integrity of onboard navigation and communication systems, with ground stations serving primarily as data collection and distribution nodes. Modern implementations include satellite-based tracking systems and advanced ADS-B variants that depend on high-precision GNSS positioning. While offering superior accuracy when properly functioning, these systems require robust integrity monitoring to detect and mitigate potential navigation system failures or cybersecurity compromises.

In practice, no single surveillance approach can fully meet UAM requirements. Multi-layer architectures that combine cooperative technologies (e.g., ADS-B, Remote ID) with non-cooperative sensing (radar, EO/IR, acoustic) and edge-level fusion are increasingly recognized as the only viable path toward resilient surveillance in dense urban airspace.

The selection of appropriate surveillance system architectures requires comprehensive evaluation across multiple decision factors that directly impact operational effectiveness, economic viability, and system sustainability:

- Cost-effectiveness: initial investments, operational expenses, and lifecycle costs, economic scalability and cost-sharing opportunities between multiple stakeholders and operators.
- Power and Energy requirements: power consumption, energy source availability and reliability, power efficiency optimization for remote installations and environmental impact.
- Physical dimensions: size constraints for installation and power availability.
- Weight considerations: impact on aircraft performance and payload capacity.

It is also fundamental, besides the mentioned main choice factor, to take into consideration operational and maintenance factors and regulatory and standards compliance.

The optimal surveillance architecture for any given urban air mobility implementation typically involves a combination of multiple system types, selected and configured to address the specific operational requirements, environmental constraints, and economic considerations of the target deployment scenario. This multi-layered approach provides enhanced redundancy, improved coverage, and greater operational flexibility while managing overall system complexity and cost.

Surveillance systems now face security challenges extending far beyond traditional aviation threats. The rise of unauthorized or maliciously operated drones creates new risks, demanding advanced detection, classification, and response capabilities.

For small Remote Piloted Aircraft System (RPAS) threatening infrastructure or public safety, a three-phase process (detection, classification, verification) is critical. Military and law enforcement require systems with real-time threat assessment and rapid response coordination.

As concerns the ground-to-air systems, Radar Stations (RS) are basic tools for UAV surveillance because of their advantage of working in any weather and light conditions and at larger distances as compared to others sensor such as electro-optical, acoustic and lidar systems under conditions of clutter and jamming. At the same time, they can determine the range, speed and angular coordinates of targets.

2.3. Drone Detection and Radar-Cross Section issues

A critical limitation of traditional radar-based surveillance in UAM scenarios lies in the RCS of small drones. Understanding this constraint is fundamental because it not only affects the detection range and SNR but also motivates the exploration of innovative solutions, such as distributed low-power radars, probabilistic detection models, and edge-level processing pipelines.

The RCS challenge represents perhaps the most fundamental limitation facing radar-based surveillance systems when attempting to detect small-unmanned aircraft. This challenge directly impacts the effectiveness of the ground-to-air radar systems that form a critical component of the surveillance architectures discussed previously, particularly in their application to UTM and U-Space operations.

The RCS of small drones presents a significant detection challenge, with typical values ranging between 0.01 and 0.1 m^2 for micro drones (under 2 kg) and mini drones (2-25 kg). This represents approximately 1/10000 to 1/1000 the RCS of conventional aircraft, creating a dramatic reduction in target visibility that places these platforms below the detection threshold of many traditional surveillance radars.

The problem is fundamentally rooted in the construction materials and design philosophy of modern drones. Most small unmanned aircraft are constructed from plastic or carbon fiber composites chosen for their lightweight characteristics and

flight performance optimization rather than their EM visibility. These radar-transparent materials contribute significantly to the reduced RCS, making drones inherently less reflective of traditional radar systems operating within the surveillance architecture discussed previously.

From a more technical point of view, the RCS is defined by the Institute of Electrical and Electronics Engineering (IEEE) as a measure of the reflective strength of a target when illuminated by a radar. The mathematical definition is given as (1):

$$\sigma = \lim_{R \to \infty} 4\pi R^2 \frac{|E_S|^2}{|E_i|^2} \tag{1}$$

The equation (1) shows that the RCS of a target is the ratio of the incident electric field (E_i) and the scattered electric field (E_s) as seen at great distance.

Moreover, it is fundamental to highlight that the RCS is a function of the following parameters:

- Position of the transmitter relative to the target.
- Position of the receiver relative to the target.
- Target geometry and material composition.
- Angular orientation of target relative to the transmitter and receiver.
- Frequency.
- Transmitter polarization.
- Receiver polarization.

2.3.1. Signal-to-Noise Ratio Impact and Detection Range Constraints

The relationship between RCS radar detection performance is governed by fundamental physics principles that create severe constraints on surveillance system effectiveness. As shown in (2), the SNR of a radar system is directly proportional to the target RCS (σ) and inversely proportional to the fourth power of the detection range (R):

$$SNR \propto \frac{\sigma}{R^4} \tag{2}$$

This relationship demonstrates that a small RCS (low σ) results in correspondingly low SNR, making the drone radar return weak and often indistinguishable from background noise or environmental clutter. The implications for surveillance system design are profound: traditional SNR detectors frequently fail to identify these weak signals, resulting in high rates of missed targets that compromise the effectiveness of the three-phase identification process outlined in our surveillance architecture discussion.

The range limitations imposed by low RCS values have direct implications for the infrastructure requirements of UAM surveillance networks. Ground-based radar systems that might provide adequate coverage for conventional aircraft operating at typical RCS values of 1-10 m^2 require significantly denser deployment to achieve equivalent coverage for drone targets. This infrastructure multiplication directly impacts on the cost-effectiveness criteria that guide surveillance system selection, potentially making traditional radar-based solutions economically unfeasible for comprehensive UAM coverage.

3. Pathways to Innovation and Entrepreneurship

Given the rapidly evolving landscape of UAM, characterized by high technological innovation and strong multidisciplinary interactions, it becomes essential to develop heterogeneous ecosystems capable of supporting the sustainable growth and integration of this sector

The “Pathways to Innovation and Entrepreneurship” program [33], funded by the U.S. Embassy in Italy in 2023 with a $50,000 grant, was conceived and coordinated by Prof. Mita Marra from the University of Naples Federico II, with the support of an international committee of experts. the program represents a paradigm shift in the way technology development and commercialization are approached. It promotes transdisciplinary collaboration and experiential learning as alternatives to traditional disciplinary frameworks, encouraging the development of entrepreneurial mindsets, technology transfer skills, and real-world problem-solving abilities.

The primary objective of this initiative is to strengthen collaborative networks between universities and enterprises in Southern Italy, thereby contributing to the creation of a dynamic and interconnected ecosystem in which researchers, professionals, and entrepreneurs, both emerging and established, can exchange knowledge, ideas, and innovative practices. More specifically, the project seeks to foster a culture of innovation and risk-taking, with the aim of enhancing research–industry collaboration, supporting highly skilled employment, promoting technological and social innovation, and facilitating the creation of new enterprises.

Through a comprehensive training pathway culminating in a collaborative project for DOCG (Denominazione di Origine Controllata e Garantita) wine regions, the highest Italian wine quality classification, equivalent to Controlled and Guaranteed Designation of Origin, in the Irpinia area Italy, the program showcases the potential of integrating cutting-edge drone technology, artificial intelligence, and sustainable agricultural practices with cultural heritage preservation and economic development.

3.1. Structure of Training Activities

The project originates from the recognition that Italian Small and Medium-sized Enterprises (SMEs) particularly those with fewer than ten employees, often lack the skilled workforce required to successfully manage the digital and ecological transitions. Although approximately 70% of SMEs have already introduced digital practices, their limited capacity to absorb highly qualified human capital may lead to the emigration of specialized workers, hence exacerbating labor market inequalities in less innovative regions such as Campania. To address these challenges, the initiative promotes entrepreneurship education grounded in university–industry collaboration between the United States of America and Italy. More specifically, it leverages the presence of significant opportunities for qualified employment in Southern Italy across key sectors such as mechanics, tourism, agri-business, and the cultural and creative industries. Furthermore, empirical studies indicate that prospective entrepreneurs are more likely to establish businesses in their region of origin when supported through peer-to-peer learning and the development of local networks.

In particular, the training pathway was organized into four thematic sessions held across different locations in Campania (Naples, Cava de' Tirreni, Altavilla Irpina, and Caggiano) between January and May 2024, and culminated in a study mission in New York at the Italian Academic Center, in collaboration with Cornell Tech, in June 2024. These sessions included:

- keynote speeches delivered by international experts;
- roundtables with entrepreneurs and industry leaders;
- case study presentations on university–industry collaboration;
- networking opportunities for young researchers to present their research and professional aspirations.

The four meetings topics and place where have been hold were:

- "*Doing Business within the Ecosystem*", in San Giovanni Campus of University of Naples Federico II within the Eastern peripheral area of the city (January 31, 2024).
- "*Entrepreneurial ecosystems in the g-Local context*", at the Monumental Complex of San Giovanni of the Municipality of Cava de' Tirreni (February 1, 2024).
- "*Entrepreneurial ecosystems within the ecoregions: An agenda for sustainability*", at the Municipality of Altavilla Irpina, in Irpinia (March 20, 2024).
- "Cultural ecosystems in energy transition: Art and culture for developing rural areas", Castello Normanno del Guiscardo, Caggiano SA (May 24, 2024).

The project involved nine young researchers, including doctoral candidates, post-doctoral fellows, and recent graduates from different research sectors, together with SMEs and startup founders. These sessions combined keynote lectures on strategic issues with panel discussions, Q&A sessions, roundtables, and case studies on university–industry collaboration. Young researchers were given the opportunity to present their work and aspirations, engage in networking with entrepreneurs, and develop collaborative projects with companies. The training was structured around four main pillars: customer discovery, decision-making, pitching and selling, and team building.

The program culminated with a Summer School at the Italian Academic Center in New York from June 24 to 28, 2024. The idea is to bridge local entrepreneurial ecosystem with global networks of researchers and entrepreneurs.

3.1.1. Transatlantic Collaboration: New York Summer School.

The Summer School "Bridging the Atlantic: Pathways to Innovation and Entrepreneurship", held in New York in collaboration with Cornell Tech, represented the culmination of the training program. Its primary aim was to enhance participants' competencies in both technological and social innovation while

expanding collaborative networks between businesses and research institutions at the local, national, and international levels.

In addition to young researchers, the Summer School brought together entrepreneurs, industry experts, and managers, thereby creating a multidisciplinary environment conducive to knowledge exchange and innovation. The curriculum was organized into five modules that addressed:

i. macroeconomic trends shaping global innovation;
ii. entrepreneurship in deep-tech ventures and social enterprises;
iii. strategies for high-impact investment;
iv. the evaluation and governance of sustainable transitions;
v. structured networking activities with companies and researchers in the New York metropolitan area.

A distinctive component of the Summer School was the collaborative project development exercise. Building on insights from the workshop conducted in Altavilla Irpina with local wine and agri-food enterprises, participants worked on a project aimed at valorizing DOCG villages in Irpinia. This project not only showcased the potential of linking cultural heritage with entrepreneurial innovation but also highlighted the broader relevance of place-based strategies for sustainable development.

Upon successful completion of the program, participants were awarded a Certificate of Learning Achievement jointly conferred by the University of Naples Federico II and Cornell Tech. This certification formalized the acquisition of new skills in innovation management, entrepreneurship, and sustainability, while also marking the establishment of long-term transatlantic collaborations.

3.2. Innovation Challenges in the Campania Region

The Campania region, classified as a “moderate innovator” within Southern Europe, faces several systemic challenges that constrain its innovation capacity and the effective transfer of technology, including in fields such as drone surveillance

systems. Understanding these challenges is critical when evaluating the development and adoption of advanced technologies.

a. *Increase of Qualified Manpower and Limited Absorptive Capacity.*
   Italian SMEs, particularly those with fewer than ten employees, frequently lack the qualified workforce necessary to navigate both digital and ecological transitions. This limited absorptive capacity contributes to the emigration of specialized workers, thereby exacerbating regional inequalities in less innovative areas like Campania. While universities play a central role in shaping human capital, fostering entrepreneurship, and generating both direct and indirect employment, the capacity of local firms to integrate highly skilled labor remains a persistent challenge.
b. *Enhance University–Business Collaboration in Peripheral Regions*.
   Despite the growing responsibilities and outreach of universities, research indicates that university-business collaboration in peripheral regions is often less effective than in core innovation hubs. SMEs in such regions tend to exhibit lower inclinations and capabilities for partnering with universities and other science and technology actors. Consequently, the transfer of advanced research (including innovations relevant to drone surveillance) from academic laboratories to industrial applications remains limited. Moreover, while collaboration with technology suppliers, competitors, and research institutions can enhance innovation activities, the role of universities in reducing innovation costs and risks is not yet fully realized in moderate innovation regions.
c. *Promote R&D-oriented SMEs strategies.*
   SMEs in Campania are predominantly market-driven rather than research-driven. They tend to prioritize managerial or process innovations over formal R&D activities, sourcing knowledge primarily from suppliers, customers, and competitors. Data indicates that a significant proportion of companies invest in acquiring existing machinery, equipment, or software rather than developing new technologies internally. This orientation that implies technological and digital transitions, including those required for

sophisticated drone surveillance systems, often occur gradually, requiring sustained strategic commitment and investment.

d. *Address socioeconomic Disparities and Foster Balanced Innovation Environments.*

   Socioeconomic disparities within the region create heterogeneous innovation environments. Local factors significantly influence how knowledge is generated, diffused, and absorbed, affecting collective learning and knowledge transfer. While Campania exhibits above-average specialization in certain sectors, most companies do not produce high-end R&D components and rely heavily on global production networks. This dependence can limit the local development of advanced technological components essential for sophisticated drone surveillance systems. Moreover, innovation tends to emerge more readily in densely populated or economically agglomerated areas, indicating that sub-regions within Campania may be unevenly positioned to foster technological advancement.

e. *Facilitate Technology Adoption and Diffusion.*

   Policy research emphasizes the importance of aligning regional capabilities with a supportive culture of innovation. In less advanced areas, this alignment is crucial for enhancing entrepreneurial activity and facilitating the adoption of emerging technologies. The Pathways to Innovation and Entrepreneurship project addresses these challenges by promoting an "entrepreneurial mindset" and fostering critical and evaluative thinking. Such competencies are essential to overcome resistance to the adoption of novel and potentially disruptive technologies, including drone surveillance systems.

3.3. Case Study: Technological Innovation and Sustainability in Irpinia DOCG Regions

In light of the innovation challenges faced by the Campania region, and considering the key themes addressed during the first three sessions of the Pathways program (including university–industry collaboration, territorial systems and global markets,

entrepreneurial ecosystems and sustainability, ecoregions and risk management, and investments for sustainable innovation) the young researchers collaboratively developed an initial project. This project served as a practical demonstration of the program's transdisciplinary approach, integrating diverse perspectives and skills to address complex socio-technical challenges.

More specifically, during the meetings, particular attention was drawn by local wine merchants in Altavilla Irpina, who hosted the involved researchers on April 30, 2024, to discuss the delicate challenges currently affecting their businesses and the broader territorial ecosystem. These issues emerged along four main dimensions:

- Social: cultural heritage preservation, area livability, and rural depopulation.
- Environmental: heterogeneous land morphology, summer aridity, and scarce or absent rainfall.
- Economic: persistently low grape prices and difficulties in attracting and retaining skilled employees.
- Governance: the need for a common vision and the establishment of collaborative networks among viticultural industries.

Hence, the project evolved towards a transdisciplinary approach designed to address these complex and interdependent challenges by integrating technological innovation, cultural heritage, and sustainable business models.

The Figure 1 illustrates the logical framework of the project. On the left, the current challenges (depopulation, low grape prices, limited tourism) are presented. At the center, technological solutions such as drone-based monitoring, AI-driven predictive models, and chemical viticulture innovations are proposed. On the right, the expected results highlight potential improvements in product quality, market positioning, and brand recognition. At the bottom, the strategic question, which defines territorial wine excellence, connects DOCG quality, cultural heritage, and innovation technology into a unifying vision.

Figure 1 also details the implementation strategy and technological integration. It outlines a phased plan:

- Phase 1: Data collection through drone deployment and baseline acquisition.
- Phase 2: AI model development and digital platform creation.
- Phase 3: Market integration with consumer engagement tools.

In parallel, the project envisions digital wine passport features leveraging blockchain authentication and immersive AR/VR experiences.

Finally, the five-year socio-economic impact projection (bottom of the figure) quantifies the expected returns: +25% revenue growth, the creation of 150 new jobs with a focus on retaining young professionals, and a 30% reduction in pesticides through sustainable, carbon-neutral practices.

To conclude, the figure demonstrate how a territory-driven innovation model can convert systemic regional difficulties into opportunities for socio-economic revitalization, technological advancement, and cultural valorization.

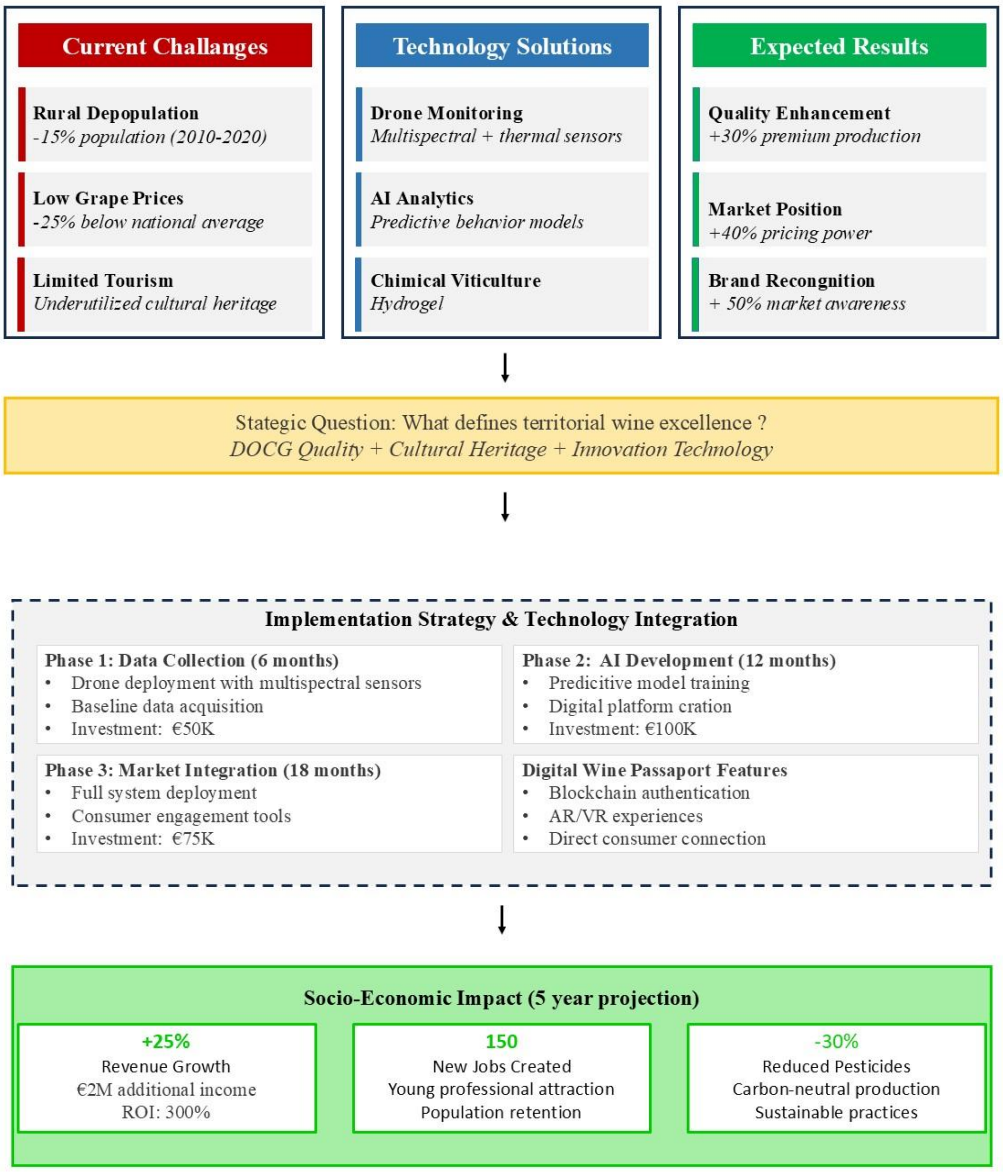

Figure 1. Project logical framework.

3.3.1. Integrated Technological Solution Framework

As mentioned earlier, the overarching goal of project born by the collaboration between young researchers and the wine merchants is to valorize the DOCG wine regions of Irpinia by integrating advanced technological solutions with social and entrepreneurial initiatives. Within this framework, drones play a central role in agricultural innovation, as their use aligns with the broader objectives of Agriculture 4.0. More specifically, they can streamline business processes, optimize

relational activities supply chain actors, ensure product quality and traceability, and ultimately improve the efficiency of agricultural systems.

The benefits of utilizing drones in this context are considerable, ranging from time optimization and reduced environmental impact to enhanced sustainability and operational safety. In addition, drones can be deployed for tasks such as planting and seeding in difficult-to-reach areas, applying treatments with higher precision, and providing security monitoring in remote agricultural contexts.

The surveillance and monitoring capabilities of drones are fundamentally determined by the suite of sensors they are equipped with. These include:

- RGB and multispectral cameras, which facilitate the assessment of plant health and the detection of anomalies;
- LiDAR sensors, employed for high-resolution topographic mapping, soil management, and biomass quantification;
- Hyperspectral sensors, enabling fine-grained analysis of plant and soil chemical composition as well as the early identification of diseases and stress factors;
- Thermal sensors, applied to the monitoring of plant water stress;
- Gas sensors, designed to detect and measure greenhouse gas emissions;
- Flow and rate sensors, which ensure the accurate application of pesticides and fertilizers.

Taken together, these sensing technologies provide a multidimensional perspective on vineyard health, generating real-time data streams that can be processed within hours and offering unattainable diagnostic precision through traditional inspection methods.

Moreover, they enable the generation of infrared imagery capable of distinguishing between healthy and diseased plants, while simultaneously providing real-time data streams that can be processed within hours. This integration of multi-sensor capabilities thus transforms drones into powerful platforms for comprehensive agricultural surveillance and decision support.

Nevertheless, relying exclusively on a single platform for data collection may not be sufficient. Hence, the project under discussion explores an integrated approach, that combine drones with satellites. Instead of drones, also balloons represent a valid alternative since they represent a cost-effective and flexible alternative, especially suited to heterogenous or mountainous landscapes, and they enable longer acquisition times than drones. The concept of "correlation between drone/balloon and satellite data" is central in this regard. While drone data typically covers only a few years, satellite imagery spans decades; integrating the two makes it possible to generate "drone-like data" for earlier periods, thereby improving the interpretation of future satellite acquisitions. To achieve this, downscaling techniques are necessary to harmonize proximity data with satellite resolution and establish meaningful correlations.

The resulting integrated data streams can serve as inputs for predictive models. Time-series forecasting techniques analyze sequentially collected data to identify trends and extrapolate them into the future. For instance, soil moisture prediction can optimize irrigation schedules, reducing water waste and improving yields, while nutrient level predictions can guide fertilizer application, preventing over-fertilization and minimizing environmental impacts. Advanced machine learning approaches, such as Recurrent Neural Networks (RNNs) and Long Short-Term Memory (LSTM) architectures, are particularly suited for such tasks, as they capture temporal dependencies and enhance predictive accuracy. Importantly, these capabilities extend beyond abiotic monitoring to encompass biotic interactions as well.

Indeed, soil microbiota play a vital role in vineyard sustainability. They act as nitrogen reservoirs, stimulate plant defenses, produce growth-promoting hormones, and contribute to nutrient accumulation. Furthermore, bacteria reduce vine mortality under drought conditions by enhancing root development, improving water retention through sugar release, and supporting osmoregulation and nutrient storage. Understanding these intricate plant–microbe interactions is thus crucial for sustainable vineyard management and long-term productivity.

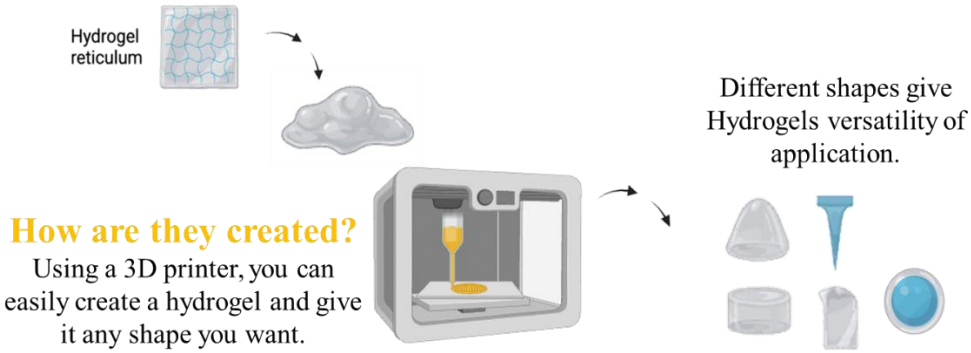

Figure 2. Hydrogel application methodology.

In this regard, hydrogels have been proposed as innovative tools to enhance resource efficiency (see Figure 3). These three-dimensional hydrophilic polymers, which can be produced via 3D printing in customizable shapes, are capable of retaining significant amounts of water and can encapsulate pesticides, fertilizers, bacteria, or polysaccharides for gradual and controlled release. Their biodegradability, eco-friendliness, and water-retention properties make them highly suitable for sustainable viticulture. Drones, as shown in Figure 3, can deploy hydrogels either by spraying them directly onto leaves with insecticides or by releasing them in dry form into the soil, where they absorb water during rainfall events.

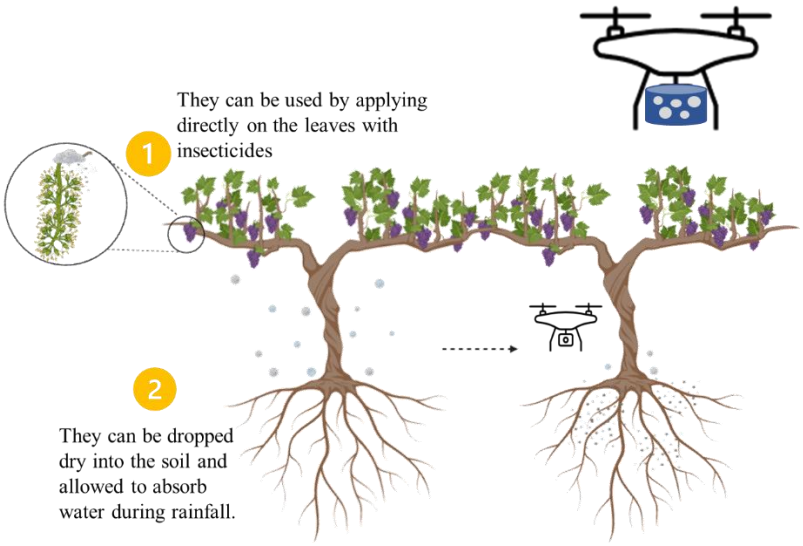

Figure 3. Example of deployment of drones spraying hydrogels onto leaves.

3.3.2. Socio-Economic Impact Assessment Framework

While these technological innovations are pivotal, they cannot be assessed in isolation. Hence, the project also considers the socio-economic and cultural implications of innovation in the wine sector. Key questions arise: Do such technologies contribute to the broader development of the territory? Do they enhance the region's attractiveness and long-term sustainability? Addressing these issues requires the use of multidimensional indicators. From a social perspective, one must examine workforce characteristics, training programs, and access to healthcare, education, and transportation. Economically, attention should be given to production volumes, sales trends, and the evolution of investments in innovation. From a tourist standpoint, the role of cultural, gastronomic, and artistic events, as well as the distribution and quality of accommodation facilities, becomes highly relevant.

By correlating these dimensions, it becomes possible to evaluate how family services, cultural activities, or corporate welfare initiatives may affect the profitability and competitiveness of local wine farms. Furthermore, the introduction of innovative technologies has the potential to increase employability, attract new professional profiles, and counteract depopulation trends in rural areas.

In sum, the integration of drones, multi-sensor platforms, predictive modeling, soil–microbiota interactions, and hydrogel applications, together with a careful evaluation of social, economic, and cultural impacts, constitutes a transdisciplinary strategy to address the multifaceted challenges of Irpinia. Innovation in viticulture thus emerges not only as a technological upgrade but also as a catalyst for territorial regeneration, linking agricultural modernization with sustainable development.

3.4. case study outcomes

The presented use case has investigated how transdisciplinary innovation frameworks can foster territorial development by combining advanced technological solutions with socio-economic and cultural dimensions. The research was structured around two complementary levels: (i) the Pathways to Innovation and Entrepreneurship program, designed to strengthen innovation capacity through

education and collaboration, and (ii) the applied project developed by participants, focusing on the valorization of Irpinia's viticulture through Agriculture 4.0 technologies.

Taken together, the program and the applied project reveal the dual potential of innovation frameworks: on the one hand, as a driver of human capital development and network strengthening; on the other, as a catalyst for concrete territorial transformation and economic revitalization. From a regional policy standpoint, the research strongly suggests the need for strategic investment in digital infrastructure, systematic curricular integration of innovation and entrepreneurship skills, and the development of incentive mechanisms that actively foster university–industry partnerships.

The research validates the hypothesis that transdisciplinary approaches, combining technological innovation with socio-cultural dimensions, can generate more resilient and sustainable development pathways than purely technology-driven or purely economic interventions. This integration creates multiplicative effects that benefit multiple stakeholders while preserving and enhancing territorial identity and cultural heritage.

Moreover, the program's success in creating lasting international collaborations demonstrates that the global innovation requires a world-wide multi-disciplinary approach to address universal challenges such as climate change, rural depopulation, and sustainable development.

4. Radar-Cross Section Analysis: Theoretical Framework and Simulation Studies

When investigating the radar cross section of emerging platforms such as unmanned aerial vehicles, establishing confidence in the computational methodology is a critical prerequisite. For this reason, validating the computational methodology by first conducting simulations on a well-characterized stealth platform, which incorporates advanced technologies for RCS reduction supported by available documentation , provides a robust foundation for establishing simulation accuracy and parameter optimization. This systematic validation approach ensures that when methodology is subsequently applied to unmanned aircraft platforms, the computational framework has been thoroughly tested against known EM behaviors, thereby enhancing confidence in the analysis of UAV radar cross section, where reference data may be limited or unavailable.

Hence, in the current section, a work about statistical analysis of the simulated RCS data for an F-35 aircraft model is presented. The core purpose of this research is to understand the F-35 radar cross section statistical behavior under various operational conditions and to identify the most suitable statistical models for describing these fluctuations which are critical for designing effective radar detection systems against stealth targets [34,35]. Moreover, these types of analysis are crucial also for designing radar receivers sensitive enough to indicate the presence of stealth-type targets.

The investigation encompasses three distinct operational scenarios defined by elevation aspect angle regimes: short-range (SR), medium-range (MR), and long-range (LR), engagements. Each regime represents different tactical scenarios where the aircraft may encounter radar systems, from beyond-visual-range interceptors to close-range surface-to-air missile systems. The analysis is conducted across three strategically important radar frequency bands: VHF (0.3 GHz), L-band (1 GHz), and X-band (10 GHz), which collectively represent the spectrum of modern radar systems from early warning radars to fire control systems.

This study employs the Mathworks Matlab™ simulation toolbox Physical Optics Facet Electromagnetic Scattering (POFACETS), developed at the Naval Postgraduate School of the University of Southern California, for high-fidelity RCS calculations. The software implements the physical optics approximation methodology for predicting the RCS characteristics of geometrically complex objects, where aircraft shapes are discretized using triangular facets, each possessing individual EM reflecting properties. This approach enables detailed modeling of the intricate surface geometries that define modern stealth aircraft while maintaining computational efficiency suitable for comprehensive parametric studies.

The analytical framework presented herein performs a rigorous first-order statistical characterization of the F-35 simulated RCS data across varying azimuth and elevation angles. The investigation systematically fits the simulated data against both mono-parametric and bi-parametric probability distributions commonly employed in radar target modeling and amplitude fluctuation analysis. The optimal distribution selection is determined through minimization of the Cramér-von Mises (CVM) distance metric, which provides robust comparison between theoretical and empirical cumulative distribution functions. Additionally, the spatial autocorrelation properties of the RCS signatures versus viewing angles are analyzed to characterize the angular decorrelation behavior, providing insights into the spatial coherence of the EM scattering patterns and their implications for tracking and engagement scenarios.

4.1. Theoretical Framework

In military context, one of the topics more investigated is the stealth technology (ST), also known as “low observable” [36]. As discussed in chapter 2, RCS depends on several factors as we know passive ST essentially exploits geometry of the object and the use of radar absorbing materials (RAM) to minimize the RCS [37], since it reduces the amount of the backscattered EM energy.

The goal of low observable technology is to reduce a variety of signature, including radio frequency (RF), infrared (IR), visible, laser, acoustic and magnetic aspects,

with RF signature reduction being of paramount importance in military applications.

The four primary techniques for RCS reduction are shaping, the use of RAM, passive cancellation and active cancellation.

- *Shaping*.
  Surfaces and edges of a stealth aircraft are designed to reflect radar energy away from the emitting sensor, rather than back to it. More specifically, bumps, curves, and external loads are avoided since they increase overall RCS.
- *RAM*
  RAM absorb part of the received radar energy and convert it into heat, thereby reducing reflected energy. However, they are not effective across all frequency bands and are considered a supplementary approach to shaping.
- *Passive Cancellation (Impedance Loading).*
  This technique currently is less considered, since it is difficult to implement for complex objects like aircraft. It involves creating a passive echo source that, with appropriate amplitude and phase, cancels another echo source.
- *Active Cancellation (Active loading).*
  Similar to the passive cancellation, this involves the target emitting EM energy synchronized with the received radar energy, with suitable and phase to minimize the reflected signal.

As response to the stealth technologies, anti-stealth technologies are developed and more and more investigated such as:

- Passive/Multistatic Radars.
- Very Low Frequency (VLF) Radars (VHF/UHF/L-Band).
- Over-The-Horizon Radars (OTHR).
- Infrared Detection Systems.
- Electronic Support Measures Passive Sensors.

It is commonly accepted that no single anti-stealth system is sufficient on its own. Instead, an effective counter to stealth threats requires a combination of radars, sensors, weapon systems, tactical data links, and appropriate tactics.

A comprehensive statistical analysis of their electromagnetic signature characteristics enables the identification of key detection parameters and the optimization of specialized algorithms for low-observable objects. This approach is also applicable to small UAS. which, as previously noted, exhibit stealth-like properties due to their minimal RCS, composite materials, and complex scattering behaviors that defy conventional radar detection assumptions. By leveraging these insights, it becomes possible to enhance surveillance systems for improved tracking of both advanced stealth platforms and small drones, which remain largely undetectable to traditional radar systems.

4.2. Methodology and Simulation Setup

4.2.1. POFACETS

The POFACETS software represents a comprehensive RCS prediction and analysis application [38]. Initially implemented in Matlab^{TM}, POFACETS has established itself as a cost-effective, user-friendly computational tool specifically designed for electromagnetic scattering analysis of complex three-dimensional objects with minimal computational resource requirements and practical execution times. The software's significance in contemporary electromagnetic warfare applications stems from its capability to address the complex challenges of RCS prediction for military platforms, which remains crucial for assessing target detectability and survivability characteristics. In Figure 4is reported an example of the main screen of the program.

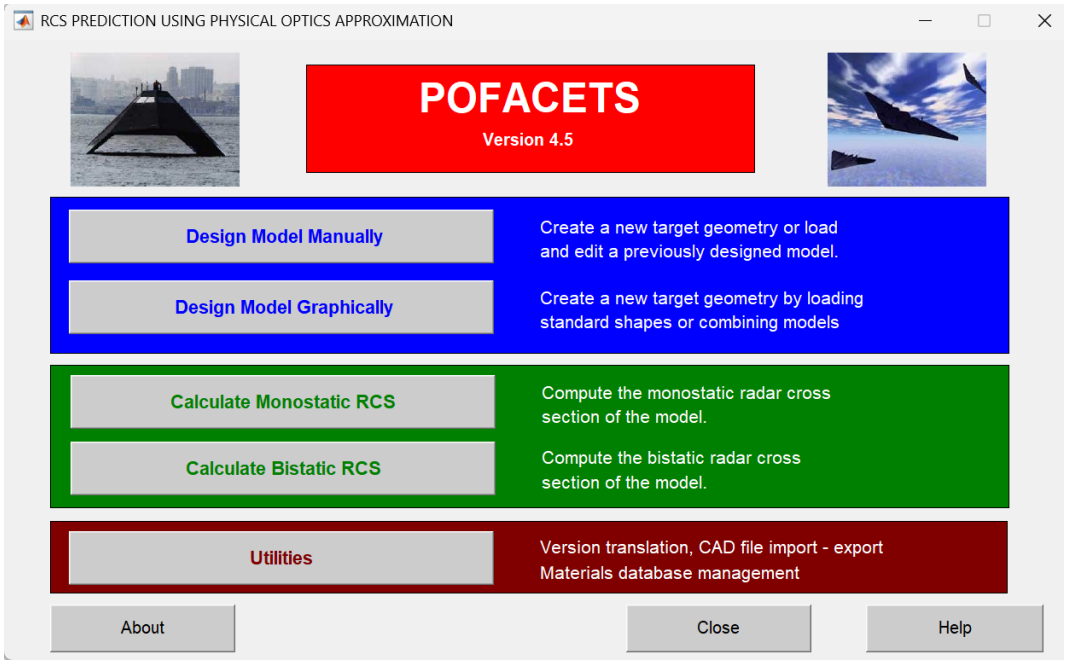

Figure 4. POFACETS v4.5 main screen.

The fundamental computational approach employed by POFACETS is based on the Physical Optics (PO) method, a high-frequency approximation technique that yields optimal performance for electrically large targets, particularly in specular reflection scenarios. The PO methodology estimates surface currents induced on target geometries by incident electromagnetic radiation through a simplified current distribution model: on directly illuminated surface portions, the induced current is assumed proportional to the incident magnetic field intensity, while shadowed regions are assigned zero current density. These determined current distributions are subsequently employed in far-field radiation integrals to compute the scattered electromagnetic field at distances significantly greater than the target dimensions.

The geometric representation of complex targets, such as the F-35, within POFACETS utilizes a triangular facet discretization approach, where aircraft surfaces are decomposed into numerous triangular elements, each characterized by specific electromagnetic properties including conductivity, permittivity, and surface treatment parameters. The total scattered field from the target is obtained through vector summation of electromagnetic contributions from all individual facets, enabling detailed modeling of geometrically complex platforms while

maintaining computational tractability for extensive parametric studies involving multiple frequency bands and comprehensive aspect angle coverage. Moreover, resistivity (whose value is normalized to that of free space equal to 377 Ω) is also associated with each facet.

Despite its computational efficiency and widespread application, the PO implementation in POFACETS incorporates several theoretical limitations that must be acknowledged when interpreting simulation results. The method abrupt transition to zero current density at shadow boundaries introduces computational inaccuracies in scattered field predictions at wide observation angles and within shadowed regions. Furthermore, the core PO implementation does not account for several complex electromagnetic scattering mechanisms including surface wave propagation, multiple reflection interactions, and edge diffraction phenomena, which can contribute significantly to total RCS under specific geometric and frequency conditions.

The software implementation in Matlab™, while providing accessibility and ease of modification, introduces computational constraints due to the interpreted language's inherent memory overhead and absence of GPU acceleration capabilities. Consequently, POFACETS is not classified as a high-performance electromagnetic simulator, limiting its application to scenarios where computational speed is not the primary constraint.

4.2.2. F-35 Aircraft Model and Simulation Configuration

The F-35, developed by Lockheed Martin [39], is one of the most popular example of stealth aircraft. Several research and studies about it are in continuous development, and there is a lot of documentation about different studies conducted to study the RCS under different frequency/polarization conditions [36,40–42].In [43] is reported an interesting analysis of the RCS for the F-22 Computer Aided Design (CAD) model, which is in size and shape very close to those of the F-35, showing pros and cons of using simulated models for RCS evaluation.

It is important to note that, unlike traditional stealth aircraft such as F-117A, B-2A, and F-22A, the F-35's stealth capability varies strongly with aspect and threat radar operating frequency [40]. It is optimized for the X-band and the upper S-band. More

specifically, it is described as 25% Very Low Observable (VLO) in the nose section, 25% Low Observable (LO) in the tail section, and 50% “reduced observable” in the beam sections, with strong frequency and angular dependance.

The F-35 Lightning II model employed in this analysis utilizes the predefined geometry available within the POFACETS software library, and it is described as a realistic model. This model captures the essential geometric features of the aircraft including its diamond-shaped wings, canted vertical stabilizers, integrated engine inlets, and faceted fuselage surfaces that contribute to its low-observable characteristics. The model represents the aircraft with overall dimensions of approximately 15.7 m in length (x-direction) and 10.7 m in wingspan (y-direction).

The POFACETS model for the F-35 is illustrated in Figure 5, where subplot (a) shows the used reference system emphasizing the azimuth φ and elevation θ angles, and subplot (b) shows the x-y view plane (i.e., the plane for θ = 90 deg).

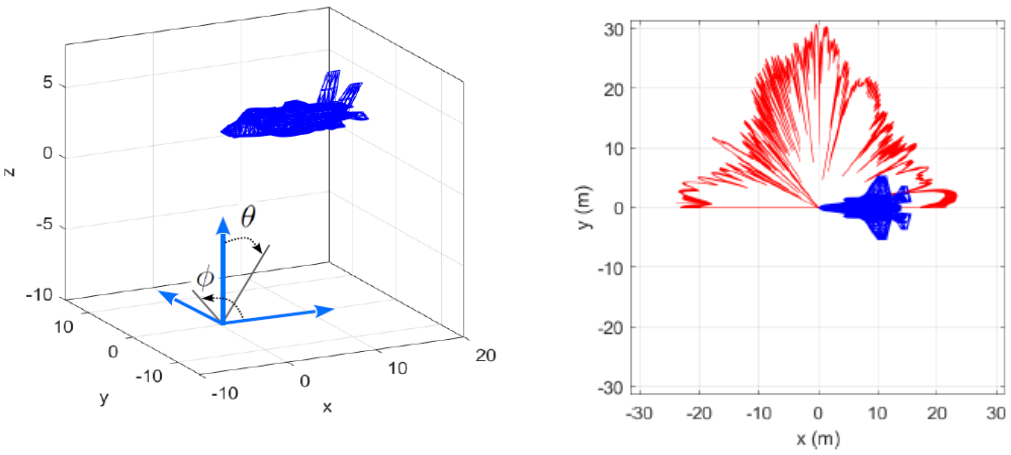

(a) (b)

Figure 5. Reference system (subplot a) and x-y view (subplot) of the F-35 overlapped with the polar plot of its RCS in dBsm. The RCS is evaluated for elevation angles in the interval [98, 100] degrees and at an L-band operating frequency of 1 GHz.

Hence, the RCS for the F-35 is computed for a monostatic radar, with the scattered field evaluated for each triangle alone, excluding all multiple reflection and diffraction effects. For the current simulations, the RCSs are computed setting the polarization of the incident wave to be a pure transverse mode (TM). Regarding the

considered aspect angle, the data are processed for the azimuth angle φ varying in the interval [0°, 180°] (only one half is accounted for due to symmetry), with a step size of 0.1°. Then, the elevation angle θ is set in order to comply with three different range regimes referred to as SR, MR, and LR [40], for which $\theta \in [120, 122]$ deg, $\theta \in [118,120]$ deg, and $\theta \in [98,100]$, respectively. Finally, data are generated for a transmitted wave at three different frequencies, viz., 0.3 GHz (VHF -band), 1 GHz (L-band), and 10 GHz (X-band). The resulting RCS for the LR regime with an operating frequency of 1 GHz (L-band) is also shown overlapped to the target with a polar plot in Figure 5-(b).

To better understand the RCS behavior as a function of view angle, Figure 6, Figure 7 and Figure 8 show the RCS results calculated for the F-35 aircraft with the three different operating frequencies and under the considered range regimes. Beyond the curves representing thee RCS data computed for each aspect angle (blue curves), the mean value with respect to the elevation is also plotted (red curve).

It is important to note that the simulation does not incorporate the effects of RAM coatings typically applied to operational F-35 aircraft. This limitation results in simulated RCS values that are significantly elevated compared to the actual platform's electromagnetic signature, with peak values reaching approximately 5 dBsm at specific aspect angles, representing increases of 10 dB or more above expected operational values. In [41] to overcome this drawback, the model for the F-35 has been changed, removing the aircraft nose to simulate the transparency in terms of RCS. Despite this limitation, the geometric accuracy of the model ensures that the angular dependencies and statistical characteristics of the RCS fluctuations remain representative of stealth platform behavior.

Moreover, it is interesting to note that at lower frequencies (i.e., VHF), due to Rayleigh scattering, the stealth capabilities of the target are significantly reduced, allowing the radar to detect it more easily. Subplots (a) and (b) of Figure 6,Figure 7, Figure 8 show higher average RCS values compared to the others.

Figure 6, Figure 7, Figure 8 illustrate the RCS behavior of the F-35 in the three operational regimes (SR, MR, LR) across VHF, L-, and X-bands. A clear trend emerges:

Short-Range (Figure 6): higher and more fluctuating RCS values are observed, particularly at VHF, where stealth effectiveness is strongly reduced. At higher frequencies, sharper oscillations appear, indicating increased sensitivity to angular variations.

Medium-Range (Figure 7): the average RCS decreases compared to SR, with smoother angular fluctuations, especially in the VHF and L-bands. However, localized peaks remain at higher frequencies, highlighting potential detection angles.

Long-Range (Figure 8): the mean RCS is further reduced, especially in the X-band, where even small angular changes produce noticeable variations in radar return. This confirms that stealth performance improves with distance but becomes more sensitive to fine angular resolution at higher frequencies.

Overall, these results show that frequency and operational regime act in a complementary manner: lower frequencies tend to reduce the effectiveness of stealth shaping, making the aircraft more visible, while higher frequencies enhance stealth performance but increase the angular variability of the radar signature.

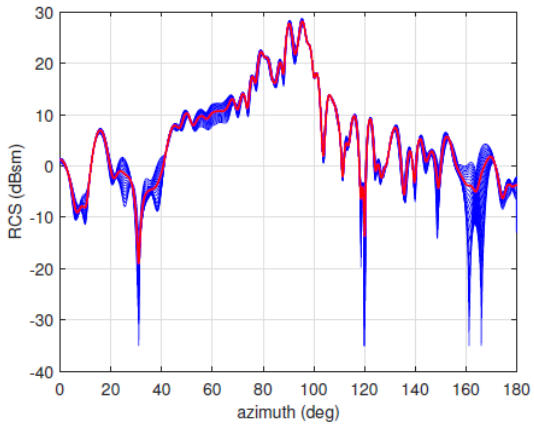

(a)

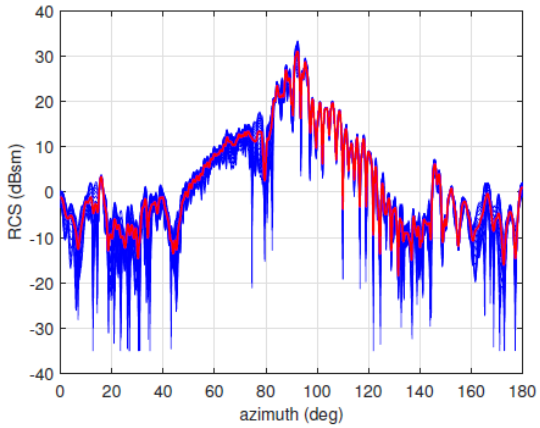

(b)

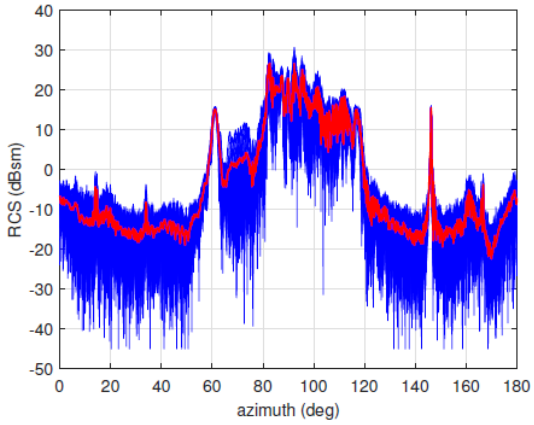

(c)

Figure 6. RCSs (dBsm) (blue line) and its mean value (red line) versus azimuth (in degrees) of the F-35 aircraft, for the three considered frequency band (i.e., VHF, L, and X, from top to bottom) under the SR regime.

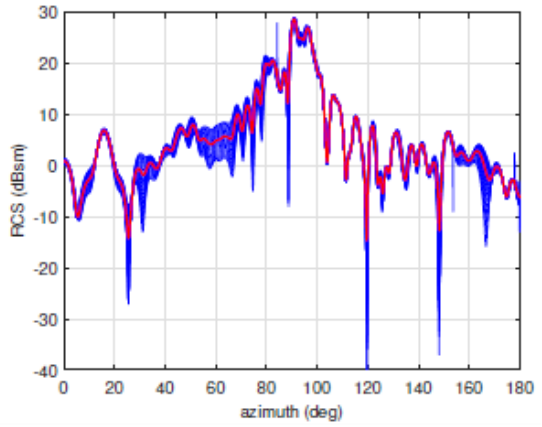

(a)

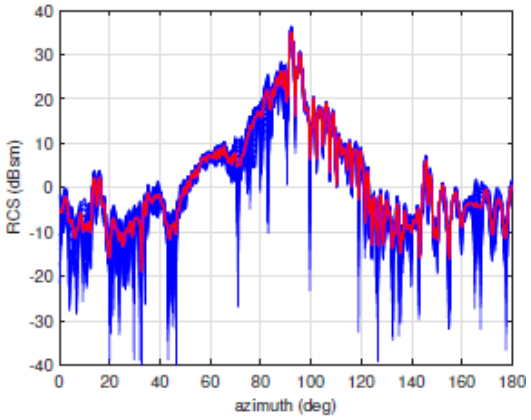

(b)

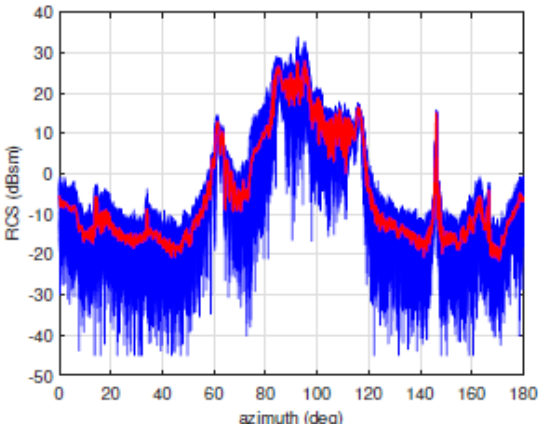

(c)

Figure 7. RCSs (dBsm) (blue line) and its mean value (red line) versus azimuth (in degrees) of the F-35 aircraft, for the three considered frequency band (i.e., VHF, L, and X, from top to bottom) under the MR regime.

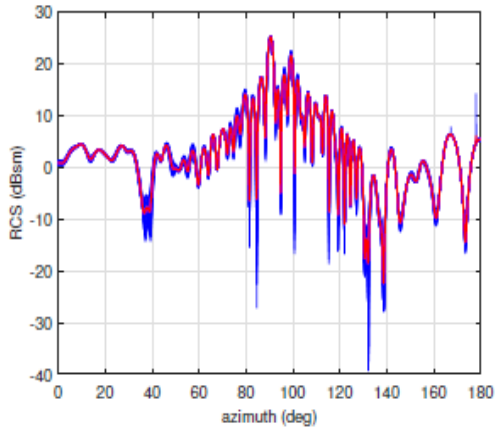

(a)

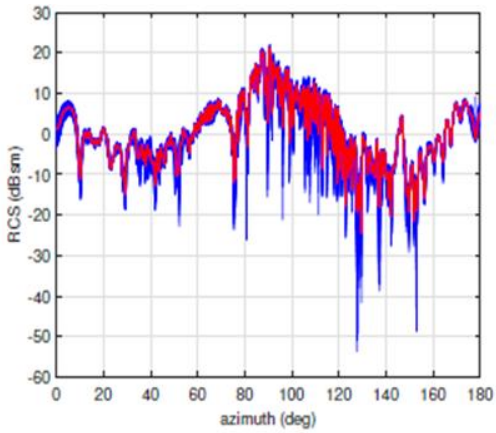

(b)

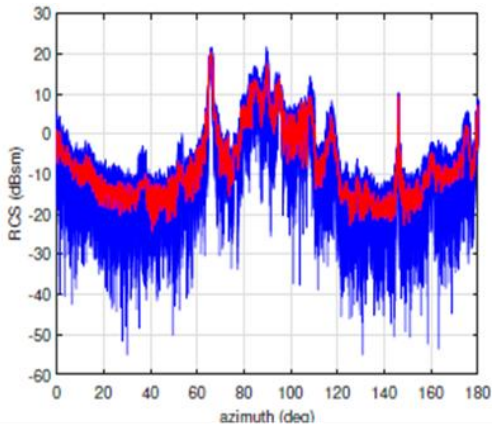

(c)

Figure 8. RCSs (dBsm) (blue line) and its mean value (red line) versus azimuth (in degrees) of the F-35 aircraft, for the three considered frequency band (i.e., VHF, L, and X, from top to bottom) under the LR regime.

4.2.3. Statistical analyses by moment matching

Typically, the method used to assess radar detection performance relies on the premise that the RCS of the target follow one of the Swerling models I-V [44] Nevertheless, some examples of practical application have shown that amplitude fluctuations are not always consistent with the above models, which can lead to discrepancies between the real-word radar performance and the theoretical one. In literature, several alternative parametric fluctuation models have been proposed to address this issue, including Weibull, Log-normal, K, and so on [44,45]. Radar detection performance can be accurately predicted with high precision when the statistical behavior of the RCS is properly characterized and comprehensively described. To achieve this objective, as mentioned before this section presents a thorough statistical analysis of the simulated RCS signatures of the F-35 aircraft, in line with [45,46].

The adopted methodology involves fitting the simulated data using well-established statistical distributions from the scientific literature, including both mono-parametric and bi-parametric models. These distributions are analyzed across a comprehensive range of aspect angles and at frequencies of operational interest. The focus is specifically on the first-order statistical analysis aimed at deriving the optimal model representing the fluctuation characteristics of F-35 RCS data with respect to viewing angle variations.

The analysis centers on the cumulative distribution function (CDF) of the square root of RCS ($\sqrt{\sigma}$), with results consistently confirming significant deviations of the experimental data from simple mono-parametric distributions such as the classical Rayleigh model, strongly favoring more sophisticated bi-parametric distributions that better capture the complex scattering behavior of stealth aircraft.

The empirical cumulative distribution function (ECDF) derived from the simulated data is systematically compared to five well-established theoretical models commonly employed in the literature for describing amplitude statistics: Rayleigh, K-distribution, Weibull, Gamma, and Log-Normal distributions. The parameters for each distribution are estimated from the data using robust moment matching techniques, ensuring optimal fit quality across the parameter space.

These distributions encompass a wide range of statistical behaviors, from the simple exponential decay of Rayleigh statistics to the more complex heavy-tailed characteristics of K-distribution and Log-Normal models [47].

Table 2 summarizes the analytic expression of the above described CDF also indicating their related parameters. Note that, the functions $\Gamma(\cdot)$, $\gamma(\cdot)$, and erf$(\cdot)$ in the table denote the Gamma, the incomplete Gamma, and the error functions, respectively.

Table 2. Theoretical CDF and their parameters

Distribution	**CDF**	**Parameters**	**Support**
Rayleigh	$F(x;b^2) = 1 - \exp\left(-\frac{x^2}{2b^2}\right)$	$b^2 < 0$	$x \geq 0$
K	$F(x;\mu,\nu) = 1 - \frac{1}{2^{\nu-1}\Gamma(\nu)}\left(\sqrt{\frac{2\nu}{\mu}}\right)^{\nu} K_{\nu}\left(\sqrt{\frac{2\nu}{\mu}}x\right)$	$\mu > 0$ (scale) $\nu > 0$ $(shape)$	$x \geq 0$
Weibull	$F(x;\mu,\nu) = 1 - \exp\left[-\left(\frac{x}{\mu}\right)^{\nu}\right]$	$\mu > 0$ (scale) $\nu > 0$ $(shape)$	$x \geq 0$
Gamma	$F(x;\mu,\nu) = \frac{1}{\Gamma(\nu)}\gamma\left(\nu,\frac{x}{\mu}\right)$	$\mu > 0$ (scale) $\nu > 0$ $(shape)$	$x \geq 0$
Log-Normal	$F(x;\mu,\nu) = \frac{1}{2} + \frac{1}{2}\text{erf}\left(\frac{log(x)-\mu}{\sqrt{2s}}\right)$	$\mu \in (-\infty,+\infty)$ $s > 0$	$x > 0$

Finally, the theoretical model that provides the best fit respect to the data is selected as the one minimizing an integral distributional distance between the designed CDF and the ECDF, referred to as the CVM distance [48]. More precisely, N denote as $\sigma_1, \sigma_2, \ldots, \sigma_N$ the set of RCS values, the CVM distance between the design distribution $F(\sqrt{\sigma})$ and its empirical counterpart can be computed as

$$d^2 = \frac{1}{12N} + \sum_{i=1}^{N}\left|F\left(\sqrt{\sigma_i}\right) - \frac{2i-1}{2N}\right|^2, \qquad (3)$$

where σ_i denotes the i-th ordered statistic from above set of RCSs.

4.3. Results and Statistical Analysis

In Figure 9, Figure 10, and Figure 11 the theoretical CDF for the five considered models whose parameters (see Table 2) are estimated form the available data, together with their ECDF. Subplots (a), (b) and (c) are referred in sequence to the above defined VHF-, L-, and X-bands (observing he figures from top to bottom) and under the SR, MR and LR regime respectively. Across all analyzed scenarios, visual inspection reveals that the F-35 RCS data strongly deviates from the commonly assumed Rayleigh distribution. This consistent deviation indicates that the traditional single-parameter exponential model is inadequate for characterizing the complex scattering behavior of stealth aircraft. Instead, bi-parametric models demonstrate superior capability in describing the statistical behavior of the RCS measurements.

Using the CVM distance criterion as the selection metric, the analysis identifies optimal distribution models for each frequency band and radar regime combination. In the LR regime, the Log-Normal distribution is consistently selected as the best fit across all frequency bands, including VHF, L-band, and X-band scenarios. The MR regime shows similar behavior, with Log-Normal distributions providing optimal fits for VHF and L-band cases, while the X-band represents a notable exception where the Weibull distribution achieves the minimum distance. The SR regime demonstrates a different pattern, where the Log-Normal distribution remains optimal for VHF-band, but Weibull distributions are selected as best fits for both L-band and X-band frequencies. All the results are summarized in Table 3.

Table 3. Best fit theoretical CDF and their parameters of the RCS data

Scenario	Selected CDF	Estimated parameters
VHF-SR	Log-Normal	$\hat{\mu} = 0.6502 \quad \hat{s} = 1.0410$
L-SR	Weibull	$\hat{\mu} = 1.8761 \quad \hat{v} = 0.5960$
X-SR	Weibull	$\hat{\mu} = 1.1171 \quad \hat{v} = 0.5630$
VHF-MR	Log-Normal	$\hat{\mu} = 0.5025 \quad \hat{s} = 1.0913$
L-MR	Log-Normal	$\hat{\mu} = 0.2590 \quad \hat{s} = 1.3068$
X-MR	Weibull	$\hat{\mu} = 0.9945 \quad \hat{v} = 0.5140$
VHF-LR	Log-Normal	$\hat{\mu} = 0.2532 \quad \hat{s} = 1.0410$
L-LR	Log-Normal	$\hat{\mu} = 0.0374 \quad \hat{s} = 1.0410$
X-LR	Log-Normal	$\hat{\mu} = -1.0121 \quad \hat{s} = 1.1608$

The Log-Normal distribution, characterized by parameters μ (mean of the logarithm) and σ (standard deviation of the logarithm), exhibits consistent behavior across different regimes. In both LR and MR regimes, the parameter μ does not exceed 0.5025, while σ oscillates around unity. The SR regime shows a slight variation with μ approximately equal to 0.65, while σ remains close to 1.0. The parameter μ shows a slight increase in the SR regime compared to LR/MR regimes, suggesting that higher resolution measurements may capture additional scattering mechanisms that shift the distribution characteristics.

The Weibull distribution, defined by scale and shape parameters, shows frequency-dependent behavior. In the MR regime, specifically for the X-band case, the scale parameter is approximately 1.0 while the shape parameter is close to 0.5. The SR regime exhibits more complex behavior with the L-band scenario showing a scale parameter of about 1.9 and shape parameter of approximately 0.60, while the X-band case presents a scale parameter of about 1.12 and shape parameter of around 0.56. The scale parameter exhibits significant variation between L-band and X-band

in the SR regime, indicating frequency-dependent scattering characteristics that become more pronounced at higher resolutions.

Summarizing, the analysis reveals distinct patterns in model selection based on radar resolution. More specifically, Figure 9, Figure 10, and Figure 11 illustrate the comparison between the CDFs and the ECDFs of the square root of the RCS ($\sqrt{\sigma}$) for the F-35 aircraft under the SR, MR and LR, respectively. The data are presented for three radar frequency bands: BHF, L-band, and X-band, from top to bottom. LR and MR regimes predominantly favor Log-Normal distributions, with only one exception in MR X-band where SR regime shows increased preference for Weibull distributions in higher frequency bands, specifically L- and X-bands, while maintaining Log-Normal for VHF.

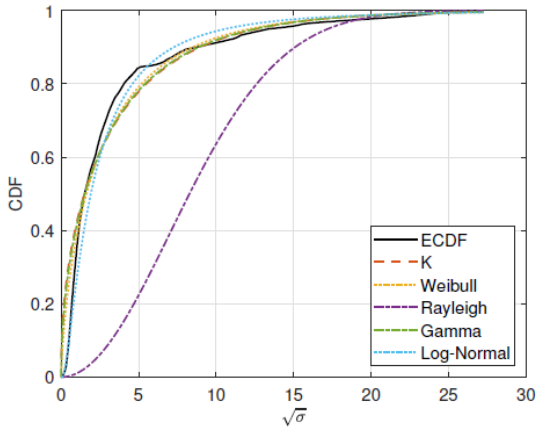

(a)

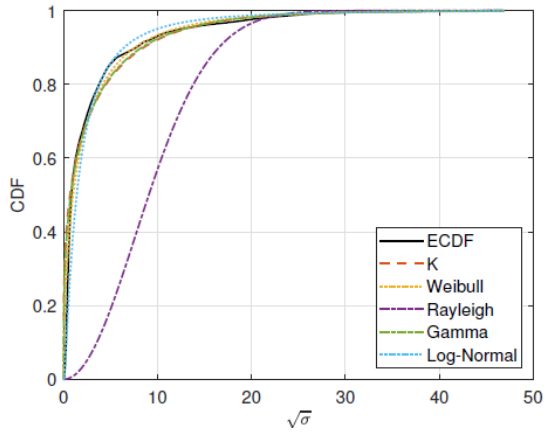

(b)

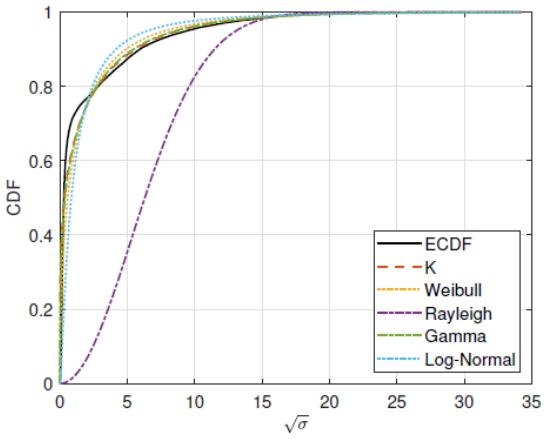

(c)

Figure 9. Theoretical CDF and ECDF versus $\sqrt{\sigma}\ of$ the F-35aircraft, for the three considered frequency bands (i.e., VHF, L, and X, from top to bottom) under the SR regime.

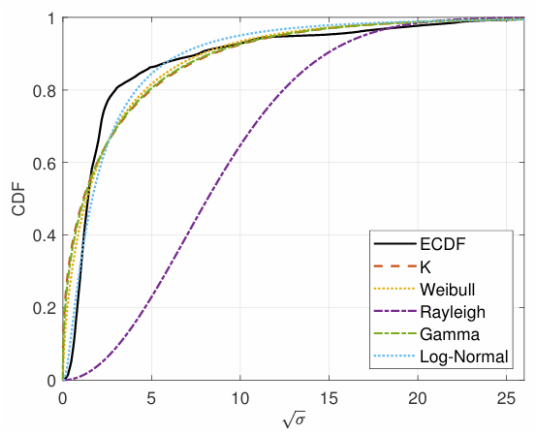

(a)

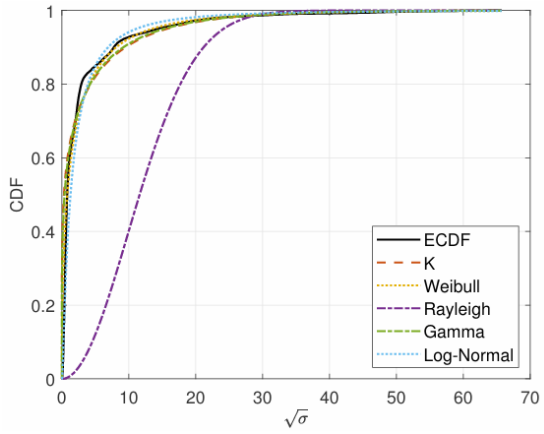

(b)

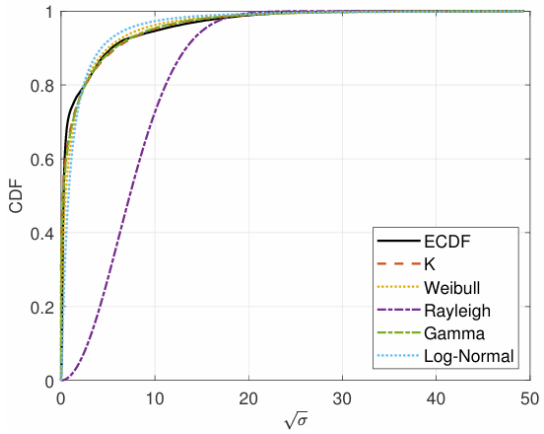

(c)

Figure 10. Theoretical CDF and ECDF versus $\sqrt{\sigma}$ of the F-35aircraft, for the three considered frequency bands (i.e., VHF, L, and X, from top to bottom) under the MR regime.

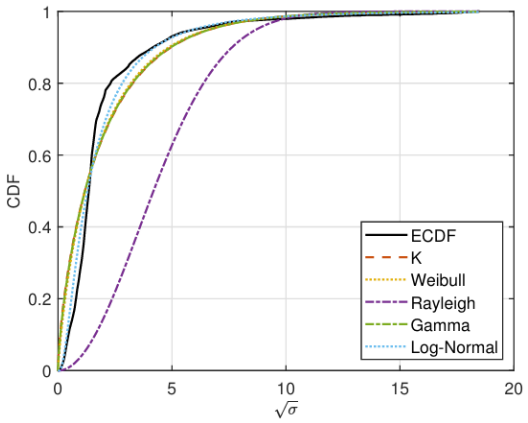

(a)

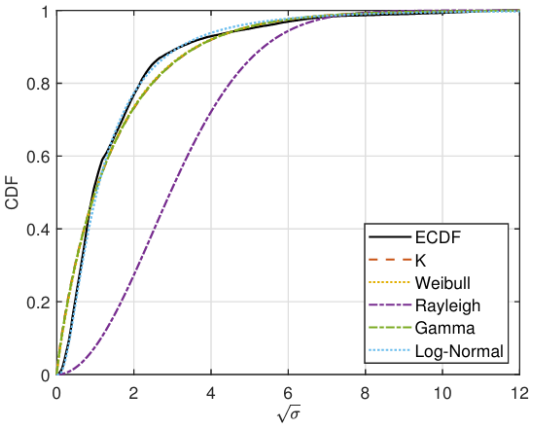

(b)

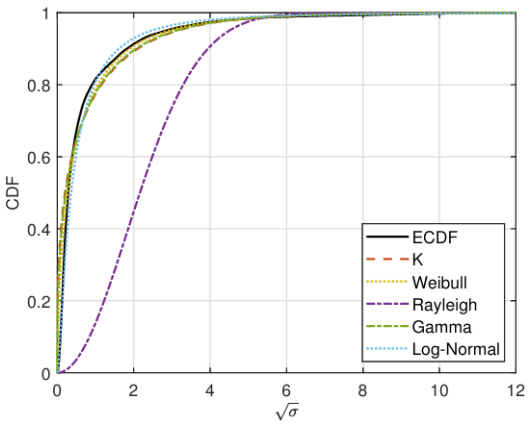

(c)

Figure 11. Theoretical CDF and ECDF versus $\sqrt{\sigma}$ of the F-35aircraft, for the three considered frequency bands (i.e., VHF, L, and X, from top to bottom) under the LR regime.

Before concluding this study about the F-35 aircraft RCS, the spatial decorrelation behavior is also analyzed as the operating frequency varying as well as for the two considered elevation aspect regimes. Precisely, indicating with L_W the length expressed in meters, the spatial (angular) decorrelation can be evaluated as [49]:

$$\Delta\theta_d = \frac{c}{2L_W f_0}, \tag{4}$$

Where $c = 3 \times 10^8$ m/s is the speed of light and f_0 is the carrier operative frequency. For the F-35 aircraft herein considered, its size id 15.7m in x-direction and 10.7 m in the y-direction as mentioned before [39], therefore a minimum and maximum spatial autocorrelation can be derived, respectively. The resulting values for the spatial autocorrelation (averaged over elevation) are plotted in where the angle at which the spatial decorrelation occurs according to (4) is also plotted as a vertical bar. From Figure 12, Figure 13, and Figure 14 inspection is possible to appreciate that as the frequency increases, there is a narrowing of the autocorrelation mainlobe. This effect is even more evident in the SR regime.

Certainly, the RCS of the F-35 has the tendency to decorrelate the faster the higher the observation frequency is. Therefore, in the X band even very small changes in the angle of view lead to significant changes in the RCS, such that they could lead to detection losses by the radar.

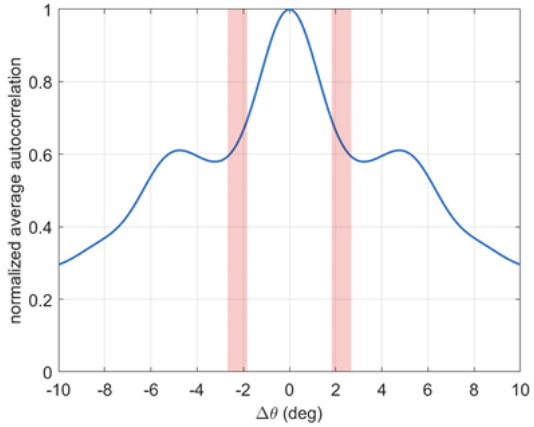

(a)

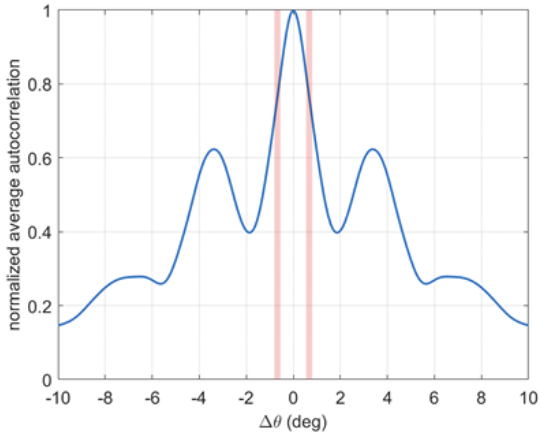

(b)

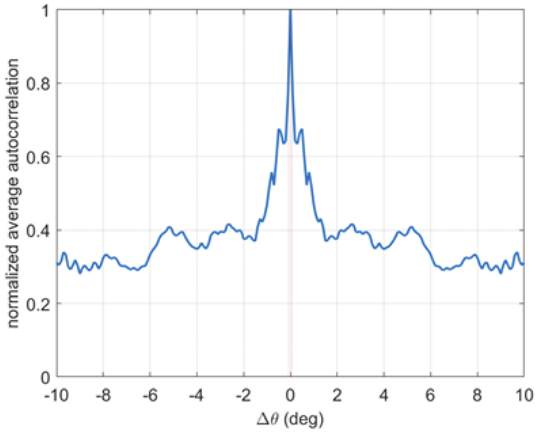

(c)

Figure 12. Normalized average autocorrelation of the RCS of the F-35aircraft, for the three considered frequency bands (i.e., VHF, L, and X, from top to bottom) under the SR regime.

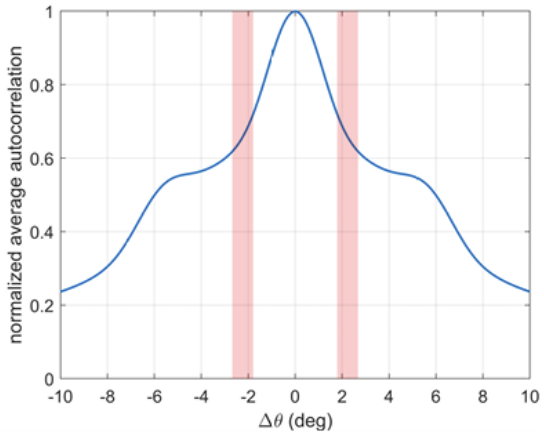

(a)

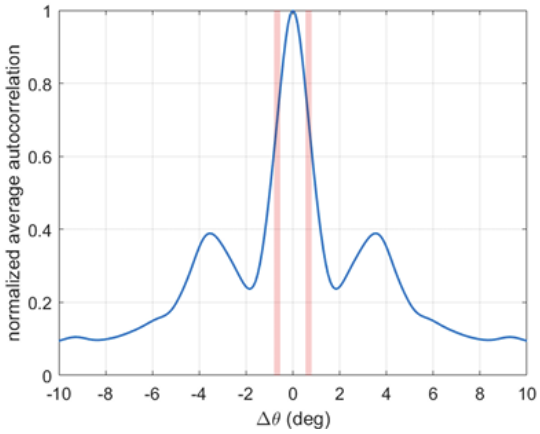

(b)

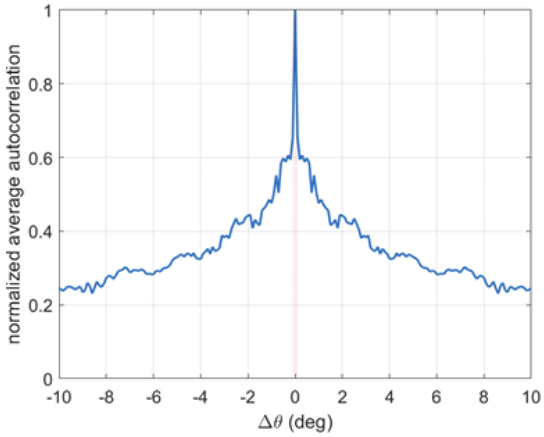

(c)

Figure 13. Normalized average autocorrelation of the RCS of the F-35aircraft, for the three considered frequency bands (i.e., VHF, L, and X, from top to bottom) under the MR regime.

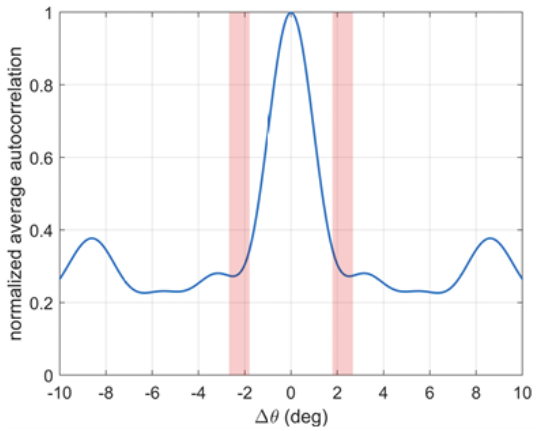

(a)

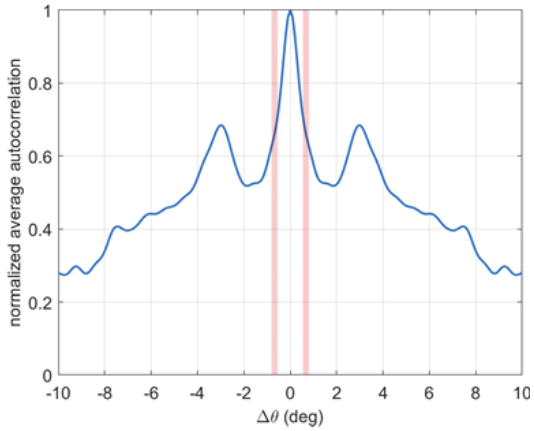

(b)

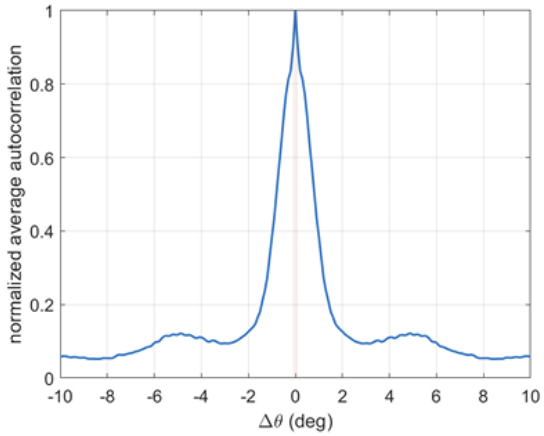

(c)

Figure 14. Normalized average autocorrelation of the RCS of the F-35aircraft, for the three considered frequency bands (i.e., VHF, L, and X, from top to bottom) under the LR regime.

5. Multi-Platform Detection Systems Simulation:

The growing proliferation of unauthorized drones in protected airspace represents a significant threat to security and privacy, particularly in urban environments. This issue creates an urgent need for developing more reliable and comprehensive surveillance networks. Moreover, traditional surveillance systems based on single sensors have inherent limitations that compromise their effectiveness in complex scenarios. Therefore, the fusion of data from heterogeneous sensors proves to be the key to achieving comprehensive situational awareness and improving tracking accuracy.

Building on the considerations outlined in the previous chapter, the integration of UAVs into controlled airspace presents additional challenges that extend beyond the issue of their reduced radar cross-section. These challenges have prompted a comprehensive investigation into suitable simulators for analyzing RCS characteristics, as well as identifying statistical algorithms that best capture drone signatures.

Regarding drone surveillance specifically, traditional air traffic surveillance systems demonstrate significant inadequacies when applied to drone detection and tracking scenarios, as they were originally designed for conventional manned aircraft. While conducting accurate RCS analysis is certainly valuable for designing radars better suited to drone surveillance, this approach alone is insufficient. An equally critical aspect to investigate is the fusion of multiple surveillance systems, aimed at enhancing the detection, identification, and tracking capabilities for small unmanned aerial vehicles.

For this reason, the current research focuses on employing the BlueSky Air Traffic Control (ATC) Simulator to investigate multi-sensor fusion approaches that combine radar and acoustic surveillance technologies. The primary objective is to minimize prediction errors in trajectory estimation while enhancing detection accuracy and tracking reliability for small unmanned systems. More specifically, this research evaluates surveillance performance for two non-cooperative drones

executing distinct flight trajectories within a shared operational airspace, providing a foundational framework for more complex multi-target scenarios.

5.1. System Architecture and Design Framework

5.1.1. Architecture Selection: Centralized vs Decentralized

Before defining the project's implementation steps, a critical decision must be made regarding the architectural paradigm: centralized or decentralized. This choice significantly impacts system performance, robustness, scalability, and, critically, the effectiveness of state estimation algorithms like the Kalman filter.

In centralized architecture, shown in Figure 15, an autonomous central management unit processes all data and makes decisions accordingly. All information about aircraft state (position, velocity, intent, etc.) is fed into this central service, typically from surveillance systems or operators via air-to-ground or ground-to-ground communications [50]. Flight authorizations, conflict resolution procedures, risk assessments, and operator notifications are all processed and disseminated by the central authority. This creates a unified decision-making framework where all unmanned aircraft operations within the designated airspace are subject to centralized oversight and control. Centralized architecture inherently limits system scalability, as the overall capacity is constrained by the computational power and infrastructure resilience of the central system. Furthermore, this model introduces potential vulnerabilities, as the entire network's functionality depends on the continuous operation of the central infrastructure. Any disruption to the central system, whether through technical malfunction or cybersecurity incidents, can compromise the operational integrity of the entire U-Space network.

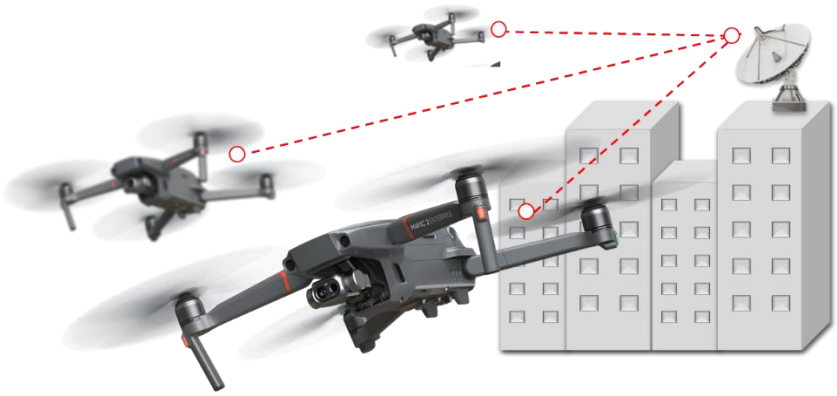

Figure 15. Example of Centralized Architecture for UTM.

The main advantages and disadvantages of centralized architecture are summarized as in Table 4, following several literature documents such as [50,51] .

Table 4. Advantages and disadvantages of Centralized Architecture for UTM.

Advantages	Disadvantages
Ensures global situational awareness	Higher latency due to data transmission to a central point
Easier to cybersecurity and authentication measures	Risk of a single point of failure
More effective fusion of multisensory data for high accuracy	Limited scalability
High accuracy in data fusion	Performance can be adversely affected by modeled input errors
Easier Synchronization of data across the system	Performance is significantly degraded by modeled transmission errors of resolution maneuvers
More effective filtering algorithms	May not be suitable for high volume traffic operation
Facilitates prioritization and sequential resolution of conflicts based on estimated time until conflict	The system relies on a central server, which acts as a bottleneck requiring continuous communication with other actors

In a decentralized architecture, shown in Figure 16, conflict resolution functions might reside onboard individual aircraft. This approach typically relies on predefined rules or protocols to compute and execute their own maneuvers without necessarily knowing others' actions in real-time. Different models exist, including uniform rule-based, coordination-based, and mixed rule-based approaches [50].

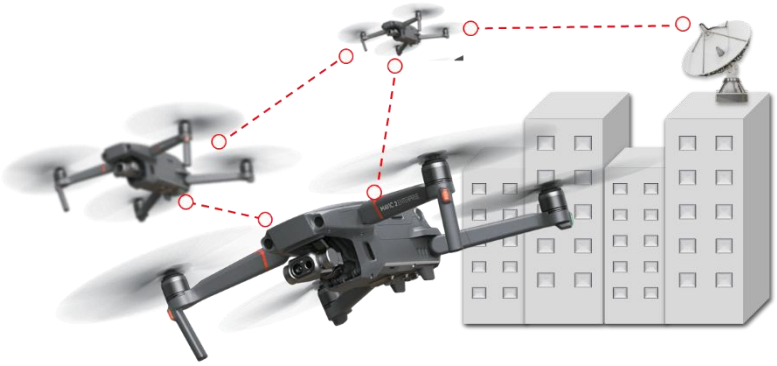

Figure 16. Example of Decentralized Architecture for UTM.

Also for the decentralized architecture, advantages and operational limitations are summarized in Table 5 .

Table 5. Advantages and disadvantages of Decentralized Architecture for UTM

Advantages	**Disadvantages**
Lower latency	More complex fusion algorithms
Greater robustness and redundancy	Potential synchronization issues among different nodes and higher computational load on individual nodes
Easier scalability	Requires a fully connected network graph for consensus-based tracking
Less vulnerable to output reception errors, as resolution maneuvers are computed and executed onboard, eliminating the need to communicate them	Communication delays could lead to conflicting state estimates

The selection between these two architectures depends on several critical factors that must be evaluated within the context of specific operational requirements and constraints, including:

- Traffic density and operational complexity;
- Infrastructure requirements;
- Regulatory environment;
- Risk tolerance.

Beyond these general considerations, the architectural choice is critically linked to state estimation requirements, particularly those associated with the Kalman Filter (KF) and its extensions such as the Extended Kalman Filter (EKF). The KF is a recursive stochastic filter that corrects predicted states using the weighted error between actual and predicted measurements. Specifically, it operates by propagating the mean and covariance of the state through time [52].

A fundamental requirement for achieving optimal state estimation with a Kalman filter is system observability. Without full observability, the filter cannot guarantee convergence to the true state. This condition is frequently compromised in decentralized networks, where individual nodes typically access only partial measurements and must exchange information with neighboring nodes to enhance overall system observability.

Given these technical constraints, while decentralized systems offer inherent advantages in terms of robustness and scalability for general UAM scenarios, this project's emphasis on comprehensive, high-accuracy multi-sensor fusion necessitates careful consideration of observability requirements. The specific demands of the KF as a core component for error prediction and state estimation lead to the selection of a centralized architecture to ensure optimal surveillance performance and state estimation accuracy.

5.1.2. System Design Overview

Once the UTM architecture type has been selected for the simulation, considering all the different requirements for sensor fusion, the system design is established. The objective is to recreate a comprehensive surveillance scenario incorporating two primary sensor types for drone monitoring: radar systems and acoustic sensors.

> This phase involves creating the operational scenario within the BlueSky ATC Simulator environment. The development process includes:
>
> a) Defining the operational area where drones will be deployed.
> b) Developing specialized plugins for various surveillance sensors.
> c) Establishing the foundational simulation framework.

This research specifically is centered on *the scenario creation and development* phase of the project, focusing on reconstructing a realistic operational scenario involving two small drones. More in particular, This phase involves creating the operational scenario within the BlueSky ATC Simulator environment. As it possible to note from Figure 17, the development process includes:

- Defining the operational area where drones will be deployed.

- Developing specialized plugins for various surveillance sensors.
- Establishing the foundational simulation framework.

The simulation environment provides a controlled testbed for evaluating sensor performance and fusion algorithms.

A critical aspect of this research addresses non-cooperative drone operations, which presents significant challenges for airspace management. In these scenarios, drones or other airspace users may not provide active signals or identification, creating potential security risks. The difficulty of managing such traffic requires external surveillance technologies, such as radar systems and acoustic sensors chosen for the project. Non-cooperative systems are especially critical for protecting sensitive airspace like airports or urban areas. They enable authorities to identify and address potential risks posed by unidentified or unauthorized airspace users.

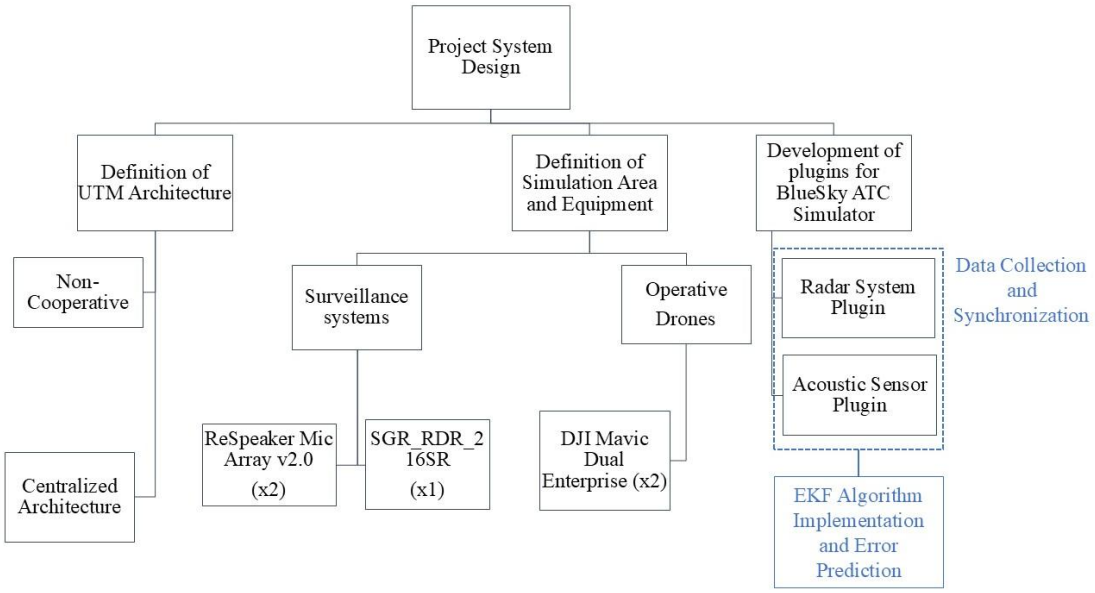

Figure 17. Project System Design

5.1.3. BlueSky ATC Simulator Platform

As simulation environment, BlueSky ATC Simulator [53] is used. The latter is born by an initiative by Delft University of Technology (TU Delft), which operates as a fully open-source and open data air traffic simulation tool with the aim to enhance

the comparability of Air Traffic Management (ATM) research. Its design prioritizes user-friendliness and high fidelity while avoiding proprietary data.

BlueSky is built with a modular setup to allow an easy extension of its functionality without requiring users to understand the entire source code. The main modules include:

- Simulation control (*sim*), a module that manages the main simulation loop and mode, initializing other modules, potentially in multiple threads.
- Command Stack (*stack*), which is basically the central processing unit of BlueSky. It receives commands from the user via the graphical user interface (GUI) console, mouse clicks, or even external programs through network connections.
- Traffic Module (*traf*), that holds all data related to simulated traffic, including the state of aircraft, its performance databases, and navigation data.
- User Interface (UI).
- Classic GUI, based on Pygame.
- Advanced GUI, a version that uses OpenGL in a Qt windows environment. b
- Tools Module, that contains functions for aerodynamics and navigation calculation, and data logging.

5.2. Experimental Setup and Implementation Framework

To proceed with Phase 1 implementation and to establish the foundation for subsequent project phase, a comprehensive experimental setup is designed. This experimental configuration satisfies the technical requirements for realistic non-cooperative drone scenario reconstruction while ensuring the controlled conditions necessary for rigorous sensor performance evaluation.

As surveillance systems selected for the current simulation are one radar system and two acoustic sensor. Their selection is driven by the following criteria necessary for the definition of the plugins for the simulation:

- *Independent Development*: the choice of different sensor technologies naturally supports the formation of independent development teams. Each technology demands distinct expertise domains (e.g., RF engineering for radar, signal processing for acoustics, minimizing technical overlap and resource conflicts while fostering focused, specialized development efforts.
- *Isolated Testing*: selected sensors can be tested and validated independently before system integration. Moreover, their accuracy, range limitations, and false alarm rates can be established through isolated protocols.
- *Scalability*: the e modular design should accommodate potential integration of additional sensor types (optical cameras, LiDAR, RF spectrum analyzers) without requiring fundamental architecture modifications.
- *Maintenance and Reliability*: the use of multiple sensor enhances system resilience by isolating faults to individual technologies, allowing independent updates and maintenance without system-wide downtime. At the same time, it is important to pay attention to not add more sensors than necessary to avoid redundancy.

In particular, the selected surveillance systems:

- SGR_RDR-216SR-1S10K-3D [54], that is an S-Band security radar equipped with a phased array system that combines mechanical azimuth scanning with electronic elevation scanning. Using pulse Doppler technology, it can detect and tracking intrusion targets in three-dimensional space. Distance, altitude, azimuth, and velocity are given as output parameter providing also a reliable situational awareness. In Table 6 with all the system's parameters of the sensor are reported.

- ReSpeaker Mic Array v2.0 [55], as acoustic sensors. The sensor, shown in Figure 18, is equipped with four digital MEMS microphones (MP34DT01TR-M), labeled (2), each spaced 45.7 mm apart. These microphones transmit their signals to the central integrated circuit (IC), an XMOS XVF-3000. This IC outputs audio through the 3.5 mm jack (5) and the USB-B port (4) located at the bottom of the board. It also includes an internal beamformer that estimates the direction of arrival (DOA) of

incoming sound. The DOA values are sent both to the USB port and to the LED ring (3), which provides a visual indication of the sound source direction. On a connected device such as a laptop, these USB-transmitted values can be accessed via a Python script. The array operates at a sampling frequency of 16 kHz, allowing analysis of audio signals up to 8 kHz, as dictated by the Nyquist criterion. Additionally, the board integrates a stereo codec with speaker drivers (6), through which the signal from (1) passes before reaching output (5). However, this feature was not employed in the present project.

It is important to note that the use of acoustic sensors is primarily intended to compensate for the high costs of more reliable and widely adopted solutions such as radar. In this case, however, the goal is to integrate them with radar systems to reduce detection errors and to investigate the feasibility of employing a low-cost solution for tracking the flight paths of non-cooperative unmanned aerial vehicles operating within sensitive areas. Moreover, the choice to implement two acoustic sensors is motivated by the fact that the ReSpeaker Mic Array v2.0

Eventually, as operative drones, two DJI Mavic Dual Enterprise [56] have been chosen. In Table 7 its main specifications are reported.

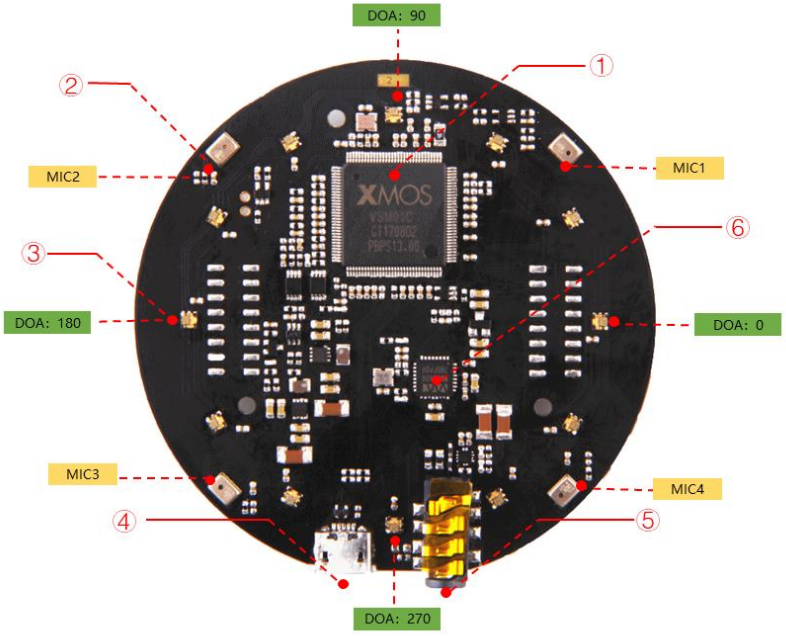

Figure 18. ReSpeaker Mic Array v2.0.

Table 6. SGR_RDR-216SR-1S10K-3D datasheet

Parameter	**Value**
Working System	Azimuth scanning + Elevation phase scanning
Working Mode	Pulse Doppler
Working Frequency	S-Band
Azimuth Coverage	360º
Elevation Coverage	≥ 40 º
Detection Speed	0.5 m/s – 30 m/s
Detection range	Up to 5 km for micro drones, but in general up to 8-10 km for civil drone
Rated power consumption	≤ 250 W
Installation	On a tower/pole of 6+ m of height
Dimension	782x882x434mm

Table 7. DJI MAVIC DUAL ENTERPRISE Specifications.

Specifications	**Value**
Takeoff Weight	899 g
Max Speed	72 kph
Max Service Ceiling	6000 m above sea level
Max Flight Time	31 minutes (no wind, at 25 kph)
Max Hovering Time	29 minutes (no wind)
Max Wind Speed Resistance	29-39 kph
Operating Temperature	-10ºC to 40ºC
GNSS	GPS+GLONASS

5.2.1. Phase 1 Implementation: Plugin Development and Scenario Configuration

Phase 1 focuses on the development and integration of surveillance sensor plugins within the BlueSky ATC Simulator environment. This phase encompasses the creation of specialized detection algorithms, the establishment of realistic operational scenarios, and the validation of individual sensor capabilities prior to fusion implementation.

All testing scenarios are simulated within the a rural area in the province of Caserta, Italy..

The experimental validation is structured around three primary test scenarios designed to systematically evaluate sensor performance across different operational conditions:

- Drones in radar coverage only: evaluate standalone radar performance and establish baseline detection metrics.
- Drones in acoustic sensor coverage only: assess acoustic sensor standalone performance and directional accuracy capabilities.
- Drones in overlapping coverage: evaluate multi-sensor detection capabilities and prepare foundation for sensor fusion implementation.

5.2.2. Trajectory Implementation

The development of the surveillance system simulation is grounded in the rigorous modeling of drone trajectories within the BlueSky ATC Simulator environment. The implementation of these trajectories constitutes the foundational framework for all subsequent sensor testing and validation, necessitating highly precise positional data and the faithful replication of realistic flight dynamics. For the sake of clarity, the two drones employed in the simulation will hereafter be referred to as Drone 1 and Drone 2, each of which is assigned a distinct trajectory path.

The initial trajectory implemented for Drone 1 within the simulation is derived from empirical flight data obtained during a prior experimental campaign conducted in the Castel Volturno area. This dataset provides real data, thereby ensuring that the simulation faithfully represents the actual behavioral patterns of drones within the targeted geographical context.

The imported trajectory comprises multiple geometric flight patterns specifically designed to evaluate various aspects of sensor detection and tracking capabilities:

- Linear Path Segments: straight-line flight patterns employed to assess continuous tracking accuracy and velocity estimation.
- Triangular Maneuvers: three-sided geometric patterns implemented to evaluate angular tracking performance and directional change responsiveness.
- Quadrilateral Patterns: four-sided flight paths facilitating comprehensive coverage assessment and the evaluation of complex maneuvering behavior.

Indeed, the original flight dataset was characterized by a high-resolution sampling rate with numerous trajectory points, resulting in substantial computational overhead during simulation processing. To address this challenge, a systematic point reduction procedure was applied, optimizing system performance while preserving trajectory fidelity.

The point reduction was accomplished through a systematic averaging and temporal downsampling approach implemented in Matlab™:

- Data Import and Preprocessing:
    - Telemetry data were imported from the .CSV file;
    - Time values were converted from datetime format to milliseconds, including appropriate time zone adjustments.
    - Altitude measurements were transformed from raw sensor readings into meters.
    - Coordinates were converted from geodetic format (latitude, longitude, altitude) to the local NED (North-East-Down) coordinate system, based on the WGS84 ellipsoid model.
- Windowed Averaging Algorithm:
    - Window Size: each averaging window consisted of 50 consecutive data points.
    - Averaging Process: Within each window, spatial coordinates (x, y, z) were averaged to produce a single representative point.
    - Temporal Downsampling: Corresponding time values were averaged within each window, thereby reducing the temporal resolution by a factor of 50.

As concerns mathematical implementation, indeed, the averaging and downsampling procedure can be formalized mathematically. Let $p_i = (x_i, y_i, z_i, t_i)$ denote the i-th trajectory point in a window of size N = 50. The representative point p_{rep} is computed as:

$$p_{rep} = \frac{1}{N}\sum_{i=1}^{N} p_i = (\frac{1}{N}\sum_{i=1}^{N} x_i, \frac{1}{N}\sum_{i=1}^{N} y_i, \frac{1}{N}\sum_{i=1}^{N} z_i, \frac{1}{N}\sum_{i=1}^{N} t_i) \quad (5)$$

This approach ensures that the reduced dataset preserves the essential geometric and temporal characteristics of the original trajectory while significantly decreasing computational load during simulation.

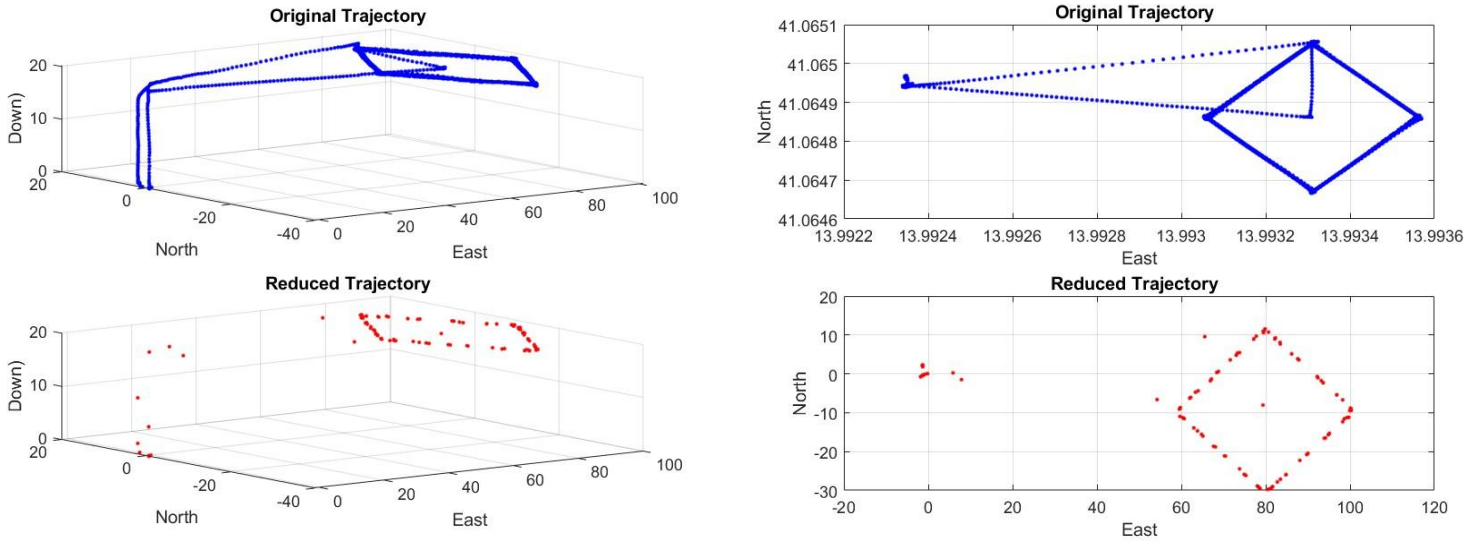

(a) (b)

Figure 19. Original and Reduced Trajectory imported for Drone 1: (a) 3D plot, (b) 2D plot.

A challenge emerged related to the visualization of the flight path within the BlueSky Air Traffic Control simulator. More specifically, due to the intrinsic resolution constraints of the simulation environment, the imported trajectory could not be adequately discerned in its reduced form. This limitation hindered the correct evaluation of the drone operational patterns and necessitated the introduction of an additional scaling step.

Hence, the algorithm performs a selective transformation exclusively on the horizontal plane (North-East coordinates) within the NED reference frame, while deliberately preserving the altitude profile. This choice ensures that the geometric amplification improves visual clarity without introducing distortions in the vertical dynamics of the drone's flight.

The scaling transformation is mathematically defined as:

- Centroid Calculation: the geometric center of the trajectory in NED coordinates is computed.
- Horizontal Scaling: North (X) and East (Y) coordinates are scaled by a user-defined factor relative to the trajectory centroid.

- Altitude Preservation: The Down (Z) coordinate remains unchanged to retain realistic flight altitude characteristics.

The scaling factor is configurable through the *scale_factor* parameter, which enables systematic exploration of different levels of magnification. More specifically, the transformation is applied according to the following formulation:

$$x_{scaled} = x_{center} + (x_{original} - x_{center}) \times \text{scale_factor}$$
$$y_{scaled} = y_{center} + (y_{original} - y_{center}) \times \text{scale_factor} \quad (6)$$
$$z_{scaled} = z_{original}$$

In Figure 20 is reported a comparison of the original trajectory and scaled one in 2D configuration, while figure depicts the scaled trajectory imported into Google Earth, thereby offering a realistic visualization of how the drone would operate within the real environment.

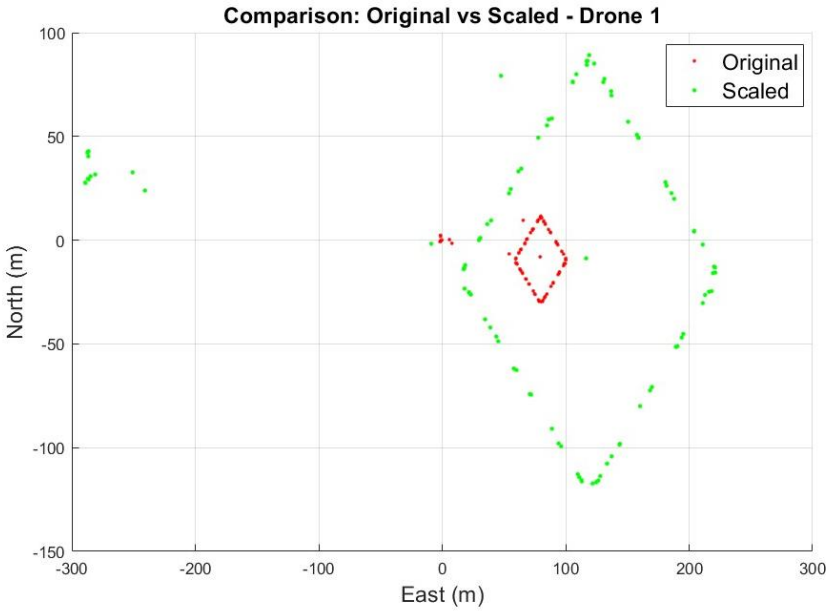

Figure 20. Comparison of the original and scaled trajectories for Drone 1 in a two-dimensional (2D) configuration.

Once obtained the trajectory, it must be imported in BlueSky. To do that, as first step the drone must be created in the scenario environment in the following way:

CRE Drone_1 Mavic2 41.0649476895666 13.9923597819262 0 94 14 (7)

The CRE command creates an aircraft and its configuration. Its input arguments are: *acid* (the assigned name), *type* (the aircraft model), *latitude*, *longitude*, *heading*, *altitude*, and *speed*. Note that altitude is expressed in feet (ft), while speed is expressed in knots (kts). Regarding the aircraft model, BlueSky provides a library containing all existing aircraft types, but new types can be added if necessary. To create an aircraft that is not already included in the library, a structure like the one shown in Figure 21 must be added to the *resourcers* folder.

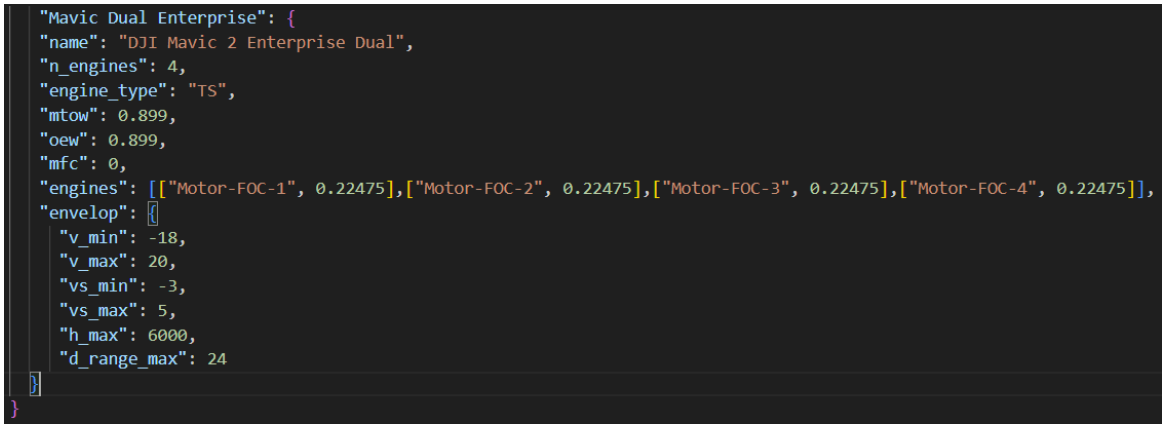

Figure 21. Example of aircraft creation in BlueSky ATC Simulator.

At this point, the command *ADDWPT* is applied to create the trajectory point by point.

Regarding the trajectory of Drone 2, a simple linear path has been assigned. This trajectory was generated manually in Python by defining waypoints directly with the *ADDWPT* command.

5.2.3. Radar Plugin Development

The integration of radar simulation capabilities within the BlueSky ATC Simulator requires precise coordination between detection algorithms and the underlying simulation framework. The plugin is designed to reflect realistic radar behavior, with particular attention to implementation strategy, mathematical modeling, and architectural coherence.

Radar operations are triggered by periodic simulation updates. During each cycle, the radar queries the traffic management subsystem to retrieve aircraft states, applies geometric and spatial filtering based on detection constraints, and communicates results to the display interface. This workflow ensures a consistent and responsive simulation of radar activity.

Temporal management is central to maintaining a balance between simulation fidelity and computational performance. The radar operates on configurable update intervals, allowing for a trade-off between detection resolution and system efficiencymirroring the operational constraints of real-world radar systems.

Initialization is handled by the *init_plugin()* function, which serves as the plugin's entry point. It instantiates the radar system and registers relevant commands within BlueSky's stack command system. Specifically, the following commands are defined:

- RADAR STATUS: shows radar status and detected targets.
- RADAR TOGGLE: toggle radar active state.
- DETECT: Verifies if a specific drone is detected by the radar and shows its information. As input, it requires the Aircraft ID.

The configuration dictionary returned by the initialization function defines the plugin integration parameters, while the registration of the update function establishes a callback mechanism that synchronizes radar processing with the simulation time progression.

The core logic resides within the Radar class, which extends BlueSky's Entity class to fully leverage the simulator's infrastructure. Its implementation follows object-oriented design principles, promoting modularity and maintainability while ensuring computational efficiency.

The radar simulation includes technical parameters that mirror operational radar systems. The positioning mechanism utilizes geographic coordinates with altitude data, enabling three-dimensional detection. Key parameters include maximum detection range and beamwidth, which define the spatial and angular coverage of

the radar. The system also incorporates rate limiting through a five-second update interval, striking a practical balance between responsiveness and processing load.

The airspace scanning algorithm constitutes the core computational component of the radar system, implementing a systematic methodology for target detection based on geometric and spatial analysis. At each simulation update, the algorithm iterates over all active traffic entities, computing their positions relative to the radar site and evaluating whether they fall within the predefined detection envelope.

To ensure both accuracy and computational efficiency, the algorithm utilizes BlueSky's optimized geographic utility functions (*geo.kwikdist()* and *geo.kwikqdrdist()*) which are based on spherical trigonometry and specifically tailored for aviation applications. These functions enable high-performance calculation of distances and bearings, which are essential for real-time simulation fidelity. In parallel, the vertical angle (elevation) between the radar and each target is computed through trigonometric methods, accounting for both horizontal displacement and altitude difference. This calculation is crucial to assess whether a target lies within the radar vertical coverage domain.

Detection feasibility is established through a three-dimensional validation process, which simultaneously considers range, azimuth, and elevation constraints. The range constraint ensures that only targets within the radar's maximum detection radius are considered. The azimuth constraint is trivially satisfied in this implementation due to the assumption of omnidirectional horizontal coverage, which is an architectural choice that reflects common surveillance radar configurations. The elevation constraint is modeled as a symmetric angular bound around the radar's horizontal axis, ensuring inclusion within the vertical beamwidth.

These constraints are combined using boolean logic consistent with physical radar detection principles: a target is deemed detectable only if all geometric conditions are simultaneously satisfied. This approach provides a realistic abstraction of radar line-of-sight mechanics, wherein spatial visibility governs the detection outcome.

Finally, all geometric calculations account for Earth curvature effects by relying on spherical geometry, ensuring consistency with established aeronautical computation standards while maintaining computational tractability within the simulation environment.

The distance calculation methodology employs great circle distance formulas, providing accurate range measurements regardless of geographic location. This approach ensures consistent detection performance across different simulation scenarios and geographic regions. The mathematical formulation for great circle distance is expressed as:

$$d = R \times \arccos(sin(\varphi_1) \times sin(\varphi_2) + cos(\varphi_1) \times cos(\varphi_2) \times cos(\Delta\lambda)) \tag{8}$$

where d represents the distance, R is the Earth's radius, φ_1 and φ_2 are the latitudes of the radar and target respectively, and $\Delta\lambda$ is the longitude difference.

The bearing calculation process determines the azimuth angle from radar to target using spherical trigonometry. The resulting bearing values provide directional information essential for target tracking and display purposes. The mathematical expression for bearing calculation follows:

$$\theta_{bearing} = arctam2(\sin(\Delta\lambda) \times \cos(\varphi_2), \cos(\varphi_1) \times \sin(\varphi_2) - \sin(\varphi_1) \times \cos(\varphi_2) \times \cos(\Delta\lambda)) \tag{9}$$

The elevation angle calculation represents a critical component of the three-dimensional detection capability. The implementation utilizes the arctangent function of the ratio between altitude difference and horizontal distance, providing accurate vertical angle measurements:

$$\theta_{elevation} = \arctan\left(\frac{h_{target} - h_{radar}}{d_{horizontal}}\right) \tag{10}$$

The mathematical formulation accounts for both positive and negative elevation angles, enabling detection of targets both above and below the radar altitude. This capability proves essential for comprehensive airspace surveillance in complex vertical traffic scenarios. In this work, $\theta_{\text{elevation}}$ denotes the elevation angle

(vertical), and φ denotes the zenith angle used in the coverage volume integral. Although φ is often used for latitude or elevation in some conventions, we adopt standard spherical coordinate notation for integration purposes.

Finally, the radar coverage volume represents a three-dimensional space defined by the intersection of range and angular constraints. The mathematical model creates a truncated cone extending from the radar position, with angular limits defining the detection envelope boundaries. The volume calculation can be expressed through the integral:

$$V_{coverage} = \iiint f(r,\theta,\varphi)\, r^2 \sin(\varphi)\, dr\, d\theta\, d\phi \tag{11}$$

With integration limits:

$$0 \le r \le R_{max}\ ,\ 0 \le \theta \le 2\pi,\ \left(\frac{\pi}{2} - \frac{\theta_{beam}}{2}\right) \le \varphi \le \left(\frac{\pi}{2} + \frac{\theta_{beam}}{2}\right) \tag{12}$$

where r denotes the slant range, θ the azimuthal angle, and φ the elevation angle.

The detection conditions can be expressed as Boolean functions:

$$R_{det}(r) = \begin{cases} 1, & r \le R_{max}, \\ 0, & r > R_{max}, \end{cases} \tag{13}$$

$$E_{det}(\varphi) = \begin{cases} 1, & \left|\varphi - \dfrac{\pi}{2}\right| \le \dfrac{\theta_{beam}}{2}, \\ 0, & \text{otherwise}, \end{cases} \tag{14}$$

$$A_{\det(\theta)} = 1 \quad \text{for} \quad 0 \le \theta \le 2\pi, \tag{15}$$

So that the overall detection condition is given by the logical product:

$$D(r,\theta,\varphi) = R_{det}(r) \cdot E_{det}(\varphi) \cdot A_{det}(\theta) \tag{16}$$

Outside the *Radar* class, another stack command named DETECTED is defined for debugging, so it manually triggers a radar scan and display results.

Finally, all the stack commands are summarized in Table 8.

Table 8. Command Interface Summary.

Command	Parameters	Function
RADAR_STATUS	None	Display current detection status
RADAR_TOGGLE	None	Toggle radar operational state
DETECT	Aircraft ID	Query specific target detection
DETECTED	None	Manual airspace scan esecution

As conclusion, the radar plugin demonstrates an effective integration of complex detection algorithms within the BlueSky simulation environment. The design combines realistic radar modeling with computational efficiency, making it suitable for both research and educational use. Its modular and extensible architecture allows for future enhancements without disrupting existing components, supporting iterative development. Geometric calculations rely on established aeronautical standards and optimized methods, ensuring accuracy and simulation consistency. Overall, the implementation provides a robust and flexible framework for simulating radar operations in air traffic scenarios.

5.2.4. Acoustic Sensor Plugin Implementation

The implementation of the acoustic sensor is grounded in the utilization of the ReSpeaker Mic Array v2.0, selected for its optimal balance between detection capability and urban deployment feasibility. The hardware characteristics of this platform, summarized in Table 9, directly influence both the plugin's detection algorithms and its operational parameters. The main aim of this plugin is to calculate the DOA.

Since two arrays are implemented in the current simulation, they will hereafter be referred to as Array 1 and Array 2 for the sake of simplicity. As for the radar plugin, the initialization is handled by the *init_plugin()* function in which the two arrays are created independently. Array 1 is positioned at coordinates 41.0645ºN, 13.9940ºE, in order to survey Drone 1, whereas Array 2 is strategically placed at 41,0632ºN, 13.9925ºE in order to cover the linear flight of Drone2. This dual positioning

strategy do not creates an overlap zone where both arrays can simultaneously detect the same target.

Table 9. ReSpeaker Mic Array v2.0 techincal specifications.

Parameter	**Value**	**Operational Impact**	**Urban Environment Consideration**
Digital Microphones	4	Circular array configuration	360º coverage capability
Inter-microphone spacing	45.7 mm	Spatial resolution for DOA	Optimal for drone frequencies
Sampling Frequency	16 kHz	Nyquist limit at 8kHz	Captures drone harmonic content
Array Tilt Angle	45º	Improved elevation accuracy	Optimized for urban flight altitudes
Realistic Detection Range	80 m	Drones as DJI Mavic 2 at optimal conditions	Complementary to radar coverage
Frequency Response	100 Hz – 8 kHz	Drone acoustic signature range	Urban noise filtering capability
Environmental Rating	IP54	Weather resistance	Urban deployment suitability

In the *init_plugin()* function, several stack commands are defined such as:

- ACOUSTIC_STATUS, which shows the status of both the array. More specifically, it provides position, status (active/not active), detections, tracking.
- ACOUSTIC_TOGGLE, that toggle the two arrays simultaneously.
- ACOUSTIC_TOGGLE_ARRAY1, which toggle Array 1 only.
- ACOUSTIC_TOGGLE_ARRAY2, which toggle Array 2 only.
- TRACK_DRONE_WAYPOINTS, which in input needs the drone name and then it can find the drone in the traffic and track it on both the arrays.
- STOP_TRACKING, Stop the tracking of the drones on both the array.
- TRAJECTORY_STATUS, reports trajectory and tracking of both the arrays.

After this, the *ReSpeakerAcousticSensor* class is created. The sensor implements a sophisticated acoustic modeling system that accurately simulates the behavior of a physical 4-microphone circular array. It should be remembered that the hardware specifications directly influence the detection algorithms, with the 45.7mm inter-microphone spacing providing optimal spatial resolution for drone acoustic signatures in the 150-300 Hz fundamental frequency range typical of consumer UAVs. The 16 kHz sampling rate ensures complete capture of harmonic content up to the 8 kHz Nyquist limit, while the 45° tilt angle of the physical array optimizes elevation angle estimation accuracy for urban flight altitudes typically between 10-100 meters.

As a preliminary step, the acoustic signature of a generic drone is simulated. Empirical studies and measurements indicate that commercial drones, such as the DJI Mavic 2, typically exhibit a fundamental blade rotation frequency in the range of 150 Hz to 300 Hz. Accordingly, a value is randomly selected within this interval to represent the base frequency of the drone's acoustic emission, reflecting the variability observed among consumer-grade UAVs.

To approximate the spectral characteristics of drone noise, a set of prominent harmonic components is introduced. Specifically, the simulation includes the 2nd, 3rd, 4th, 5th, 8th, and 10th harmonics of the fundamental frequency. These harmonics are chosen based on the observation that drone acoustic signatures are often rich in harmonic content due to periodic blade passage events and structural resonances.

The amplitude of the acoustic signal is modeled to attenuate with increasing distance from the sound source. A simplified inverse-distance model is employed:

$$A = \max\left(0.1, \frac{1.0}{\left(\frac{d}{10.0}\right)}\right) \tag{17}$$

where A denotes the amplitude, and d is the distance in meters from the sensor to the drone. A lower bound of 0.1 is enforced on the amplitude to ensure numerical stability and prevent unrealistically low values at large distances.

For each harmonic component, its corresponding frequency is computed by multiplying the base frequency by the harmonic order. These frequencies, along with their respective attenuated amplitudes, constitute the simulated spectral profile of the drone at the given distance.

To calculate the DOA, the core signal processing implements the Phase Transform (PHAT) weighting Cross Correlation Algorithm (GCC-PHAT) [57]. This algorithm aims to:

- Compute the cross-correlation between the two signals in the frequency domain, obtained via Fast Fourier Transform (FFT), because it is more efficient than direct time-domain correlation.
- Flatten the amplitude spectrum and give predominant weight to the phase (PHAT weighting), which carries more informative content about the delay and is less sensitive to amplitudes, echoes, and spectral coloration.
- Return to the time domain with the IFFT: the peak of the correlation indicates the TDOA.

The formulation can be summarized as:

$$R_{xy}^{PHAT}[n] = \mathcal{F}^{-1}\{\frac{X[k]Y^*[k]}{|X[k]Y^*[k]| + \epsilon} \tag{18}$$

where X, Y are the FFTs of the two signals, $*$ denotes the complex conjugate, and $\in$ prevents division by zero.

Direction of Arrival estimation combines time delay measurements from multiple microphone pairs to determine three-dimensional drone positions through sophisticated coordinate transformation processes. The GPS-to-cartesian conversion utilizes Earth-Centered Earth-Fixed (ECEF) transformations with subsequent conversion to local East-North-Up (ENU) coordinates, maintaining sub-meter accuracy throughout the transformation pipeline. The cartesian-to-spherical conversion provides range, azimuth, and elevation measurements with realistic error modeling that reflects actual acoustic sensor limitations in urban environments.

Finally, as primary outputs of the code are obtained:

- Estimated DOA parameters: Azimuth (± 10º error), elevation (± 15º error), range (±20% error).
- Quality metrics: Average correlation strength from cross-correlation analysis and dominant frequency components.
- Error measurements: Absolute differences between estimated and ground truth positions.

As a result of this implementation, the dual-array ReSpeaker plugin successfully establishes a software framework for acoustic sensing within the BlueSky ATM simulation environment, specifically targeting urban drone surveillance scenarios. The plugin incorporates a complete detection pipeline, in which a dual-array architecture enables both redundancy and cross-validation of acoustic measurements. A dedicated coordinate transformation module ensures high-precision conversions from GPS coordinates to spherical spatial references, thereby maintaining full compatibility with BlueSky internal position management system.

At the core of the detection algorithm lies a PHAT-weighted cross-correlation process, which operates on simulated four-microphone array signals. This implementation includes parameterized error modeling, yielding estimation uncertainties of ±10° for azimuth, ±15° for elevation, and ±20% for range. The system supports a maximum detection range of 50 meters and achieves an update frequency of 10 Hz (0.1-second intervals). A correlation strength threshold of 0.3 is employed to filter out unreliable detections, enhancing the robustness of the acoustic sensing process.

The command interface provides granular control over both independent and synchronized array operations. Additionally, the plugin integrates with BlueSky's waypoint-based trajectory tracking system to enable predictive detection prioritization, thereby improving computational efficiency. Environmental adaptability is achieved through dynamic adjustment of correlation thresholds in response to varying simulated urban noise profiles.

Despite these functional capabilities, the implementation exhibits several fundamental limitations. Most notably, it remains a purely simulated system without integration of physical acoustic signal processing. All detection processes are based on synthetically generated signals and parameterized error distributions, rather than on real-world acoustic input. As such, the framework's current form precludes empirical validation and limits its applicability to real-time, hardware-based urban surveillance operations.

5.2.5. Simulation Scenario

For the creation of the final scenario for simulation data collection, it was decided to separate the scenario in which only the radar plugin is active from the one in which only the acoustic sensor plugin is active. The two scenarios are created as *.scn* files (where the simulation area is defined) that is, the Bluesky simulator screen is set to cover the field test area, establishing the perimeter within which the two drones will operate.

In the scenario where only the radar is active (see Figure 22), once the simulator view has been positioned over the area of interest, the green, blue, and red circles are defined, corresponding respectively to the minimum detection zone, the recommended detection zone for drones, and the maximum detection range.

After this, the plugin is activated, the aircraft are created, and the trajectories are added. In Figure 23 a zoom on the generation of paths is reported. Using the stack commands DETECT DRONE 1 and DETECT DRONE 2, the function outputs are printed and saved into .txt files.

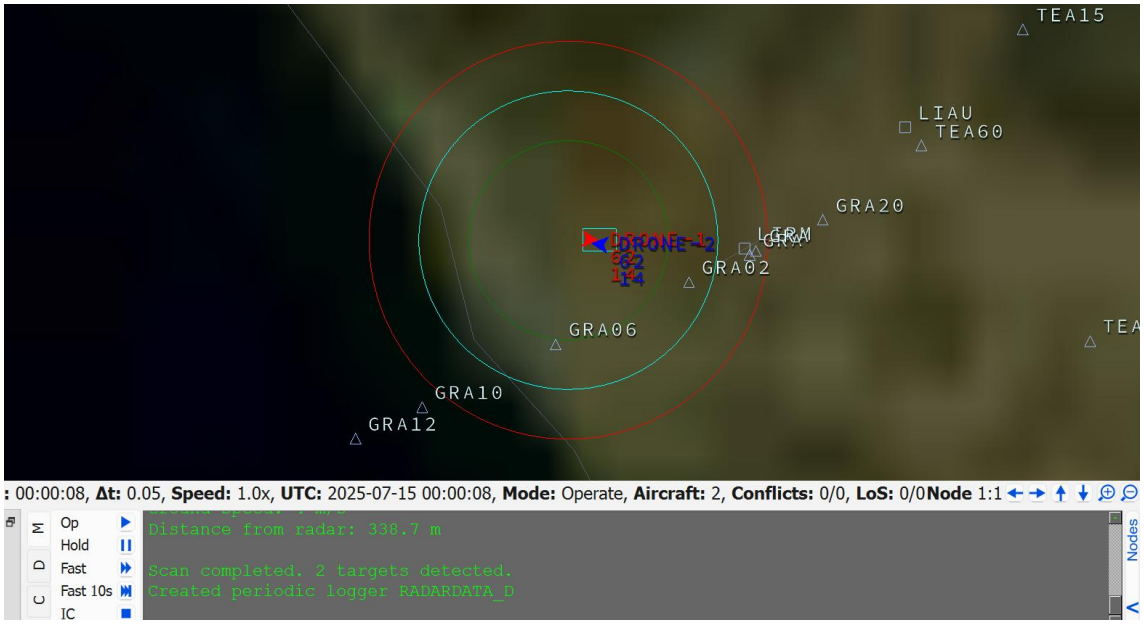

Figure 22. Radar-based simulation scenario in the Bluesky ATC environment.

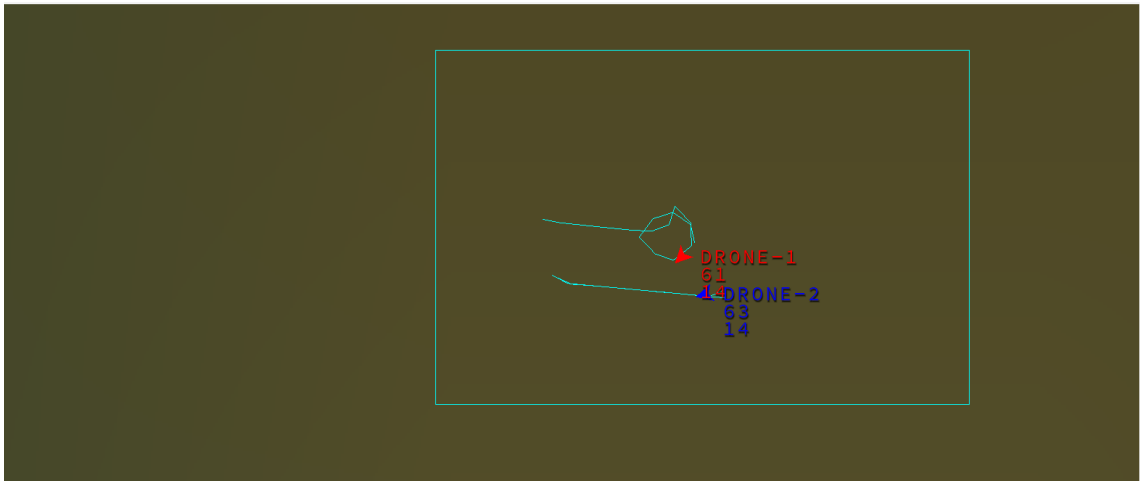

Figure 23. Zoom on the drone's trajectories in the radar-based simulation scenario in the Bluesky ATC environment.

In the scenario where only the acoustic sensors are active (see Figure 24), the procedure is very similar. First, the simulation area is created, and the acoustic sensors are placed within the defined perimeter. Once the sensors are positioned, they are activated, and the drones are generated along with their respective trajectories and the simulation data saved in .csv files.

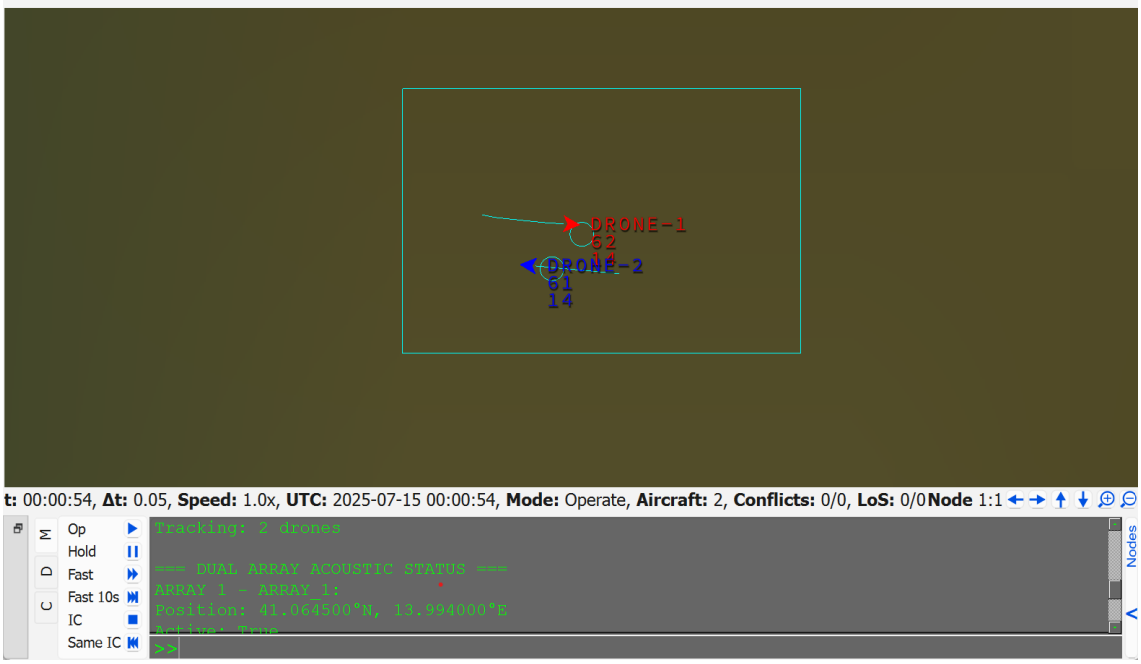

Figure 24. Acoustic sensor-based simulation scenario in the Bluesky ATC environment.

In conclusion, all the required data have been successfully generated and are ready for Phase Two. In future works, the datasets will be synchronized and processed with a Kalman filter to refine the measurements, suppress noise, and enhance the accuracy and reliability of the simulation results.

6. Experimental Validation: Real-world Drone Detection and RCS Characterization

As discussed in Chapter 2, which provided a detailed treatment of RCS properties and associated detection challenges, the reliable detection and tracking of UAVs has become increasingly critical, particularly in the context of airspace security and surveillance systems [58–60]. Small drones, however, typically generate weak radar signatures and often operate at low altitudes, thereby posing substantial challenges to conventional detection and tracking techniques [61]. Traditional detection schemes frequently assume that the RCS of a potential target can be modeled according to one of the classical Swerling models [44]. Although widely adopted, numerous studies have demonstrated that such models fail to provide an adequate description of UAV RCS characteristics [62–74]. This mismatch between actual UAV RCS behavior and the presumed statistical model can result in false alarms or missed detections, ultimately degrading overall radar system performance. Consequently, an accurate statistical characterization of drone RCS is a fundamental prerequisite for the design of dedicated signal processing strategies aimed at improving detection capabilities, reducing false alarm rates, and enhancing tracking accuracy.

Building upon the theoretical foundations established in the previous chapters, the present work extends the investigation through a comprehensive experimental analysis. Previous research carried out as part of this doctoral work has approached UAV radar characterization from a complementary perspective. Initially, simulation methodologies were developed using Matlab™ to explore and analyze the fundamental properties of UAV radar signatures under controlled conditions. Subsequently, large-scale simulations of multi-drone and multi-sensor surveillance scenarios in urban environments were performed to evaluate detection performance in more complex and realistic operational contexts.

In this context, the scope of the analysis is to investigate on the RCS statistical behavior of small drone using data collected during experiments performed with a Frequency-Modulated Continuous-Wave (FMCW) radar system both in X- and L-band [75,76]. The overarching objective is to perform a first-order statistical

characterization of RCS fluctuations for two representative UAV platforms: a consumer-grade drone (DJI Mavic 2 Dual Enterprise [56]) and a professional-grade drone (DJI Matrice 300 [77]). Data acquisition was carried out using the Multiband Interferometric and Polarimetric Synthetic Aperture Radar (MIPS) system [78–81], a ground-based polarimetric radar platform capable of operating in both X- and L-bands. While the X-band mode is limited to a single-polarization interferometric configuration, the L-band mode enables full polarimetric data acquisition, thereby allowing a more detailed investigation of polarization-dependent RCS variability.

The analysis is designed to examine how the statistical properties of UAV RCS are shaped by both radar operating frequency and polarization. In particular, for the L-band, all four polarization channels (VV, HH, VH, and HV) are analyzed independently. The ECDF of the measured RCS values is employed to evaluate the statistical behavior of each UAV. Complementary statistical metrics, including standard deviation, interquartile range, full range, and box-and-whisker plots, are further used to quantify RCS dispersion across different measurement conditions. To determine the most appropriate theoretical model, a quantitative comparison is performed using the CVM distance [44]. Finally, a comparative analysis between X- and L-band results is presented, with the aim of identifying key differences and elucidating the respective roles of radar frequency and polarization in shaping UAV radar signatures.

The results of this investigation confirm that distinct UAV platforms exhibit markedly different RCS fluctuation behaviors, each of which aligns with different statistical models depending on the UAV structural and geometrical characteristics. Furthermore, for a given UAV, the best-fitting RCS distribution changes not only between the X- and L-band, but, in the case of the L-band, also across polarization channels. These findings substantiate the frequency- and polarization-dependent nature of UAV radar signatures and highlight the necessity of statistically grounded modeling approaches for accurate UAV detection and classification.

6.1. Overview

The scientific literature has extensively investigated the influence of polarization and aspect angle on the scattering properties of unmanned aerial vehicles (UAVs) [62–74]. Nevertheless, the majority of these studies have relied on measurements acquired in controlled or semi-controlled environments, often overlooking dynamic factors that become critical in realistic operational scenarios, such as UAV flight dynamics and rotor blade motion [62–74]. In operational conditions, these elements introduce non-negligible contributions to the radar signature and must therefore be incorporated into any rigorous and comprehensive analysis [82–91]

6.1.1. Factors Influencing Radar Cross Section

The RCS of UAVs under realistic conditions is shaped by a range of interdependent factors that distinguish these platforms from conventional aircraft and ground vehicles, as outlined in Chapter 2. Specifically, UAV radar signatures are primarily governed by their physical configuration, which is typically characterized by lightweight composite materials, complex geometrical structures, and prominent rotor assemblies. Small UAVs frequently operate within the Rayleigh or resonance scattering regimes, where the RCS exhibits a pronounced frequency dependence, whereas larger UAVs may approach optical scattering behavior at higher frequencies.

A particularly important consideration is that, unlike static measurements, operational UAV flights introduce temporal variability into radar signatures due to several dynamic phenomena:

- Rotor Blade Modulation: The rotating blades create time- varying scattering contributions that manifest as amplitude modulation of the radar return and characteristic micro-Doppler signatures. These effects are particularly pronounced at frequencies where blade dimensions approach resonant lengths.
- Attitude Variations: Continuous changes in UAV orientation during flight result in aspect angle-dependent RCS fluctuations. The angular sensitivity

of UAV radar signatures means that small attitude changes can produce significant variations in measured RCS.

- Flight Dynamics: Accelerations, velocity changes, and maneuvering introduce additional Doppler effects and can influence the effective aspect angle presentation to the radar over time.

Moreover, frequency plays a pivotal role in shaping the observable radar characteristics. Lower frequency bands (e.g., L-band) generally exhibit reduced angular sensitivity but are often associated with lower absolute RCS levels. Conversely, higher frequency bands (e.g., X-band) tend to yield stronger radar returns, albeit with greater angular dependence and heightened sensitivity to fine structural detail stronger returns but with increased angular dependence and sensitivity to structural details.

6.1.2. Radar Cross Section Estimation Procedure

The procedure for estimating the RCS of in-flight UAVs is based on the radar equation for a monostatic radar system. The power of the signal received by the radar, reflected from a target at range R with a specific RCS σ, is expressed as [44]:

$$P_r = \frac{P_t G^2 \sigma \lambda^2}{(4\pi)^3 R^4 L} \tag{19}$$

Where P_t is the transmitted power, G is the antenna gain (assumed equal for transmission and reception), λ is the wavelength corresponding to the carrier frequency, and L accounts for loss terms. Solving this equation for σ yields the RCS of the target:

$$\sigma = \frac{P_r R^4 (4\pi)^3 L}{P_t G^2 \lambda^2} \tag{20}$$

Assuming the antennas gains and system losses remain constant over N consecutive pulses, the RCS for each slow-time index can be estimated as:

$$\hat{\sigma}_n = \hat{P}_{r,n} \hat{R}_n^4 \kappa \qquad n = 1, \dots, N \tag{21}$$

Where $\kappa = \frac{[(4\pi)^3 L]}{[P_t G^2 \lambda^2]}$ is a constant whereas $\hat{P}_{r,n}$ and $\hat{R}_n, n = 1, \dots, N$ are the estimates of the received power and range of the target for each pulse. To facilitate the study of RCS fluctuation without computing κ, a normalized RCS vector of observations is considered:

$$\bar{\sigma} = \frac{\hat{\sigma}}{\hat{\sigma}_{av}} \tag{22}$$

Where $\hat{\sigma} = [\hat{\sigma}_1, \hat{\sigma}_2, \dots, \hat{\sigma}_N]$, and the parameter $\hat{\sigma}_{av}$ is the sample mean of $\hat{\sigma}$.

6.1.3. FMCW Radar Systems

FMCW radar technology has emerged as particularly suitable for UAV detection applications due to its inherent advantages in detecting small, low-velocity targets in cluttered environments.

FMCW systems transmit a frequency-modulated signal and process the frequency difference (beat frequency or instantaneous signal) between transmitted and received signals to extract target range and velocity information simultaneously. For UAV detection, FMCW offers several key advantages such as high range resolution, simultaneous range and velocity measurement, low peak power requirements, excellent clutter rejection.

The fundamental principle of an FMCW radar is based on its transmitted signal, known as chirp, that is a sinusoidal signal whose frequency increases linearly with time [92]. Each chirp is precisely characterized by a start frequency (f_c), a specific bandwidth (B) it sweeps across, and a duration (T_c). For example, a chirp might sweep a bandwidth of 4 GHz in 40 microseconds, defining a slope (S) of 100 MHz/µs.

The Operational process in a monostatic FMCW radar unfolds in several key steps:

- Chirp Generation and Transmission: A synthesizer generates the chirp, which is then transmitted into the environment by the transmit (TX) antenna.

- Reflection and reception: When this transmitted chirp encounters an object, a portion of its energy is reflected. The reflected chirp, now delayed in time due to the round-trip travel, is received by the receive (RX) antenna.
- Signal Mixing and IF Signal Generation: The crucial step for range estimation involves "mixing" (multiplying) the received (RX) signal with a portion of the currently transmitted (TX) signal. This process generates an "Intermediate Frequency" (IF) signal. For a single stationary object, this IF signal is a constant frequency tone. The frequency of this tone is directly proportional to the time delay (τ) between the transmitted and received chirps, which in turn is proportional to the object's distance (d). Specifically, the IF frequency is given by the formula $S\tau = S(2d/c)$, where S is the chirp slope, d is the object's distance, and c is the speed of light.
- Digitization: The analog IF signal is then converted into digital data by an Analog-to-Digital Converter (ADC). The sampling rate (F_s) of this ADC is critical, as it directly limits the maximum range (d_{max}) the radar can effectively detect. This maximum range can be calculated as $d_{max} = F_s c \,/\, 2S$.
- Range Estimation via FFT: To determine the precise range of objects, a FFT is performed on the digitized ADC data. The FFT transforms the time-domain IF signal into the frequency domain, where distinct peaks correspond to the frequencies of the constant tones present in the IF signal. Each detected frequency peak directly correlates to an object range.

When multiple objects are present in the radar field of view, the IF signal will contain multiple constant frequency tones, each corresponding to a different object's range. Performing an FFT on this complex IF signal will thus reveal multiple peaks, enabling the radar to resolve and measure the ranges of these distinct objects. The ability of the radar to differentiate between two closely spaced objects is known as range resolution.

Beyond range, FMCW radars are also capable of estimating an object velocity. This is typically achieved by transmitting multiple chirps within a defined "frame" and applying a more complex 2D-FFT processing technique to the collected data.

The combination of these range and velocity measurements allows for the creation of a range-velocity plot of the observed scene. FMCW radars are widely used in various applications, including altimeters, proximity fuses, and advanced automotive collision avoidance systems. Their use of frequency modulation effectively decouples energy and resolution, providing significant advantages over simple pulsed waveforms

6.1.4. Experimental Setup and Methodology

The entire experiment was conducted in the drone flying zone located in a rural area, mentioned in the previous chapter. In Figure 25 is illustrated an example the flight area for the drones and location of the surveillance system used.

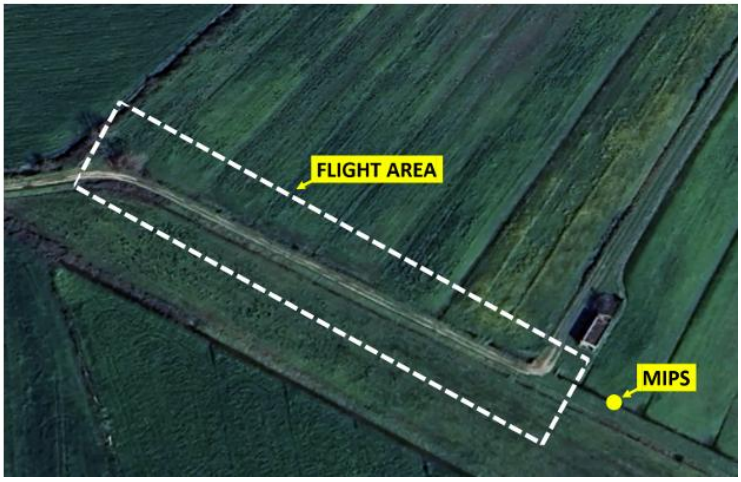

Figure 25. Example on Google Earth of the flight area for drones and location of the surveillance system (MIPS radar system).

The radar system used to collect data is the MIPS [79–81], which is single-pass interferometric airborne FMCW Synthetic Aperture Radar (SAR) prototype realizes by the Electromagnetic Sensing of the Environment (IREA) of the National Italian Research Council (CNR) in agreement with "Elettra Microwave". It basically exploits FMCW technology, which allows to work in a high-resolution mode, and is capable of operating in two distinct frequency bands:

- X-band: Functions as a single-pass interferometric radar. In this mode, the system uses three X-band commercial off-the-shelf VV polarized microstrip antennas (one for transmission (TX) and two for reception (RX1 and RX2).

The transmitting antenna is placed at the center, with a baseline of 1.75 m connecting the two receiving antennas. These antennas provide a maximum gain of 24.7 dB and a half-power beamwidth of approximately 20º in elevation and 7.5º.

- L-band: Operates as a fully polarimetric system. For L-band, the system is configured with four L-band antennas, comprising two TX and two RX. These antennas include two vertically and two horizontally polarized elements. They share identical gains but exhibit a wider half-power beamwidth of approximately 59º in elevation and 56 º in azimuth.

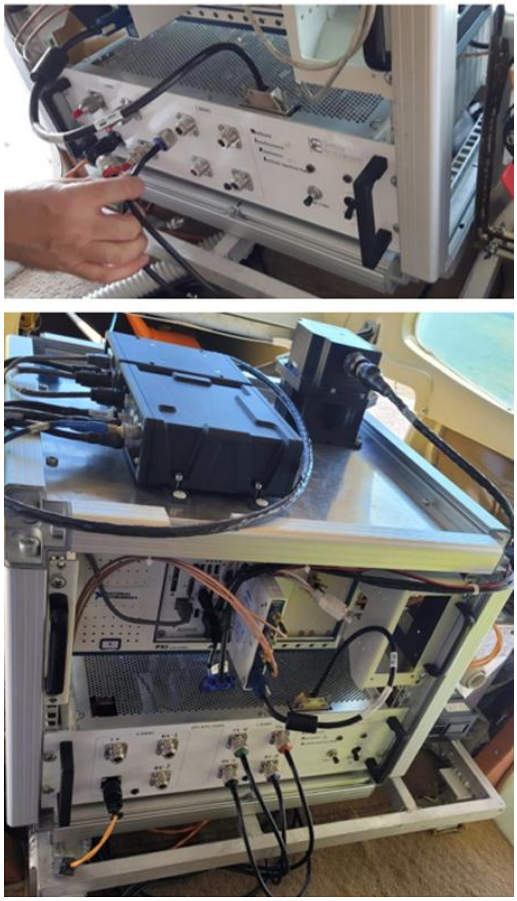

Figure 26. MIPS system's rack.

For all conducted measurements, the MIPS system was operated as a ground-based radar platform. Due to its compact size (approx. 50 cm x 50 cm x 65 cm) and low weight (approx. 35 kg), the transmit and receive subsystem was mounted inside a car, with both the transmit and receive antennas installed on the roof at approximately 1.80 m above the ground as demonstrated in Figure 26 and Figure

27. The antennas were consistently oriented at approximately -50º in azimuth with respect to true North and 73 º in elevation relative to the ground level in both X- and L- band trials. The main parameters of the MIPS radar system used in the experiment are summarized in the Table 10.

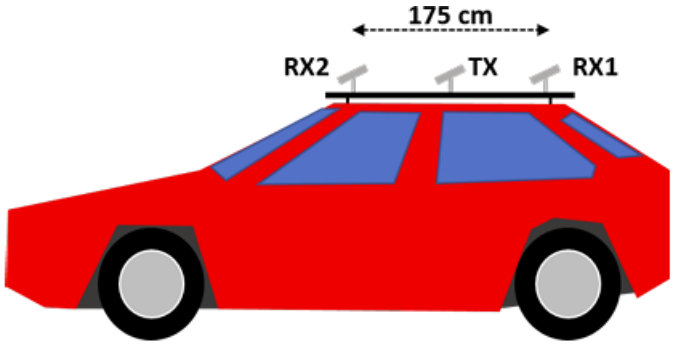

(a)

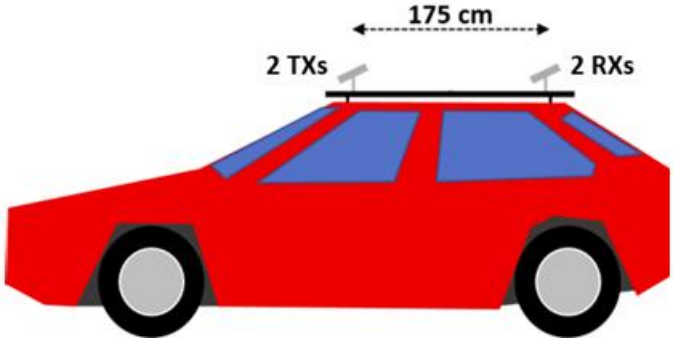

(b)

Figure 27. Example of the geometric configuration of the transmit and receive antennas used in the measurement campaign. (a) X-band interferometric configuration. (b) L-band fully polarimetric.

Table 10. Main features of MIPS radar system both in L- and X-band.

Parameter	L-band	X-band
Carrier frequency [Ghz]	1.35	9.55
Chirp bandwidth [Mhz]	200	200
Sampling rate [Mhz]	25	25
Pulse Repetition Frequency (PRF) [Hz]	600	1200
Polarization	Quad-pol	VV
Range Resolution [m]	3	3
Number of TX antennas	2	1
Number of RX antennas	2	2
Radar rack size [cm]	50 × 50 × 65	50 × 50 × 65
Radar weight [kg]	35	35
Antenna size [cm]	20 × 40 × 4	24 × 12 × 1.5
Antenna weight [kg]	1.5	0.5

The experiments involved the simultaneous flight of two different Commercial-Off-The-Shelf (COTS) drones: (i) DJI Mavic 2 Enterprise Dual [56], (ii) DJI Matrice 300 [77]. These drones , shown in Figure 28 ,were chosen to represent platforms used for professional operations in the U-Space environment, based on their different sizes and Maximum Take-Off Mass (MTOM) values. The main characteristics of the drones are compared in Table 11.

Figure 28. DJI Matrice 300 (left), DJI Mavic 2 Enterprise Dual (right).

Table 11. Comparison between main characteristics of DJI Matrice 300 and DJI Mavi 2 Dual Enterprise

Characteristics	**DJI Matrice 300**	**DJI Mavic 2 Dual Enterprise**
Dimensions (with propellers) [cm]	81 × 67 × 43	32.2 × 24.2 × 8.4
MTOW [kg]	9	1.1
Maximum payload weight [kg]	2.7	No payload
Flight endurance [min]	55	31
Satellite navigation system	GPS+GLONASS+BeiDou+ Galileo	GPS+GLONASS
Stationary flight accuracy [m]	±0.5V ±1.5H	±0.5V ±1.5H
Propeller Diameter [mm]	533	220

During the in-flight trials, both drones flew up to a maximum range of 200 m and a maximum height of 120 m. They followed an almost piecewise linear flight path, moving away from and toward the radar. The flight campaigns were conducted in

automatic flight mode, with planned waypoints defined by 3D coordinates (latitude, longitude, and height) using the drone manufacturer mission management systems. The flight trajectories included phases of moving away from the radar; segments of stationary flight (hovering), and movements towards the sensor, repeating cyclically. Figure 29 shows the drones nominal range based on telemetry and radar position during MIPS operation in the X-band (a) and L-band (b). These dynamic and realistic conditions, including intervals where both drones were at similar distances, were designed to analyze behavior under potentially critical radar detection and resolution scenarios.

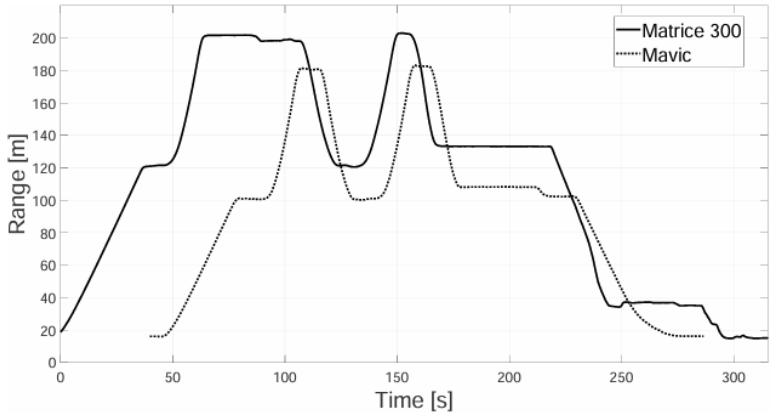

(a)

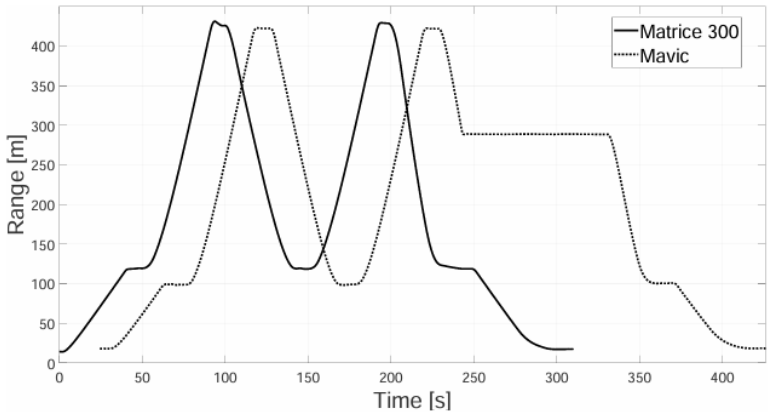

(b)

Figure 29. Nominal drone range, determined from telemetry data and the radar's precise geographic coordinates, during MIPS system operation in the X-band (a) and L-band (b)

After describing the experimental setup and the procedure used to estimate the drone's RCS, we now turn to the methodology of the analyses performed and the discussion of the corresponding results.

The actual range of the drones and their contribution to the received signal's power are estimated from the scene's range profile. For an FMCW system like MIPS, the range profile for each slow-time index is obtained by taking the modulus of the Discrete Fourier Transform (DFT) of the beat signal (also known as the frequency difference signal) samples [93]. Multiple targets in the scene result in multiple peaks in the range profile, allowing their ranges to be estimated from the peak positions, and their power contributions from the square of the identified peak values.

Moreover, since the MIPS system has a range resolution of 3 m in both frequency bands, the Matrice 300 appears as an extended target in the range domain, occupying multiple adjacent range bins. To treat both drones as point-like targets, the range profiles are computed by applying the modulus of the DFT to a shortened portion of the beat signal. This effectively lowers the range resolution, allowing the Matrice 300 to be considered as a point-like target for the analysis.

6.1.5. Results and Discussion

The statistical model associated with these RCS fluctuations is also studied by evaluating the ECDF from this normalized observation vector. The comparison of the ECDFs of the two in-flight UAV allows us to investigate the potential relationship between drone type and the statistical models describing RCS fluctuations for each frequency band and polarization, as well as to assess whether these models are affected by the radar operating parameters.

6.1.6. X- Band Results

Data for the X-band analysis are collected over a span of 296 s. The range-time maps (in dB), obtained using the first and second halves of the beat signal samples for each slow-time index, are shown in Figure and Figure respectively (hereafter referred to as Segment 1 and Segment 2).

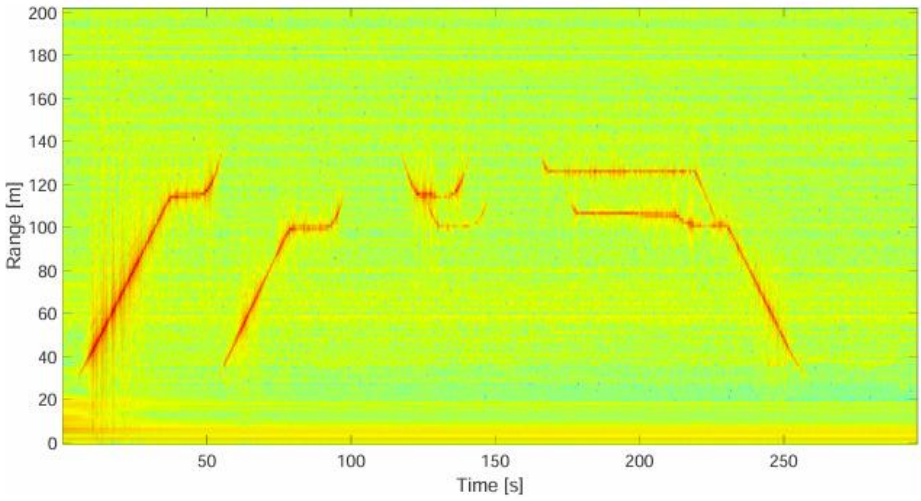

(a)

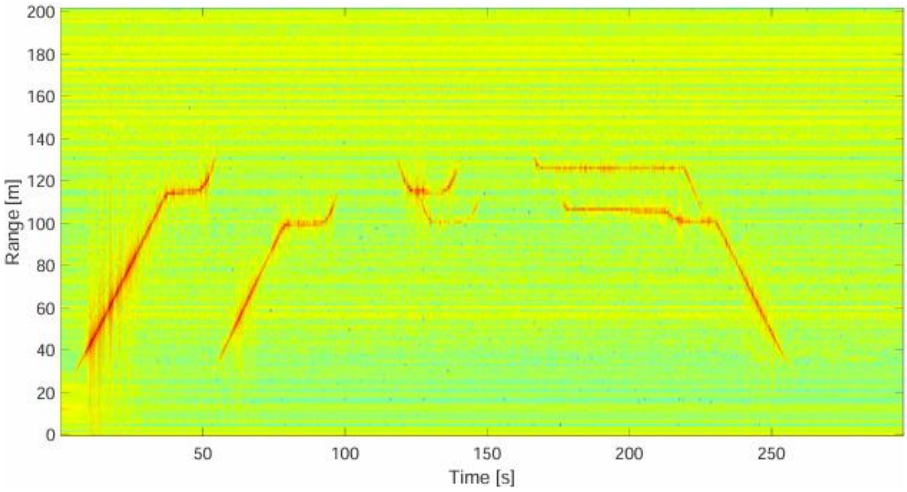

(b)

Figure 30. Range-time maps (in dB) obtained from X-band data using the first (a) and second (b) halves of the beat signal samples for each slow-time index.

However, drones were not consistently visible in the radar data during certain acquisition intervals, which corresponded to times when the UAVs flew outside the main beam of the radar system. This phenomenon results more pronounced in the X-band due to the narrower beamwidth of the antennas compared to the L-band experiments.

The ECDFs of the normalized RCS for both the Matrice 300 and the Mavic are illustrated in Figure 31. The RCS data are extracted from two distinct time intervals,

referred to as Area 1 and Area 2. Area 1 corresponded to [29.5; 35.5] s for the Matrice 300 and [62;68] s for the Mavic, while Area 2 encompassed the prudence of both drones during [186;196] s.

Key observations from the X-band ECDF analysis include:

- For a given area and drone, the ECDFs derived from the two segments of the beat signal (Segment 1 and Segment 2) were almost identical.
- For a given drone, ECDFs obtained from data collected across the two areas (Area 1 and Area 2) showed generally good agreement, despite some deviations.
- Regardless of the area and segment, the ECDFs corresponding to the two drones are notably different. This highlights that different drones follow distinct models to describe their RCS fluctuations, a crucial finding for developing tailored adaptive detectors.

The latter observation reinforces the concept that the structural characteristics of the UAVs, as size, material composition, and shape, have a strong impact on the determination of the RCS fluctuation behavior.

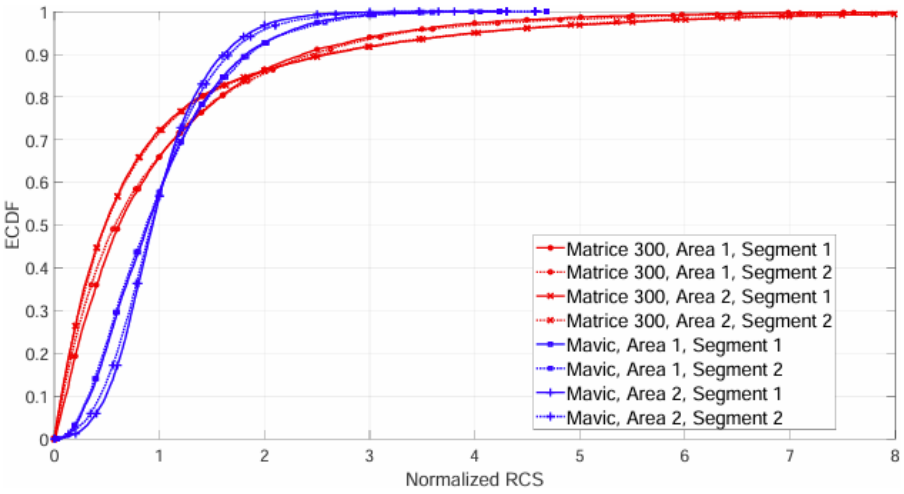

Figure 31. Behavior of the ECDFs of both the DJI Matrice 300 (red curves) and DJI Mavic 2 Dual Enterprise (blue curves) using the RCS observations in the X-band.

To provide a quantitative assessment of RCS variability, statistical dispersion indices such as standard deviation (SD), interquartile range (IQR), and full range were calculated. The Matrice 300 consistently exhibited much stronger variability

in its RCS fluctuations compared to the Mavic 2 Dual Enterprise, as evidenced by higher values for these indices across all area and segments as shown in Table 12.

Table 12. Dispersion indices of normalized RCS for both drones across different areas and segments.

Area-Segment	Drone	SD	IQR	Range
Area 1- Segment 1	Matrice 300	1.1270	1.0815	12.940
	Mavic	0.6078	0.7788	4.2166
Area 1- Segment 2	Matrice 300	1.2044	1.1063	13.703
	Mavic	0.6280	0.7999	4.6501
Area 2- Segment 1	Matrice 300	1.4751	0.9247	17.345
	Mavic	0.4557	0.5453	4.2994
Area 2- Segment 2	Matrice 300	1.4427	0.9518	18.967
	Mavic	0.5021	0.6074	4.5786

Hence, Matrice 300 has a more complex RCS behavior probably due to the structural characteristics and geometry of the drone. This trend is also clear in the box-and-whisker plots shown in Figure 32. The Matrice 300 displayed significantly wider boxes and longer whisker across all area-segment case studies, indicating a deeper RCS fluctuation. The dense distribution of outliers (shown as red crosses) further supports the occurrence of strong radar returns, likely due to its structural complexity. In contrast, the Mavic showed more compact boxes, shorter whiskers, and fewer outliers, reflecting a more stable RCS behavior.

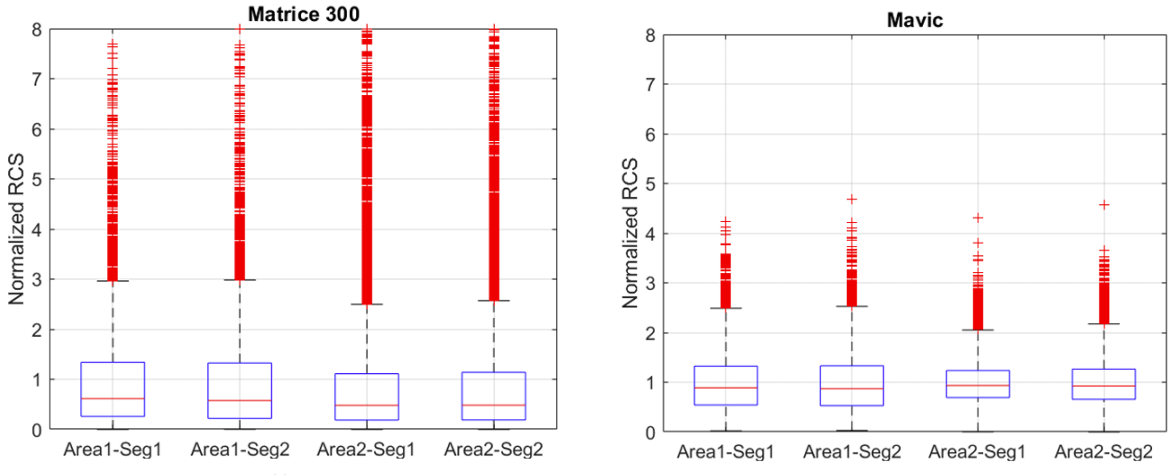

(a) (b)

Figure 32. Box-and-whisker plots from X-band data of the Matrice 300 (a) and Mavic (b) drones. Each box shows the statistical distribution of normalized RCS values for different areas and segments.

6.1.7. L-Band Results

The analysis conducted for the L-band are carried out using the same methodological approach as for the X-band, with some notable differences. First, the data are collected over a time span of 314 s. The broader beamwidth of the L-band antennas results in an extended radar footprint, enhancing spatial coverage but simultaneously increasing clutter, as highlighted by the comparison with the X-band maps in Figure 30. To mitigate the interference affecting the initial portion of the acquisition, the analysis was restricted to the second half of the beat signal. The corresponding range–time maps (in dB) for the four polarimetric channels (VV, HH, VH, HV) are shown in Figure 33.

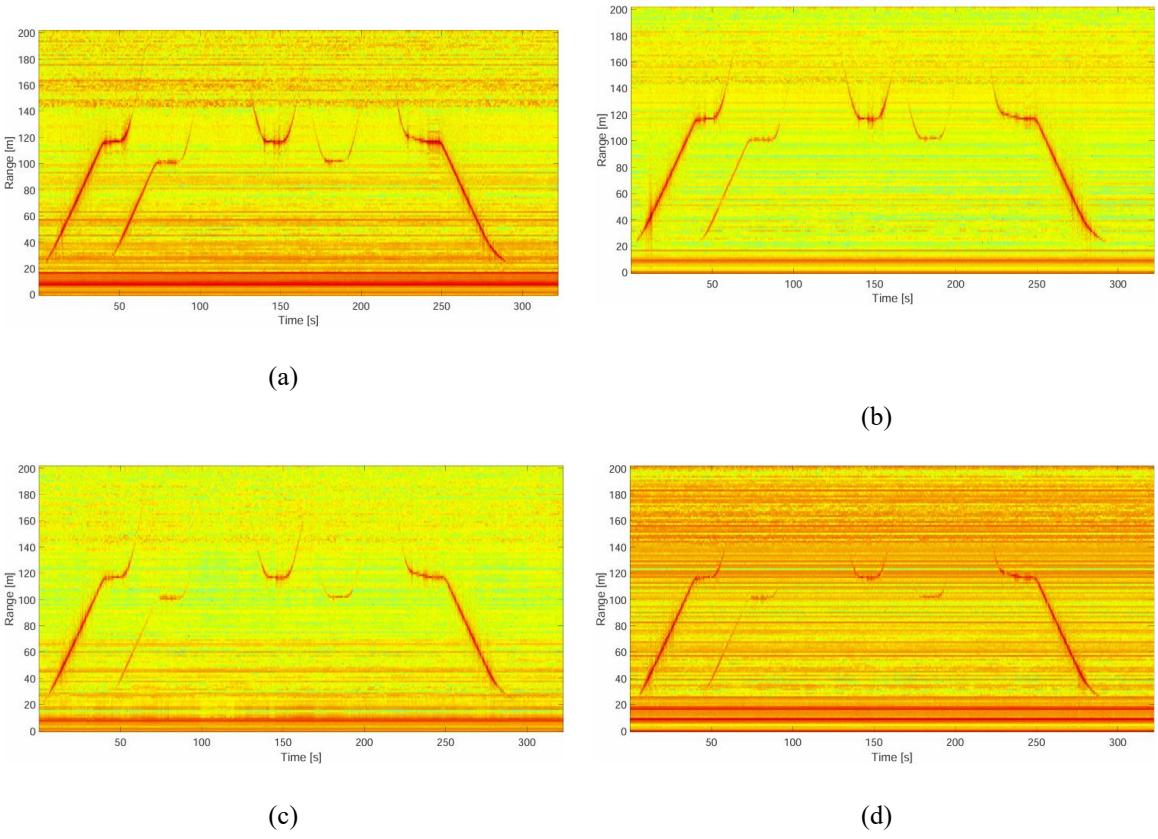

Figure 33. Range-time maps (in dB) derived from L-band data using the second half of the beat signal samples for each slow-time index, shown for the four polarization configurations: (a) VV, (b) HH, (c) VH, and (d) HV.

For the L-band experiments, the ECDFs shown in Figure 11 were computed using RCS data estimated over the time intervals [30, 40] s for the Matrice 300 and [68.5, 74] s for the Mavic.

Analysis of the resulting curves leads to the following observations:

- For each UAV, the ECDFs corresponding to the co-polarized channels (VV and HH) are similar to each other, as are those of the cross-polarized channels (VH and HV).
- For both drones, the ECDFs of the co-polarized channels (VV and HH) display a steeper transition from 0 to 1 compared to those of the cross-polarized channels (VH and HV), suggesting that the latter exhibit greater variability in RCS.

- Across all polarization configurations, the ECDFs differ significantly between the two drones, indicating that each UAV has a unique RCS fluctuation pattern.

These findings emphasize the importance of polarization diversity in radar-based drone detection and classification. In particular, evaluating the RCS under different polarization configurations can enhance the discriminatory capability of surveillance and classification radar systems.

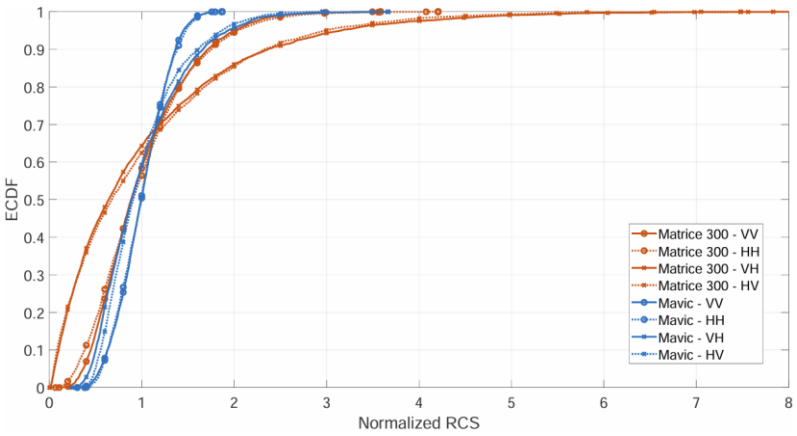

Figure 34. Behavior of the ECDFs of both the DJI Matrice 300 (red curves) and DJI Mavic 2 Dual Enterprise (blue curves) using the RCS observations in the L-band.

To further assess the variability of the normalized RCS under different polarization conditions, as was done for the X-band, several statistical dispersion metrics were computed. Table 13 reports the results for both UAVs across the four polarization channels.

Table 13.Dispersion indices of normalized RCS for each drone and polarization

Polarization	Drone	SD	IQR	Range
VV	Matrice 300	0.5104	0.6686	3.4752
	Mavic	0.2762	0.4082	1.5662
HH	Matrice 300	0.5509	07233	4.1399
	Mavic	0.2794	0.4121	1.4838
VH	Matrice 300	1.0639	1.1545	8.6310
	Mavic	0.4773	0.6286	3.4164
HV	Matrice 300	1.0073	1.2110	7.4730
	Mavic	0.4248	0.5295	2.6580

Overall, the Matrice 300 exhibits larger and more variable RCS fluctuations across all polarization configurations, with particularly pronounced variability in the cross-polarized channels (VH and HV). This trend is also visually evident in the box-and-whisker plots in Figure 35, where the Matrice 300 displays noticeably wider boxes and longer whiskers across all polarizations, especially in VH and HV, along with a significantly higher number of outliers.

In contrast, the Mavic presents more compact and uniform box plots across all polarization channels, with fewer outliers and a tighter distribution, indicating a more stable RCS response.

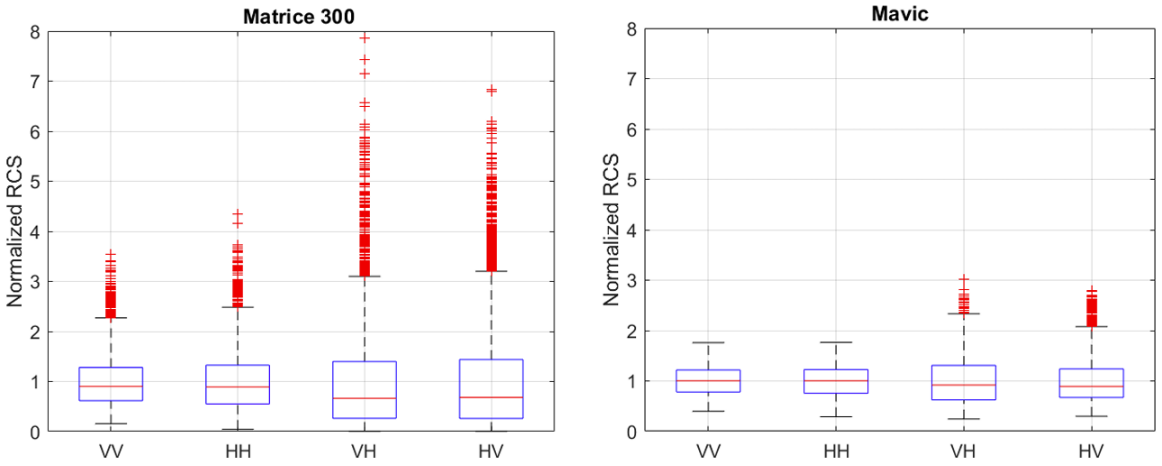

Figure 35. Box-and-whisker plots from L-band data of the Matrice 300 (a) and Mavic (b) drones. Each box shows the statistical distribution of normalized RCS values for polarization.

6.1.8. Cramér-von Mises Distance Analysis

Having established that the ECDFs exhibit notable differences across UAV platforms, frequency bands, and polarization configurations, the subsequent step involves identifying the theoretical statistical model that best describes the observed normalized RCS values. This evaluation is carried out by computing the CVM distance between the empirical ECDFs and a set of candidate theoretical distributions.

The model that yields the smallest CVM distance is considered the most appropriate for accurately representing the RCS fluctuations of each UAV. To perform this comparison, the parameters of each candidate distribution are estimated directly from the data using the maximum likelihood estimation (MLE) method. This technique identifies the parameter set that maximizes the likelihood of observing the measured RCS values under the assumption that the data follows the distribution in question.

Once the optimal parameters are obtained, the corresponding CDF is derived and compared to the empirical CDF using the CVM distance. This distance is a measure of the discrepancy between two CDFs and is particularly suitable for assessing the goodness-of-fit in a distributional sense.

Formally, for a set of H independent and identically distributed observations $\{X_1, \dots, X_H\}$ of a random variable X, the CVM distance is computed as follows:

$$d_{CV} = \sqrt{\frac{1}{12H} + \sum_{h=1}^{H} \left| F_X(X_h) - \frac{2h-1}{2H} \right|^2} \tag{23}$$

where $f_{X(\cdot)}$ is the presumed CDF and $X_{(h)}$ is the h-th order statistic from the set of observations. In particular, the CVM distance has been computed considering the Exponential (E), Gamma (G), Log-Normal (LN), Weibull (W), and Generalized Pareto (GP) distributions as candidate models. The probability density functions (PDFs) corresponding to each of these distributions are provided below:

$$f(x) = \lambda e^{-\lambda x} \qquad \lambda > 0, \; x \geq 0 \qquad \text{(E)} \tag{24}$$

$$f(x) = \frac{x^{k-1} e^{-x/\theta}}{\theta^k \Gamma(k)} \qquad k > 0, \theta > 0, \; x \geq 0 \qquad \text{(G)}$$

$$f(x) = \frac{1}{x\sigma\sqrt{2\pi}} e^{-\frac{(\ln x - \mu)^2}{2\sigma^2}} \qquad \mu \in \mathbb{R}, \sigma > 0, \; x > 0 \qquad \text{(LN)}$$

$$f(x) = \frac{k}{\lambda}\left(\frac{x}{\lambda}\right)^{k-1} e^{-\left(\frac{x}{\lambda}\right)^k} \qquad \lambda > 0, k > 0, \; x \geq 0, \qquad \text{(W)}$$

$$f(x) = \frac{1}{\sigma}\left(1 + k\frac{x}{\sigma}\right)^{-\frac{1}{k}-1} \qquad k \in \mathbb{R} - \{0\}, \sigma > 0 \; x > 0, (k > 0), \; 0 < x < \frac{\sigma}{|k|} (k < 0) \qquad \text{(GP)}$$

where $\Gamma(\cdot)$ is the Gamma function. Among the considered models, it is noteworthy that the exponential distribution represents a special case of both the Gamma and Weibull distributions, occurring when the respective shape parameter k equals one. In this study, for each dataset of normalized RCS values, the parameters of the selected distribution were estimated using the Matlab™ mle function. Depending

on the distribution, this function either exploits a closed-form analytical solution, as in the case of the exponential distribution, or relies on iterative numerical optimization procedures when no explicit solution is available.

The results of this analysis for the X-band are presented in Table 14-(a) where the CVM distances relative to the considered statistical models have been evaluated for both drones across different areas and segments. Inspection of the table shows that, regardless of the area or segment considered, the normalized RCS measurements of the Mavic are best described by a Gamma distribution, whereas those of the Matrice 300 are more consistent with a Generalized Pareto model. The corresponding distribution parameters are reported in Table 14-(b).

This difference can be attributed to the size and structural complexity of the two UAVs. The DJI Mavic, being smaller and more compact, exhibits more stable and moderate RCS fluctuations, making the Gamma distribution a suitable model for its behavior. In contrast, the Matrice 300, which is significantly larger and structurally more complex, produces a wider range of RCS values, including occasional extreme peaks. These peaks are likely due to the increased surface area and the complex scattering mechanisms present in larger UAVs, which generate sporadic but intense radar returns. The Generalized Pareto distribution, recognized for its ability to model heavy-tailed data and extreme values, is therefore better suited to capturing the RCS variability of the Matrice 300. This behavior is also visually confirmed in Figure 36 and Figure 37, where the empirical CDFs are compared with the theoretical CDFs of all candidate statistical models.

A corresponding analysis was conducted for the L-band data (Figure 38 Figure 39), considering all four polarization configurations: VV, HH, VH, and HV. The CVM metrics between the empirical and theoretical distributions were calculated, and the outcomes are summarized in Table 15. As shown in the table, the best-fitting distribution depends on both the polarimetric channel and the UAV type. For the Mavic, the Weibull distribution provides the best fit in the co-polarized channels (VV and HH), whereas the Log-Normal distribution achieves the lowest CVM distances for the cross-polarized channels (VH and HV). In the case of the Matrice 300, the most suitable statistical model varies with the polarization channel, as

detailed in Table 15-(a): the Log-Normal distribution best describes VV, the Gamma distribution yields the best fit in HH, the Generalized Pareto provides the lowest CVM distance for VH, and the Weibull distribution performs best in HV. The parameters associated with each best-fitting model are reported in Table 15.-(b). These findings highlight the role of polarization in shaping the statistical behavior of the RCS and demonstrate that no single distribution can adequately capture all scenarios. This further emphasizes the importance of polarization-specific statistical modeling, particularly for complex UAVs such as the Matrice 300, where the larger size and irregular geometry lead to diverse scattering mechanisms.

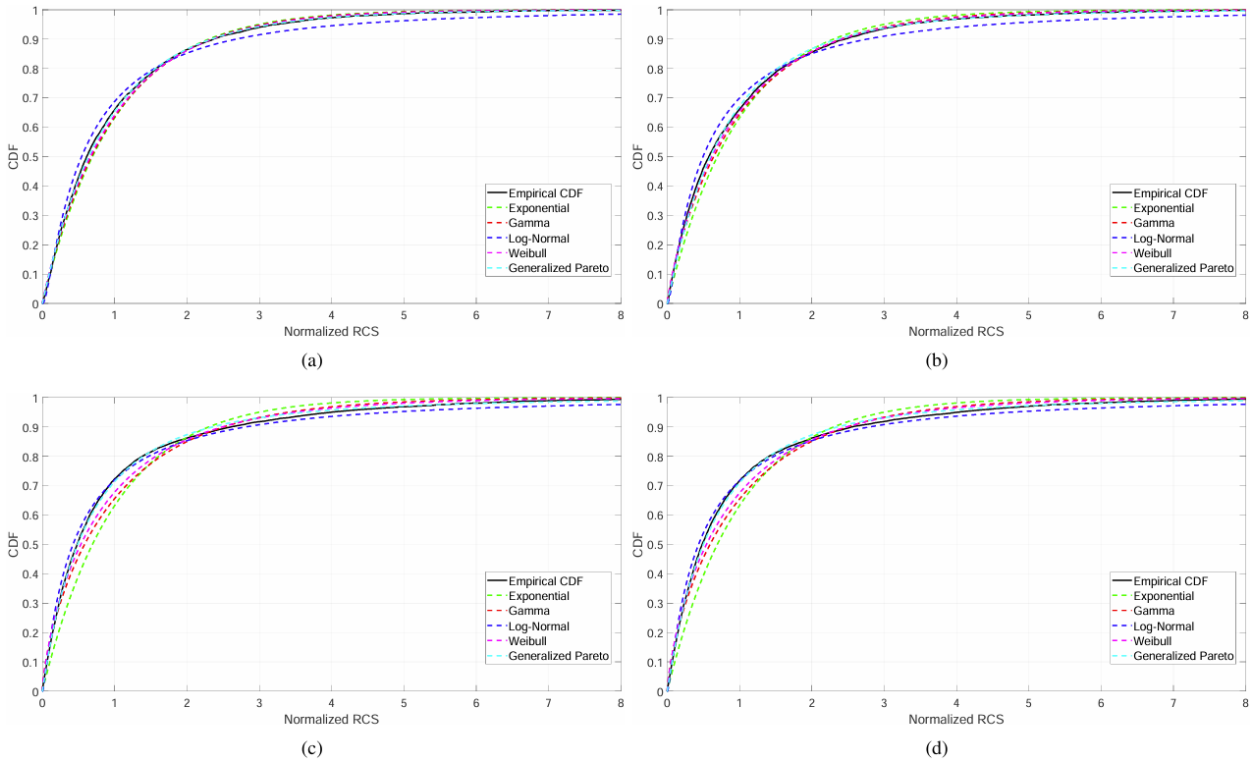

Figure 36. Comparison between empirical and theoretical CDFs of normalized RCS observations for the Matrice 300 drone in the X-band. Each subplot corresponds to a specific area and segment: (a) Area 1 – Segment 1, (b) Area 1 – Segment 2, (c) Area 2 – Segment 1, (d) Area 2 – Segment 2.

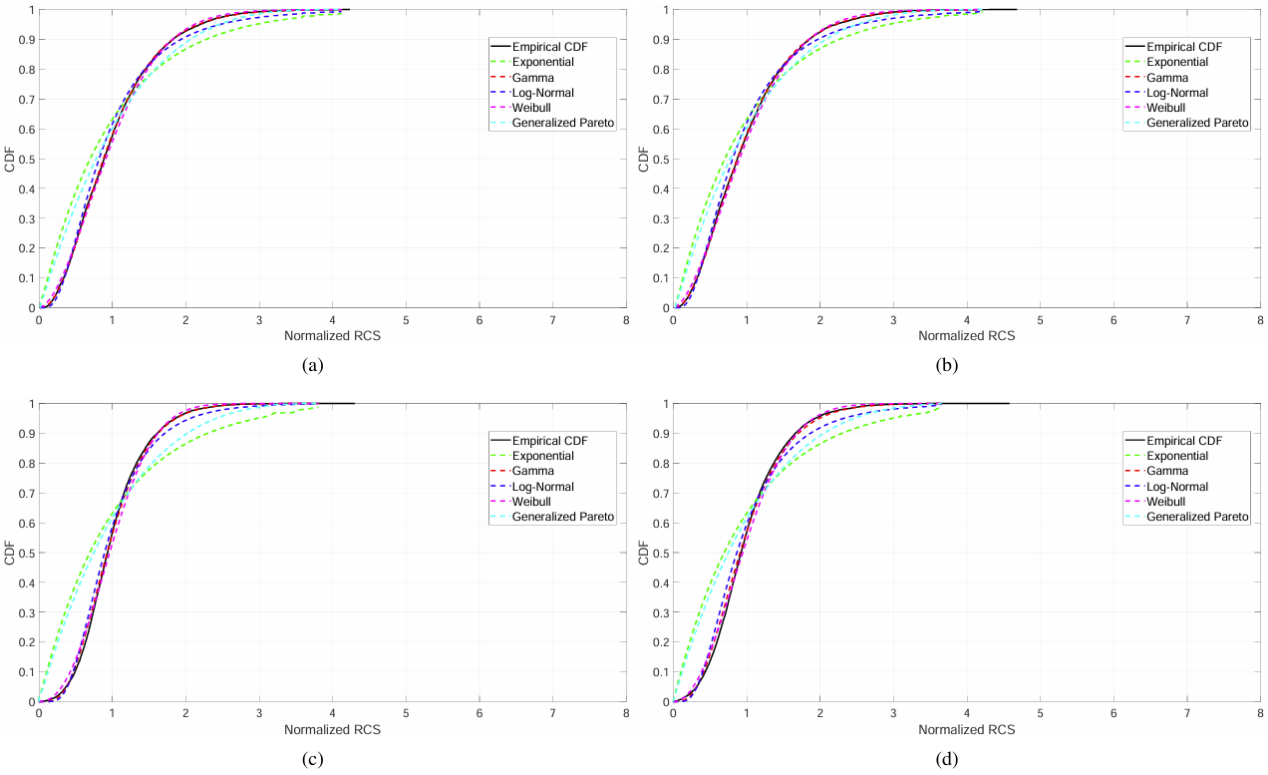

Figure 37. Comparison between empirical and theoretical CDFs of normalized RCS observations for the Mavic drone in the X-band. Each subplot corresponds to a specific area and segment: (a) Area 1 – Segment 1, (b) Area 1 – Segment 2, (c) Area 2 – Segment 1, (d) Area 2 – Segment 2.

		Area 1 Segment 1	Area 1 Segment 2	Area 2 Segment 1	Area 2 Segment 2
Matrice 300	Exponential	1.96	3.50	8.99	8.53
	Gamma	1.55	1.62	4.41	4.29
	Log-Normal	2.36	2.46	2.71	2.58
	Weibull	1.17	0.95	2.89	2.83
	Generalized Pareto	**0.61**	**0.95**	**0.68**	**0.73**
Mavic	Exponential	9.71	9.14	18.47	16.72
	Gamma	**0.37**	**0.40**	**1.67**	**2.04**
	Log-Normal	2.25	2.20	3.60	4.75
	Weibull	1.24	1.22	3.09	2.56
	Generalized Pareto	11.09	10.38	20.32	18.41

(a)

	Area 1 Segment 1	Area 1 Segment 2	Area 2 Segment 1	Area 2 Segment 2
Matrice	GP(ξ=0.1155, σ=0.8849)	GP(ξ=0.2029, σ=0.8017)	GP(ξ=0.4189, σ=0.6072)	GP(ξ=0.3969, σ=0.6262)
Mavic	G(k=2.6792, θ=0.3732)	G(k=2.5161, θ=0.3974)	G(k=4.6062, θ=0.2171)	G(k=3.6248, θ=0.2759)

(b)

Table 14. (a) CVM distances computed from the available RCS observations in the X-band for both drones across different areas and segments. (b) Parameters of the best-fitting distributions are also reported: for the Generalized Pareto distribution, the shape and scale parameters are denoted by ξ and σ, respectively, while for the Gamma distribution they are denoted by k and θ.

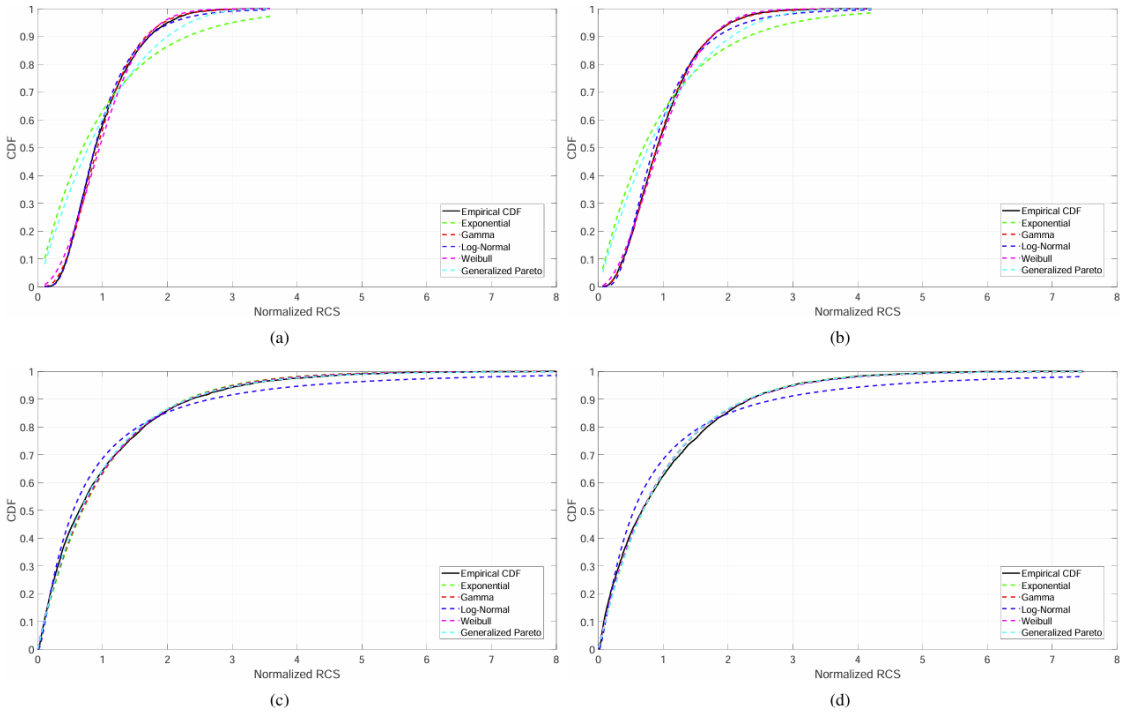

Figure 38. Comparison between empirical and theoretical CDFs obtained from different statistical models (Exponential, Gamma, Log-Normal, Weibull, and Generalized Pareto) for normalized RCS observations in the L-band acquired from the Matrice 300 drone. Results are shown for the four polarization channels: (a) VV, (b) HH, (c) VH, and (d) HV.

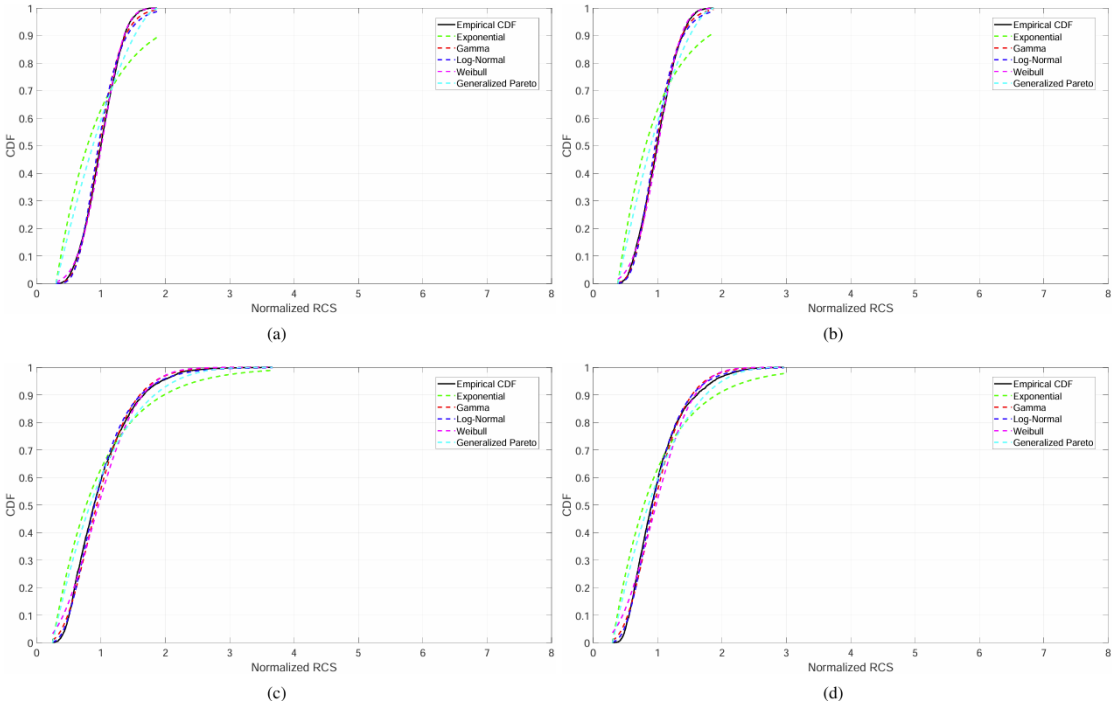

Figure 39. Comparison between empirical and theoretical CDFs obtained from different statistical models (Exponential, Gamma, Log-Normal, Weibull, and Generalized Pareto) for normalized RCS observations in the L-band acquired from the Matrice 300 drone. Results are shown for the four polarization channels: (a) VV, (b) HH, (c) VH, and (d) HV.

		Polarization VV	Polarization HH	Polarization VH	Polarization HV
Matrice 300	Exponential	11.56	10.31	1.63	1.44
	Gamma	1.26	**0.34**	1.28	1.12
	Log-Normal	**0.80**	1.91	2.32	3.13
	Weibull	2.37	1.21	0.98	**1.09**
	Generalized Pareto	13.17	8.19	**0.92**	1.38
Mavic	Exponential	12.71	12.67	9.49	10.59
	Gamma	1.23	1.12	1.56	1.72
	Log-Normal	1.79	1.59	**0.93**	**0.94**
	Weibull	**0.70**	**0.93**	2.34	2.80
	Generalized Pareto	16.39	16.33	10.61	12.16

(a)

	Polarization VV	Polarization HH	Polarization VH	Polarization HV
Matrice	LN(μ=−0.1290,σ=0.5183)	G(k=3.2650,θ=0.3062)	GP(ξ=0.0720,σ=0.9283)	W(λ=0.9878,k=0.9728)
Mavic	W(λ=1.1033,k=4.0244)	W(λ=1.1046,k=3.9366)	LN(μ=−0.1054,σ=0.4574)	LN(μ=−0.0818,σ=0.3992)

(b)

Table 15. (a) CVM distances computed from the available RCS observations in the L-band for both drones across different polarization channels. (b) Parameters of the best-fitting distributions: for the Log-Normal, the mean and standard deviation of the logarithm, denoted by μ andσ; for the Gamma, the shape and scale parameters, k and θ; for the Weibull, the scale and shape parameters, λ and k; and for the Generalized Pareto, the shape and scale parameters, ξ and σ.

6.1.9. Comparative Analysis of RCS behavior in X- and L-Band

A comparative assessment of RCS fluctuations in the X-band and L-band yields significant insights into the role of radar operating frequency in shaping both the statistical models and the dispersion characteristics of the observed data. The joint

analysis of the empirical cumulative distribution functions, dispersion indices, and corresponding best-fitting theoretical models allows several key considerations to be drawn.

First, the statistical distribution of normalized RCS values demonstrates a clear dependence on frequency, with notable variations observed across the two bands for each UAV. For the Mavic, a Gamma distribution provides the most accurate description in the X-band, whereas in the L-band the optimal model is polarization-dependent: the Weibull distribution achieves the best fit in co-polarized channels, while the Log-Normal distribution more effectively captures the behavior of cross-polarized channels. In contrast, the Matrice 300, which is well represented by a Generalized Pareto distribution in the X-band, exhibits a more complex statistical characterization in the L-band, with the most suitable model varying with polarization channel. These results emphasize the combined influence of both radar frequency and polarization on the statistical representation of RCS fluctuations.

Moreover, a distinction emerges between the two UAV platforms. The Mavic consistently displays a more stable and bounded RCS profile, whereas the Matrice 300 is characterized by greater variability and sporadic high-magnitude returns, which lead to heavier-tailed or spikier best-fitting distributions. Such differences can be directly ascribed to the physical characteristics of the UAVs, in particular their size, geometry, and structural complexity, which mediate the interaction between radar wavelength and scattering mechanisms.

In general, and consistent with theoretical expectations, the analysis reveals that RCS fluctuations exhibit higher dispersion in the X-band relative to the L-band. This trend is corroborated by the dispersion indices (standard deviation, interquartile range, full range, and box-and-whisker plots) reported in Table 12 and Table 13 Table 13, which consistently yield larger valuesin the X-band. Collectively, these findings confirm the frequency-dependent nature of UAV radar signatures and demonstrate that the variability of RCS tends to be more pronounced at higher operating frequencies.

6.2. Experimental Test Results

This study has provided a statistical characterization of the RCS fluctuations for in-flight UAVs, based on measurements obtained with an FMCW radar system operating in both X- and L-bands. Two distinct UAV platforms, the DJI Matrice 300 (professional-grade) and the DJI Mavic 2 Dual Enterprise (consumer-grade), were tested simultaneously to examine how RCS fluctuation models vary with drone type, radar frequency, and polarization.

Following a detailed description of the RCS estimation procedure and experimental setup, a first-order statistical analysis of the RCS measurements was conducted by evaluating the corresponding ECDFs. Additionally, a complementary analysis was performed to quantify the dispersion of RCS values under different conditions, employing statistical metrics such as standard deviation, interquartile range, full range, and box-and-whisker plots.

The results revealed that both the UAV type and the radar operating conditions significantly influence the statistical behavior of the RCS. Specifically, the Mavic drone, characterized by its smaller and more compact structure, exhibited more stable and constrained RCS fluctuations, which were well described by distributions such as Gamma and Weibull. In contrast, the larger and more structurally complex Matrice 300 displayed greater variability in its RCS behavior, which was more accurately modeled by Generalized Pareto or Log-Normal distributions.

A comparative analysis between X- and L-band measurements indicated that, for a given UAV, the most appropriate statistical model strongly depends on the frequency and polarization. These findings highlight both the structural differences between the two UAVs and the frequency-dependent nature of their radar signatures.

Future work could expand on this analysis by including additional UAV platforms and exploring more dynamic flight scenarios, particularly taking into account the presence of drone swarms.

7. RCS Enhancement Strategies: Passive and Active Systems

Ensuring a safe and sustainable environment for integrated drone operations requires a dual approach: on the one hand, advancing the performance of ground-based, multi-sensor surveillance networks, and on the other mandating that cooperative UAVs integrate technologies designed to increase their detectability. This cooperative strategy is essential to overcome the inherent challenges associated with detecting small, low-altitude flying objects, and it represents a fundamental prerequisite for the development of safe and efficient UAM.

For this reason, after the investigation of the best statistical behavior of the RCS first through simulation and then with the experimental validations, in this chapter several solutions designed to enhance the RCS of small drones are proposed and tested. The first solution involves a passive on-board system, more specifically an octahedral corner reflector. The second implements an active on-board system, which in for the current case of study is the Software Defined Radio (SDR). Through a series of on-ground and in-flight tests, this work aims to demonstrate the feasibility of both approaches, contributing to the development of a safer operational environment for future UAM [94].

7.1. RCS Enhancement Solutions

To enhance the RCS of an object, two primary classes of methods can be identified: passive and active solutions.

- **Passive solutions**, include shaping, surface coating, and the integration of reflective materials. In the case of shaping, the objective is to design the geometrical configuration of the target in such a way that the backscattered electromagnetic wave is maximized in the direction of the radar. With coating-based approaches, a layer with specific electromagnetic properties is applied to the target, resulting in a modification of the reflected wave characteristics and, consequently, an increase in the effective RCS. Beyond these strategies, standard practices frequently employ devices such as Luneburg lenses, corner reflectors, or other radio-reflective surfaces to achieve a similar enhancement.

- **Active solutions**, includes transponders, on-board radio systems, and airborne radar systems. Unlike passive methods, active techniques do not require modifications to the geometrical configuration of the UAV to increase backscatter. Instead, they leverage antennas and sensors located on the platform itself, which can contribute to RCS augmentation. In particular, active approaches require the implementation of systems capable of detecting the amplitude, frequency, phase, and angle of arrival of incident radar waves, and subsequently transmitting an amplified response signal. Such systems must be designed to be simple and flexible, while at the same time efficient and cost-effective.

The feasibility of both passive and active approaches depends on the fulfillment of specific requirements.

For passive systems, the key requirements are follows:

i. Proper design tailored to the specifications of the UAV to avoid structural or operational damage.
ii. Assurance of electromagnetic compatibility, ensuring that the system does not interfere with other drone communication signals (e.g., controller links).
iii. Compliance with payload constraints, maintaining the system weight within the allowable payload capacity of the UAV.
iv. Dimensional compatibility, such that the system size remains suitable for the UAV platform under consideration.

For active systems, the requirements largely mirror those of passive systems but also extend to operational and hardware-related constraints. In the context of this project, the chosen active solution is based on a SDR. Accordingly, the specific implementation must adhere to the guidelines detailed in [10], with particular regard to hardware limitations and integration with existing UAV subsystems.

The proof-of-concept scenario assumes the following system composition:

i. UAVs equipped with a camera, primary battery, propulsion system, receiver antenna, Inertial Measurement Unit (IMU), GPS, GNSS, and designated payload.

ii. A Ground Control System (GCS) comprising a surveillance infrastructure, a remote operator, a UAS Service Supplier (USS), and a Flight Information Management System (FIMS).

To examine in dept which are some of the most common solutions investigated for RCS enhancement, see [94]

7.1.1. Advantages and Disadvantages both of Active and Passive solutions

As benefit, passive RCS do not require power consumption, thereby simplifying integration on UAV platforms with limited energy availability. Their implementation and maintenance are straightforward, and the absence of active electronic components contributes to a high degree of reliability. Moreover, passive devices are generally cost-effective and suitable for basic applications, particularly when budgetary or operational constraints must be considered. Importantly, they do not introduce electromagnetic interference with the existing communication and control systems of the UAV.

Despite these advantages, passive solutions suffer from significant drawbacks. Their performance is strongly constrained by angular dependencies, resulting in limited coverage outside optimal orientations. The enhancement characteristics are fixed by design and cannot be adapted dynamically to changing operational conditions or radar frequencies. In addition, the introduction of extra weight and potential aerodynamic drag can negatively affect UAV endurance and maneuverability. These systems, therefore, remain less versatile in complex or highly dynamic operational scenarios.

Active RCS enhancement solutions provide superior capabilities compared to passive approaches. They offer adaptive frequency responses and the potential for omnidirectional coverage, thereby ensuring higher detection probability across different operational conditions. Active systems can be designed to optimize their performance in real time, leveraging advanced signal processing and integration with onboard UAV electronics. This adaptability positions them as strong candidates for future applications requiring robust and resilient detection solutions.

However, the benefits of active systems come at the expense of increased complexity. Power consumption requirements impose significant constraints on UAV platforms, especially those with limited payload capacities. The systems are also more costly, both in terms of initial development and ongoing maintenance. The reliance on active electronic components raises concerns about reliability, while the possibility of electromagnetic interference with other UAV subsystems must be carefully mitigated.

In Table 16, disadvantages and advantages of the different types of solutions are summarized.

Table 16. Summary of advantages and disadvantages of both passive and active systems.

	Advantage	**Disadvantages**
Passive Systems	No power required	Limited Angular Coverage
	Simple implementation	Fixed characteristics, no dynamic adaptation
	Hight reliability	Additional weight
	Cost-effective	Poor performance in dynamic scenarios
Active Systems	Omnidirectional coverage potential	High power consumption
	Real-time optimization	Higher costs
	Superior detection capabilities	Reliability concerns

7.2. Experimental Setup and Methodology: Passive System

The experimental validation of these RCS enhancement techniques required two distinct testing campaigns, each optimized for the specific characteristics and requirements of passive and active enhancement systems. The separation of these campaigns was driven by differing technical requirements, safety considerations, and measurement methodologies.

The passive enhancement experiments were conducted at a dedicated UAV testing facility featuring a netted area Figure 40 measuring 30 m in length and 8 m in

height. This facility was specifically designed to provide controlled outdoor conditions while ensuring safety compliance for drone operations. The netting material, constructed from high-strength polyethylene e fibers, provided containment for experimental flights while introducing minimal electromagnetic interference at the S-band operating frequency.

The test area featured a predominantly natural ground surface with scattered concrete elements, creating a realistic mixed-clutter environment representative of urban operational conditions. This environmental complexity, while introducing measurement challenges, provided valuable insights into RCS enhancement performance under realistic conditions where ground reflection and multipath effects cannot be neglected.

The radar system was positioned at a fixed location 5 meters from the primary test area, mounted on a stabilized platform at 1.5 meters above ground level. This positioning provided optimal coverage of the flight test volume while maintaining sufficient separation to avoid near-field effects that could compromise RCS measurements. The radar location was selected after site survey analysis to minimize unwanted returns from facility infrastructure while maximizing the signal-to-clutter ratio for drone targets.

Figure 40. Picture of the Netted Area at University of Naples Federico II in San Giovanni a Teduccio.

7.3. Passive System Radar Configuration

The measurement system for passive enhancement testing utilized the Ancortek SDR-KIT 240B, an S-band FMCW radar operating at 2.45 GHz. This system is selected for its software-defined architecture, which enabled flexible parameter adjustment and real-time data processing capabilities necessary for the experimental program. It is important to note that the selected radar frequency of 2.45 GHz, with its corresponding wavelength of 12.24 cm, is not optimal for small drone detection as it approaches the target dimension, potentially affecting measurement accuracy. Table 17 reports the characteristics of the chosen measurement system, highlighting also which should be the best value of a radar suitable for drone detection .

Table 17. ANCORTEK SDR-KIT 240B

Parameter	Value	Optimal Range	Impact on Measurements
Carrier Frequency [GHz]	2.45	8-15 GHz	Wavelength too large for small targets
Transmit Power [dBm]	22	> 30	Limited detection range capability
Bandwidth [MHz]	150	> 50	Poor range resolution (1.0 m)
Antenna Gain	15	> 20	Reduced sensitivity
Beam Width |[deg]	38 x 38	< 20 x 20	Broad coverage, lower gain
Polarization	HH –	Dual/Circular	Single polarization limits analysis

As passive enhancement system, a commercial octahedral corner reflector (Plastimo 16"), originally designed for maritime radar visibility enhancement of small vessels, is employed (see Figure 41). This reflector was selected through comparative analysis of available commercial systems, evaluating both peak RCS performance and average RCS stability across varying aspect angles.

The octahedral design provides theoretical maximum RCS of approximately 3.0 m^2 when optimally oriented, representing a potential enhancement factor of 300 relative to typical small drone RCS values of 0.01 m^2. However, this performance is strongly dependent on the relative orientation between the radar illumination angle and the reflector's geometric axis, with rapid degradation occurring as elevation angles exceed 30 degrees from optimal alignment.

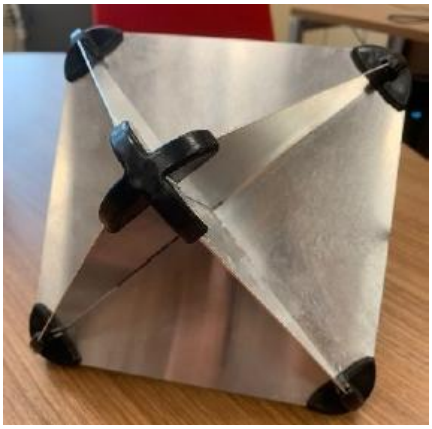

Figure 41. Platismo 16”^{TM} Octahedral Corner Reflector.

The mounting system for the corner reflector required careful engineering to minimize interference with drone flight characteristics while maintaining optimal electromagnetic orientation. A lightweight aluminum frame was fabricated to suspend the reflector beneath the drone fuselage, positioned to preserve the aircraft's center of gravity while ensuring unobstructed radar visibility. The complete mounting system added 0.78 kg to the drone's payload, well within the 6 kg capacity of the DJI Matrice 600 Pro [95] platform, chosen for the experiments, but representing a significant fraction of typical operational payloads.

7.3.1. Passive Tests Protocol

The passive enhancement test protocol was designed to systematically isolate the contribution of the corner reflector from background clutter, support structure returns, and the drone's intrinsic RCS. Six distinct test configurations reported in Table 18 were implemented to enable quantitative assessment of enhancement effectiveness. In Figure 42 (a) and (b), an example of the last two test performed is reported.

Table 18. Configuration of the test performed with the passive system.

Test ID	Configuration	Primary Objective	Analysis Focus
Test1	Support structure only	Background Characterization	Baseline establishment
Test2	Corner reflector on support	Passive enhancement validation	Peak RCS measurement
Test3	Drone static on support	Intrinsic drone RCS	Target baseline
Test4	Drone hovering flight	Dynamic baseline performance	Flight condition effects
Test5	Enhanced drone static	Combined RCS measurement	Enhancement qualification
Test6	Enhanced drone hovering	Operational performance	Real-Word Validation

The test sequence began with baseline measurements of the polystyrene support structure alone to establish its negligible contribution to radar returns. This material was specifically selected for its low dielectric constant and minimal radar reflectivity, ensuring that support structure contributions would not contaminate target measurements. Subsequent tests measured the corner reflector mounted on the support structure to establish its standalone performance characteristics. However, it is not reported the actual measured RCS value achieved during testing, limiting quantitative assessment of the reflector's performance relative to specifications.

Data acquisition employed continuous sampling over 30s intervals with 0.5 ms sweep times and 256 samples per sweep. This sampling strategy provided sufficient statistical basis for analysis while capturing temporal variations in system performance due to drone movement, rotor blade modulation and environmental effects.

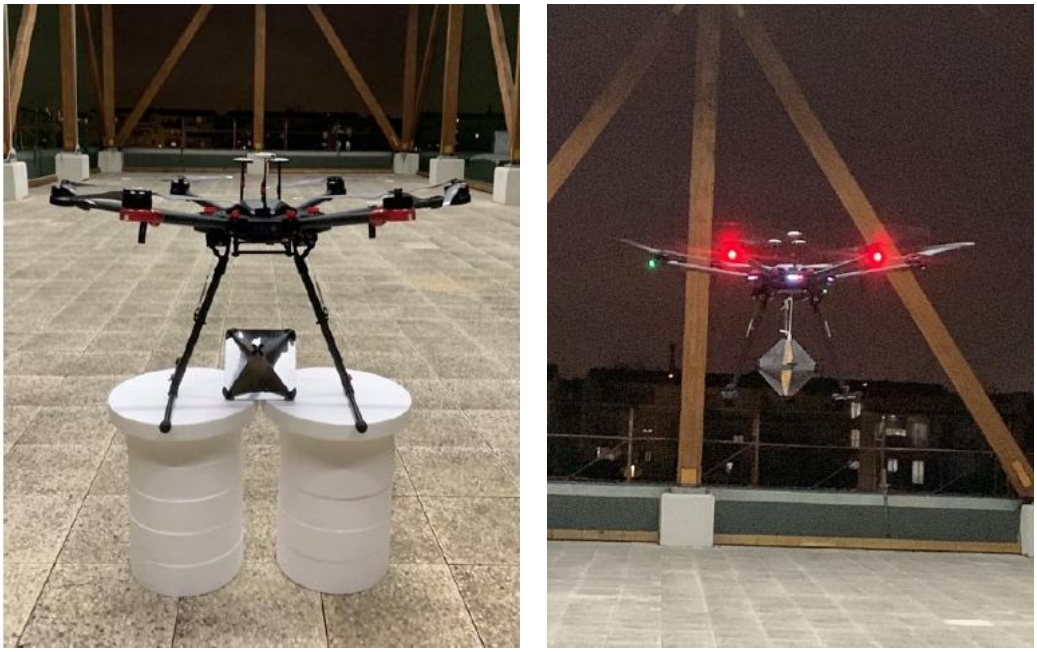

(a) (b)

Figure 42. Configuration of Test5 (left) and Test6 (right).

7.4. Passive System Results

The data processing was performed in MATLAB environment, applying the FFT. The intensity of the received signal versus time is analyzed for each test whereas for the Test4 e Test6 also the Range-Doppler map has been analyzed.

As indicated previously, the initial phase of passive system testing focused on establishing baseline performance characteristics and validating the measurement methodology. The polystyrene support structure (Test1) demonstrated negligible radar returns across the measurement range, confirming its suitability as a low-reflectivity mounting platform. In Figure 43 is reported a comparison between the Tests1/2/3/5.

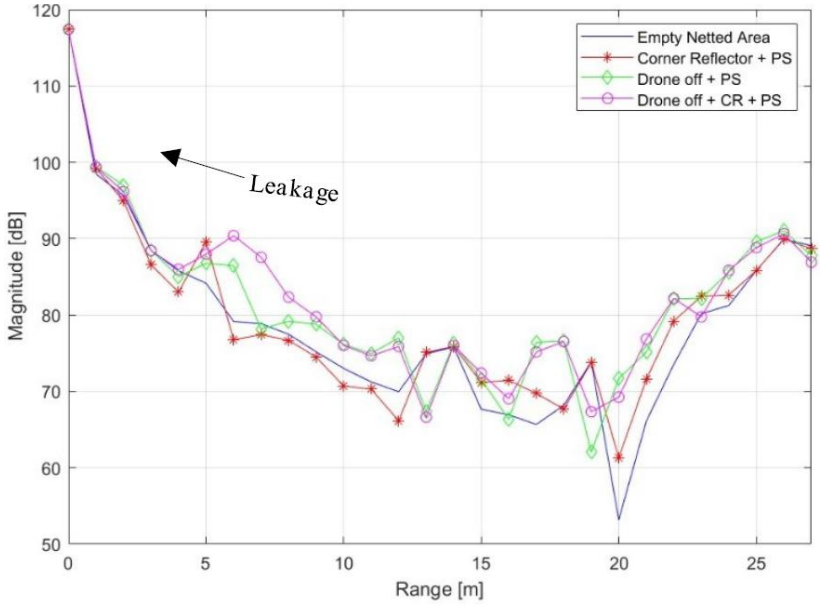

Figure 43. Comparison between the range profile of the empty Netted-Area with Test2, Test3 and Test5

In radar and telecommunications, leakage refers to an undesired signal that unintentionally couples from one component or channel into another, thereby reducing measurement accuracy. In FMCW radars, for instance, leakage occurs when a portion of the transmitted signal directly enters the receiver masking or degrading the useful target echo. More generally, in RF systems, leakage denotes the loss of isolation between transmitter and receiver, or between different channels, which results in interference and a lower signal-to-noise ratio. Typically it occurs when the TX and RX antennas are not well separated.

As concerns radar signature of the DJI Matrice 600 Pro, it was characterized under both static (Test3) and hovering flight (Test4) conditions. During hovering flight measurements, micro-Doppler signatures from the rotating propeller blades have been observed, though detailed analysis of these signatures is not provided in the current research. However, the Range-Doppler processing revealed characteristic modulation effects, but the limited range resolution of 1 m prevented detailed characterization of individual rotor contributions.

The comparative analysis between drone measurements with and without the corner reflector demonstrated measurable enhancement in the radar return. Note that for the comparison in the hovering mode, the drone is positioned at 10 m from the radar

equipment. In Figure 44 is possible to appreciate the range profiles comparing different test configurations, with visible increases in signal amplitude when the corner reflector is present.

The reduction of peak amplitudes observed during the hovering mode of the Matrice 600 can be attributed to several concurrent factors. First, the performance of the corner reflector is strongly dependent on the elevation angle, leading to an average decrease in the RCS as the elevation angle increases. Moreover, when the drone is not perfectly aligned with the radar boresight, gain losses occur, further degrading the overall performance. Another contributing factor to the reduction of RCS peaks is the high level of multipath interference, which is particularly enhanced by the presence of the Netted-Area structure. Finally, range resolution limitations imposed by the 150 MHz bandwidth, corresponding to approximately 1.0 m resolution which is comparable to the physical dimensions of the drone, significantly affect measurement accuracy, thereby reducing the clarity of the observed radar returns.

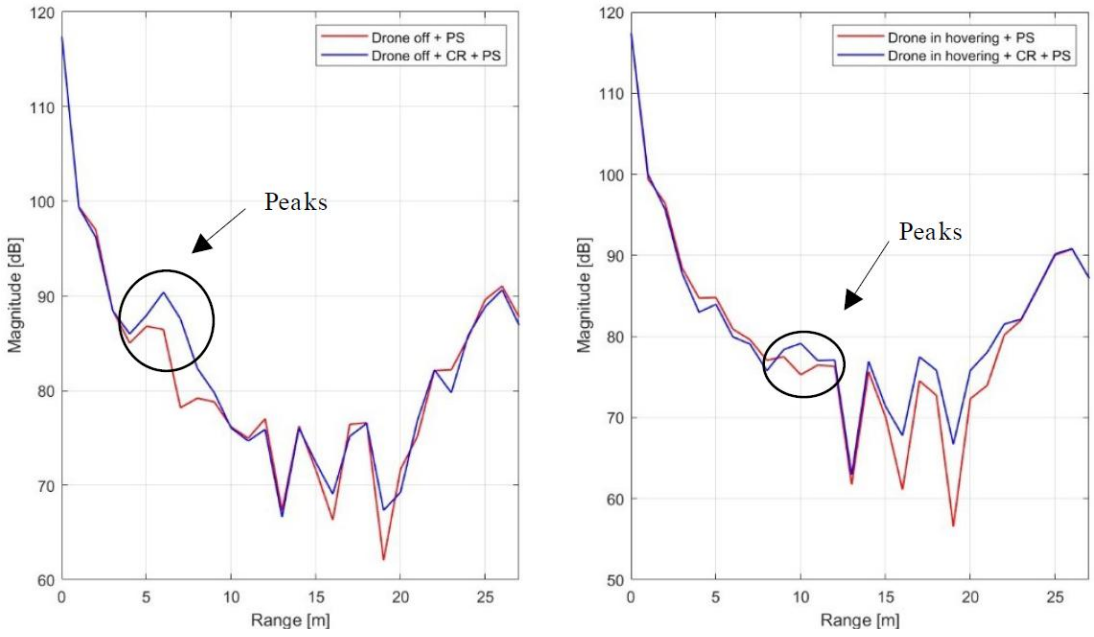

(a) (b)

Figure 44. Comparison between the range profile of drone with and without the Corner reflector: (a) Drone in static mode (Test3 & Test5), (b) Drone in hovering Test4 & Test6).

As conclusion of the results obtained with the passive system, a table which shows the environmental limitations identified is reported below in Table 19.

Table 19. Summary of results obtained during tests with passive system.

Limitation Source	Effect Described	Impact on Measurement
Netted Facility	High multipath interference	Signal distortion and false returns
Radar Frequency Selection	Wavelength (12.24 cm)	Reduced measurement accuracy
Range Resolution	1.0 m resolution vs 1.5 m drone dimensions	Inadequate target discrimination
Elevation Angle Dependency	Performnce degradation with increasing angles	Operational utility limitations
Background Clutter	Peaks at 27 m from facility structures	Measurement contamination

7.5. Experimental Setup and Methodology: Active System

Based on the system requirements, which were defined in accordance with the IEEE Standards guide [96]. and tailored to the objectives of the project, the system configuration illustrated in Figure 45 was designed.

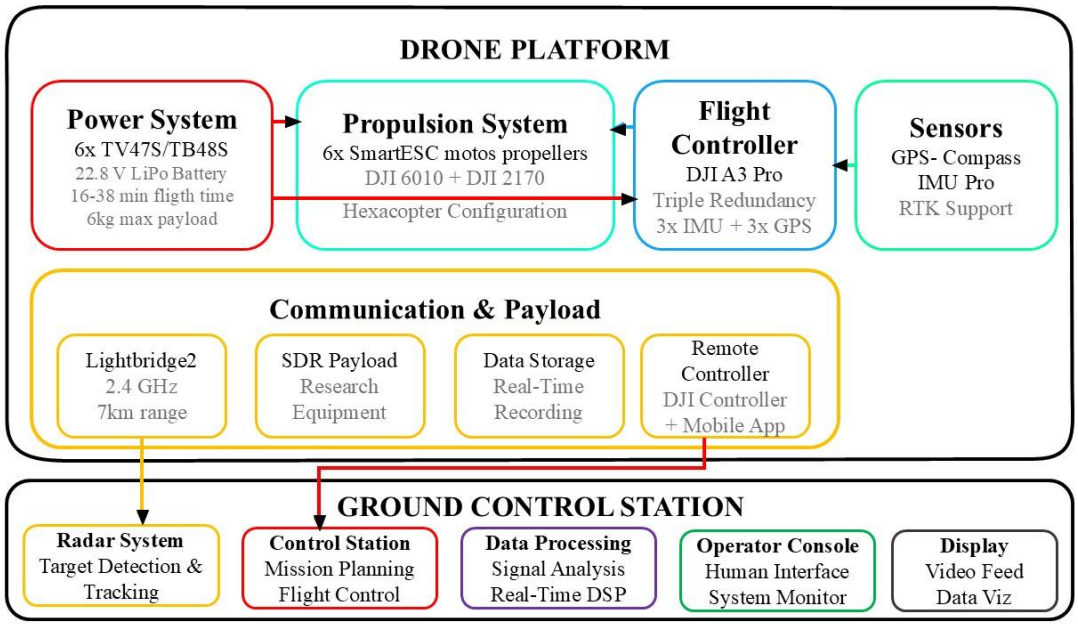

Figure 45. System Configuration of the experiment with the Active System.

The test equipment comprised the following components:

- DJI MATRICE 600 PRO;
- HackRF One SDR Transceiver [97];
- Ancortek SDR Evaluation Kit 240B [98].

The software-defined radio requires dedicated software for signal modulation and demodulation. The HackRF One is compatible with GNU Radio, a software development platform that provides signal processing functions to implement SDR. The digital processing blocks were developed in C++, while the interconnection between blocks was implemented in Python [99–101]. GNU Radio allows precise configuration of sampling rate, carrier frequency, and RF gain. The parameter settings applied during the tests are summarized in Table 20.

Table 20. GNU Radio parameter setting for the experiment of active system.

GNU Radio Settings	
Parameter	**Value**
Frequency [GHz]	2.54
RF/IF/BB Gains [dB]	40
Sample Rate [MS/s]	10

The experimental methodology involved positioning two computers within the test area:

- The first computer was connected to the SDR transceiver installed on-board the drone, transmitting the desired configuration to the HackRF One via GNU Radio, as illustrated in Figure 47– (a).
- The second computer was connected to the Ancortek radar detector, which, through SDR-Sharp software, both transmitted a signal from the ground radar and recorded the response signal received by the SDR, as illustrated in Figure 47– (b).

Using SDR-Sharp, a FMCW signal, i.e. a tone (X_T),was transmitted from the ground radar at 3.58 MHz with a carrier frequency of 2.4667 GHz. The on-board system retransmitted the signal back to the radar via the antenna installed beneath

the drone (X_{TRT}), and the returned data were acquired on the ground by a Data Acquisition System (DAQ), composed of measurement hardware and a computer with programmable software. It is important to note that the signal received by the radar corresponds to the sum of the actively retransmitted signal (X_{TRT}) and the passively reflected signal from the drone's structure (X_{RR}).

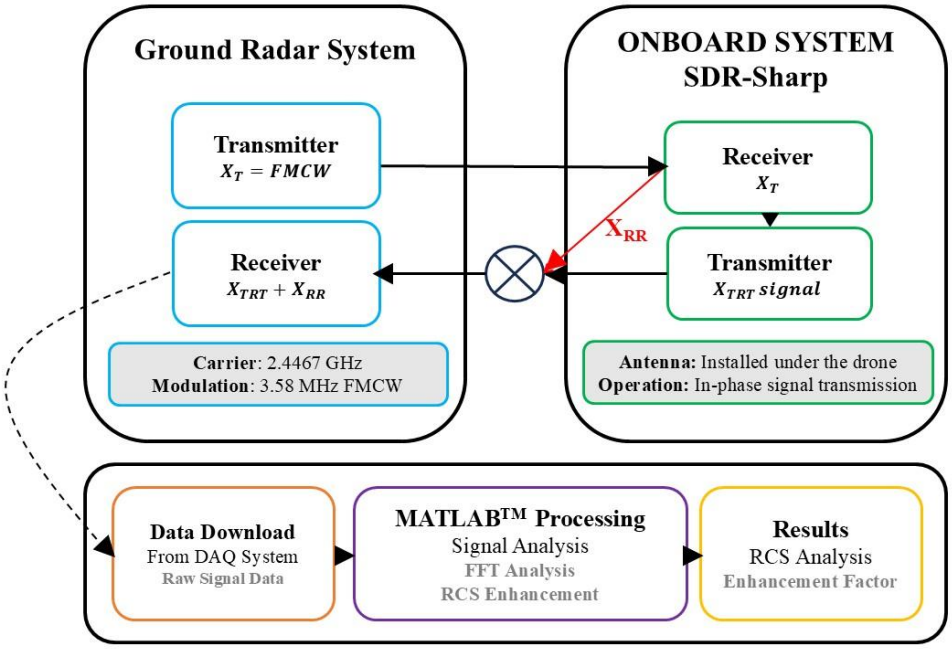

Figure 46. Test Development and Procedures with the Active System.

Following the acquisition, the data were downloaded and processed offline in the Matlab™ environment for detailed signal analysis. The operational workflow is schematically represented in Figure 46. A fundamental requirement for achieving radar cross-section enhancement is that the actively retransmitted and passively reflected signals remain in phase, ensuring constructive interference and maximizing the effective radar return.

(a) (b)

Figure 47. Experimental setup for the tests with the active system: (a) configuration with the first computer connected to the SDR transceiver installed on-board the drone; (b) configuration with the second computer connected to the Ancortek.

7.5.1. Active System Principle for RCS Estimation

As discussed in the previous section, the active enhancement approach does not rely on modifications of the target's geometric configuration to increase the RCS. The underlying principle of any active system can be derived from the classical radar equation, expressed by (19). In the case of an active enhancement system, the power received by the device, p_r, and the transmitted power retransmitted, p_t, can be expressed as:

$$p_r = P_t G g_r \left(\frac{\lambda}{4\pi R}\right)^2 \tag{25}$$

$$p_t = g_a p_r \tag{26}$$

Where g_r is the gain of the device receiver and g_a is the amplification gain of the active system between the receiver and transmitter antennas, Combining these espressions yields an equivalent radar equation for the active system:

$$P_R = p_t g_t G \left(\frac{\lambda}{4\pi R}\right)^4 \tag{27}$$

Comparison of this expression with the classical radar equation allows the derivation of the equivalent active radar cross section σ_a:

$$\sigma_a = \frac{g_r g_a g_t \lambda^2}{4\pi} \tag{28}$$

Furthermore σ_a can also be expressed in terms of the effective areas of the device transmitter S_t and receiver S_r as:

$$\sigma_a = \frac{g_a S_t S_r 4\pi}{\lambda^2} \tag{29}$$

These formulations quantitatively describe how the active system enhances the radar cross-section by amplifying and retransmitting the incident radar signal, independently of the target's physical geometry, and provide a rigorous framework for evaluating active enhancement performance.

7.5.2. Software Defined Radio Principle

The SDR is a radio communication system that employs reconfigurable, software-based components for the processing and conversion of digital signals [102]. This architecture is primarily composed of two functional blocks: the Radio Front-End (RFE) and the digital backend.

The RFE encompasses the antenna impedance interface, the receiver, and the transmitter, and includes all the analog circuitry required to transmit and receive high-quality signals. The digital backend, in turn, may consist of a Field-Programmable Gate Array (FPGA), a General-Purpose Processor (GPP), or a Digital Signal Processor (DSP). Among these options, the FPGA is generally preferred due to its reconfigurable logic gates, which enable multiple functions with high power efficiency and moderate costs [102]. Further details on SDR architecture are available in [102]. The inherent versatility and flexibility of SDRs, primarily afforded by the FPGA, make this class of systems particularly suitable for the objectives of the present project.

The advantages of SDRs can be summarized as follows [103,104]

i. Flexibility: Controlled via software, the same SDR hardware can be configured for different applications. Depending on system requirements,

the software can adjust the RF carrier frequency, modulation type, sampling frequency, and forward error correction (FEC) techniques, thereby minimizing interference with other communication channels.

ii. Common Hardware: SDRs allow the substitution of analog components with COTS or general-purpose hardware, simplifying the overall system design.

iii. Reduced System Costs: This benefit arises from the combination of software-based flexibility and the use of common hardware components.

However, several limitations are also present:

i. Integration Challenges: The hybrid nature of SDRs, comprising an analog RF front end and a digital backend, complicates interfacing between the two domains. Moreover, the performance of the analog-to-digital converter (ADC) imposes a maximum frequency limit for the digital components.

ii. Dynamic Range Limitations: Some SDR designs exhibit poor dynamic range, defined as the ratio between the largest tolerable signal and the smallest usable signal.

iii. Software Development Complexity: Implementing software for different target systems remains challenging, requiring significant development effort.

7.5.3. Results with Active System

The active system testing included six different operational configurations showed in Table 21. Active System Test Configurations to assess performance under various flight conditions . The results showed varying levels of active response depending on the specific maneuver being performed (see Figure 48).

The baseline performance is established during Test T1, with the drone in stationary condition but with active rotors. This configuration provided a stable reference for evaluating the impact of flight dynamics on active system performance. The hovering configuration (Test T2) demonstrated the system's capability to maintain active enhancement during typical operational flight conditions.

Table 21. Active System Test Configurations

Test ID	Flight Condition	Type of maneuver
T1	Stationary with active rotors	Active response detected
T2	Hovering configuration	Active response detected
T3 & T4	Flight with altitude changes	Active response detected
T5	360° rotation around vertical axis	Weakest response observed
T6	Data acquisition during landing	Active response detected

During the 360° rotation of the drone at constant angular velocity (Test T5), a reduction in the system response was observed, attributable to the presence of the landing gear. This outcome illustrates that the physical configuration of the aerial platform can exert a significant influence on the radiation patterns of the active system's antennas, inducing shadowing and blockage effects that compromise enhanced performance.

Rotational testing thus highlights intrinsic limitations of the active system arising from the interaction between antenna patterns and platform geometry. The observed performance degradation underscores the critical importance of both the placement and orientation of the active system antenna relative to the drone structure in achieving optimal functionality.

In contrast to passive corner reflectors, whose performance is largely determined by predictable geometric factors, the orientation sensitivity of the active system is primarily governed by electromagnetic effects. Obstruction caused by the landing gear generates shadowing that reduces both the signal received from the ground radar and the effective power retransmitted toward it, thereby diminishing the enhancement.

The efficacy of the active enhancement system fundamentally relies on maintaining constructive interference between the active return and passive reflections. Radar

cross-section enhancement is attainable only when the signals remain in phase, emphasizing the pivotal role of phase coherence in ensuring correct and reliable system operation.

Moreover, the validation of the active enhancement was performed through spectral analysis of the signals received at the ground radar. The peaks in the spectral amplitude distribution, as illustrated in Figure 48, correspond to measurable responses associated with the active system operation under different flight conditions, confirming the feasibility of the approach.

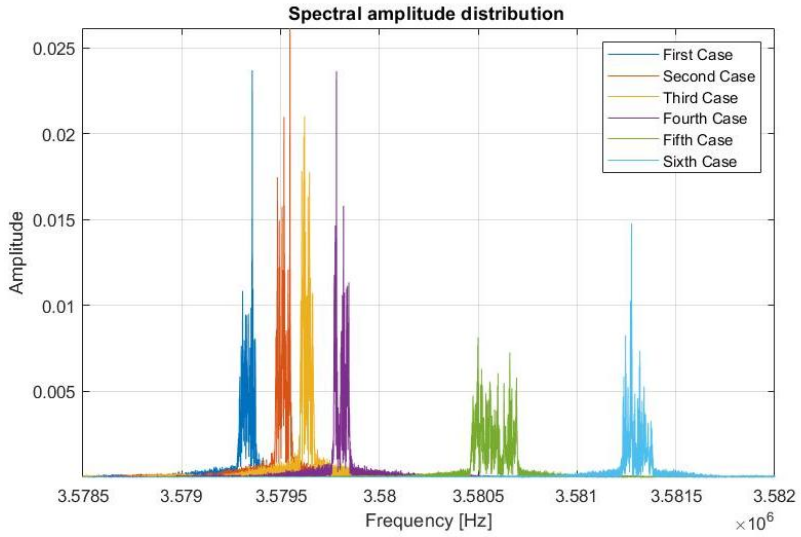

Figure 48. Peaks of the spectral *amplitude* distribution for each Test with the active system on-board

As conclusions, the active enhancement system effectively demonstrated the fundamental principles of signal detection, processing, and retransmission across all test configurations. Coherent signal processing and retransmission of the incident radar signals from the ground-based Ancortek system were successfully achieved using the HackRF One SDR platform, with amplified returns observed for each test condition.

8. Cooperative Multi-Agent System for Autonomous Detection of Target in Semi-Structured Urban Environments

The evolution of autonomous systems in defense and security applications has increasingly focused on cooperative multi-agent architectures capable of operating in complex, semi-structured environments. This chapter presents the experimental validation of the S.APR.AI (Swarm - APR - Artificial Intelligence) project, which addresses the fundamental challenge of autonomous target library generation through heterogeneous platform cooperation. The research demonstrates how aerial and terrestrial robotic systems can collaborate effectively to detect, classify, and track targets in realistic urban scenarios, representing a significant advancement in autonomous surveillance and reconnaissance capabilities. The methodology presented here validates both individual agent performance and collective system behavior, establishing a comprehensive framework for multi-agent target detection systems that can adapt to dynamic operational requirements while maintaining robust performance under real-world constraints.

8.1. Swarm Robotic Systems

Swarm robotic systems, particularly those involving Unmanned Aerial Vehicles, represent one of the most transformative developments in modern robotics, offering unprecedented operational capabilities while simultaneously presenting significant technical and operational challenges that demand careful consideration [105]. A drone swarm, defined as "Smart War-Fighting Array of Reconfigured Modules," constitutes an emerging concept involving numerous autonomous and cooperative unmanned aerial systems that operate as a single organism to achieve common objectives [106]. Rather than simply coordinated drone operations, these systems represent cooperative robotics where drones communicate among themselves and autonomously change their behavior, exhibiting complex emergent performance that surpass individual unit capabilities.

These systems excel through distributed sensor grids where complementary capabilities create comprehensive data collection impossible with individual units, while parallel processing dramatically reduces mission completion times at lower costs than complex single platforms. The most significant advantage lies in exceptional fault tolerance, where individual unit losses are instantly compensated through task reassignment, ensuring mission continuity and superior destruction resistance [105,107,108]. This scalability operates through both homogeneous identical-unit configurations and heterogeneous arrangements incorporating combat, reconnaissance, communication, and decoy capabilities for enhanced operational effectiveness.

However, these advantages come with inherent complexities that increase proportionally with system scale [105,106]. Control complexity escalates as UAV numbers grow, making effective management by single operators increasingly challenging, requiring advanced command and control models such as "emergent coordination" where coordination naturally arises from individual swarm element reactions. The human-system interface presents significant complications, with large, complex, or heterogeneous swarms placing substantial cognitive demands on human operators, potentially leading to delayed reaction times and difficulty in accurately predicting swarm behavior while maintaining optimal control. Technical limitations further compound these challenges, as large swarms require vast information processing capabilities with increased collision risks, while continuous inter-unit communication creates vulnerability to electronic disturbances that can disrupt coherent functioning.

Autonomy levels ranging from "human in the loop" to "human out of the loop" introduce ethical and security dilemmas, including concerns about losing control or algorithmic errors. Current hardware limitations constrain capabilities through equipment restrictions, size and weight constraints, battery life limitations, and onboard computational capacity restrictions. The widespread deployment of swarm systems requires comprehensive regulatory framework development to ensure safety while addressing legal and ethical concerns.

In military contexts, swarm robotics represents a revolutionary force multiplier that fundamentally transforms battlefield dynamics through overwhelming enemy defenses with coordinated multi-vector attacks, creating impenetrable reconnaissance networks that provide comprehensive situational awareness, and establishing resilient communication infrastructures that remain operational despite individual unit losses. The psychological impact on adversaries cannot be understated, as swarms create fear and uncertainty while their distributed nature makes traditional countermeasures ineffective [109]. Most importantly, swarms execute precision strikes against multiple targets simultaneously while their numerical superiority overwhelms defensive systems designed for single-threat scenarios [106].

Moreover, specific military defense applications highlight the tactical versatility of swarm systems. These swarms offer rapid area defense capabilities, operating near sensitive zones or safeguarding carrier aircraft by facilitating their escape from high-risk areas. A notable early example is the experiment conducted in [108], aimed at designing, developing, and testing drone swarms as a countermeasure against ground-based radar detection.

The objective of the following project is to build upon and evolve the foundation laid by previous work. More specifically, it focuses on the development of drones equipped with advanced AI and Machine Learning (ML) capabilities, with the following key goals

- Testing and validation of swarming logics and algorithms
- Development of Counter-Unmanned Aircraft Systems (CUAS) strategies based on machine learning techniques
- Autonomous target recognition and classification

This evolution aims to enhance the adaptability and intelligence of drone swarms, enabling more sophisticated behaviors in dynamic and contested operational environments.

8.2. Experimental Setup

The experimental setup employs a heterogenous multi-agent system designed to simulate realistic operational scenarios. More specifically, the system comprises:

- Two autonomous aerial drones STANIS 1 & 2 (Figure 49-(a) and Figure 49-(b)) equipped with electro-optical (EO) sensors, which for this case study is ZED 2i [110].

- One terrestrial robot (see Figure 49-(c)) with ground reconnaissance capabilities, equipped both with camera ZED 2i and an Infrared (IR) Camera, that for this application is Optris PI 640i [111] .

- Three UAS targets, two provided by RSV and one DJI Mavic Enterprise platform.

- One mannequin target.

Two drones STANIS work as autonomous aerial drones cooperatively with the terrestrial robot within the prepared urban scenario. The aerial platforms integrate ZED 2i cameras for electro-optical target detection, while the terrestrial robot incorporates infrared sensing capabilities for thermal signature detection. All artificial intelligence processing operates on electro-optical characteristics to ensure consistent sensor modality across the detection pipeline, but also on IR characteristics for the identification and classification of targets.

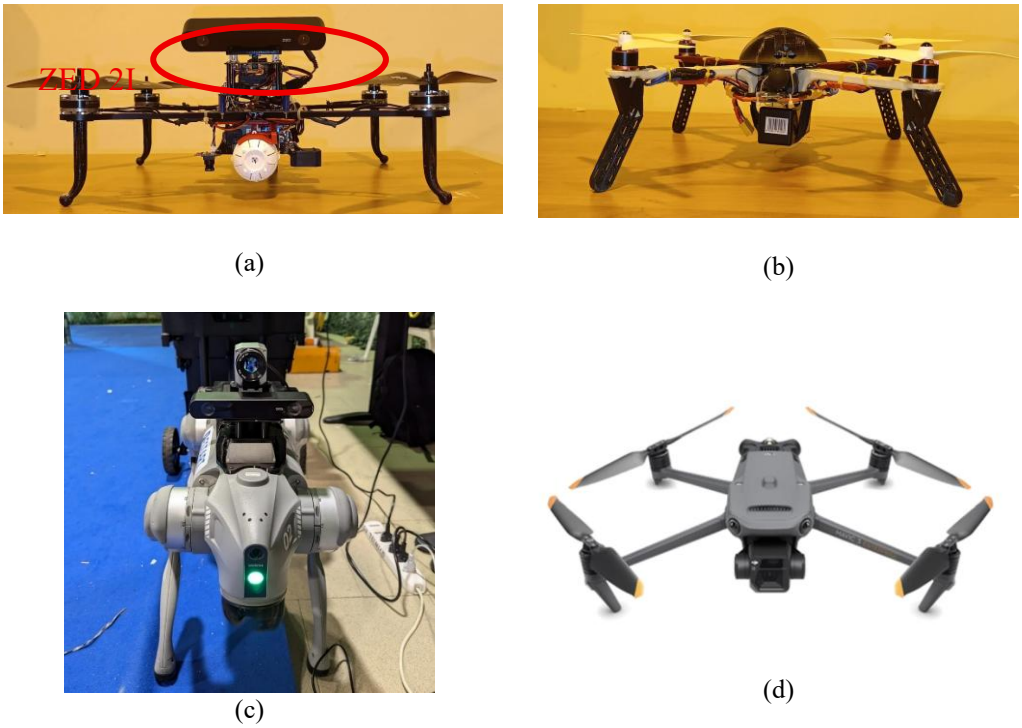

Figure 49. Multi-agent system designed to simulate realistic operational scenarios: (a) Drone STANIS equipped with camera ZED 2i, (b) Drone target, (c) Terrestrial robot equipped both with camera ZED 2i and one IR camera Optris PI 640i, (d) DJI Mavic Enterprise

The experimental environment features a comprehensive control station providing real-time visibility over algorithmic processes, image acquisition systems, library generation procedures, and continuous system monitoring.

8.2.1. Team

The experimental validation employs a distributed testing approach across three specialized facilities, each contributing unique capabilities to the overall research framework. The “Reparto Sperimentale di Volo” (RSV), in the framwork of the RPW project, provided the primary development environment through its CUTE Laboratory, which supports programming, development, and system integration activities. This facility includes an indoor test range specifically designed for controlled flight testing and initial system validation procedures.

The University of Rome Tor Vergata contributes advanced laboratory facilities dedicated to algorithm development and refinement. These facilities include sophisticated indoor test ranges that enable preliminary system validation under controlled conditions, allowing for iterative algorithm optimization before deployment in more complex scenarios.

The University of Naples - Advanced Metrological and Technological Services Center (CeSMA) facility provides the most comprehensive testing environment through its Laboratory for Innovative Flight Technologies (LIFT) , which supports advanced testing protocols and extended validation procedures. The facility includes both outdoor test ranges for realistic operational scenario simulation and the Castel Volturno flight field, which accommodates large-scale demonstrations and final system validation exercises. Moreover, the integration of the thermal sensor and the automatic detection through AI has been supported.

The test environment undergoes systematic modification to simulate urban operational conditions while maintaining experimental control. Environmental standardization includes the implementation of homogeneous floor coverage designed to eliminate background visual inconsistencies that could affect detection algorithm performance. Wall and window coverage protocols remove potential visual artifacts that might introduce detection bias or false positives during autonomous scanning procedures. The figure shows an example of how the scenario is set up.

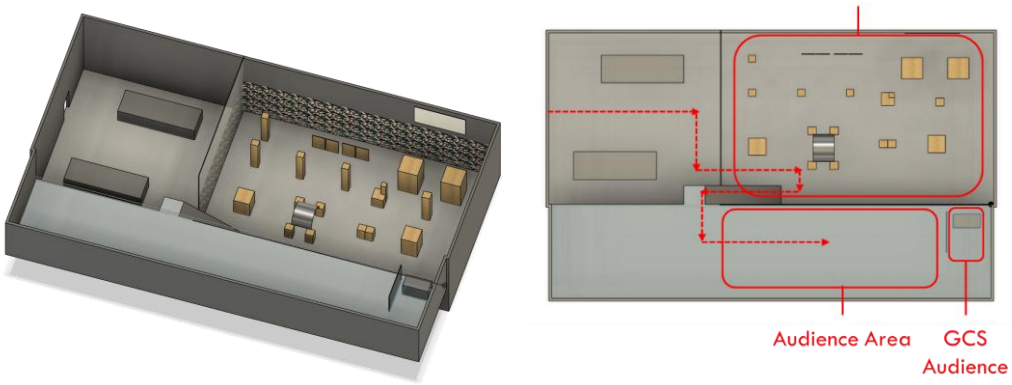

(a) (b)

Figure 50. DEMO Scenario Set-up

8.3. Methodology and Work

To organize as well as possible the division of tasks, a set of work packages (WP) has been drafted as shown in Table 22.

The methodology implements systematic work package organization addressing all technical aspects of the cooperative multi-agent system. Infrastructure development (WP-01) establishes the indoor test range with scenario decoration and environmental preparation. Target development (WP-02) provides the three target platforms with appropriate electro-optical characteristics for detection algorithm validation.

Platform development encompasses autonomous drone construction (WP-03), sensor integration for both electro-optical and infrared capabilities (WP-04), and terrestrial robot programming (WP-05). In Figure 51 is shown a demonstration of how the image for electro-optical sensor training has been acquired.

(a)

(b)

Figure 51. Images acquired to train the ZED 2i for the autonomous target recognition algorithm.

Cooperative behavior implementation includes swarming logic programming (WP-06) and datalink integration (WP-07) for inter-agent communication and coordination.

Artificial intelligence algorithm development addresses ground target recognition (WP-08), autonomous library generation (WP-09), and aerial target recognition (WP-13). System integration (WP-10) ensures seamless operation across all platforms and algorithms, while specialized capabilities include payload release system integration (WP-11) and autonomous payload deployment testing (WP-12).

Table 22. Work Package Status Matrix showing completion, responsibilities, and requirements for each WP.

WP-01	Infrastructure development for indoor test range with scenario decoration and environmental preparation	RSV
WP-02	Development of Electro-optical characteristics for detection algorithm validation	UNINA
WP-03	Development of two autonomous drones	RSV-TOR VERGATA
WP-04	Integration both of electro-optical sensors on two autonomous drones and one IR on terrestrial robot	TOR VERGATA
WP-05	Terrestrial robot programming	TOR VERGATA
WP-06	Cooperative behavior implementation includes swarming logic programming	TOR VERGATA
WP-07	Datalink integration for inter-agent communication and coordination	ALL
WP-08	Development of the autonomous ground target recognition algorithm	UNINA
WP-09	Autonomous library generation	UNINA
WP-10	Algorithms integration	ALL
WP-11	Payload release system integration	RSV UNINA
WP-12	Autonomous payload deployment testing	RSV-UNINA
WP-13	Development of the autonomous aerial target recognition algorithm	UNINA

8.3.1. Timeline

The experimental campaign followed a structured timeline from initial mission definition (February–March 2024) to final demonstration (October 2024). The key phases are:

- Algorithm development and platform construction (April – May 2024)
- System integration and rigorous testing (June – August 2024)
- Final refinements and demonstration preparation (September – October 2024)

This phased approach ensured balanced development across all work packages while preserving system coherence and readiness for deployment. By embedding iterative testing and refinement throughout the cycle, the methodology guaranteed robust performance at the final demonstration, validating both technical maturity and operational reliability.

8.3.2. Live Trial

The simulation is divided into three phases as follows.

- *Phase 1*: Autonomous Exploration.
- *Phase 2*: Multi-modal Cooperative Target Engagement.
- *Phase 3*: Dynamic Target Interception.

8.3.3. Phase 1: Autonomous Exploration

The initial experimental phase (see Figure 52) validates basic autonomous target detection and library creation capabilities under controlled conditions. Two autonomous drones conduct coordinated aerial surveillance operations over the prepared urban-like scenario, engaging three EO/IR suitable targets positioned throughout the urban environment. The experimental protocol operates under a strict thirty-minute duration constraint to ensure operational relevance.

The test involves the take-off of two autonomous drones in a simulated urban scenario and its exploration. The library generation phase represents the core innovation of this methodology, implementing autonomous creation of target libraries based exclusively on acquired electro-optical characteristics. The system generates comprehensive target profiles supporting subsequent recognition

operations, with real-time database integration and classification accuracy validation. The phase concludes with autonomous landing procedures, demonstrating complete mission autonomy from takeoff to landing.

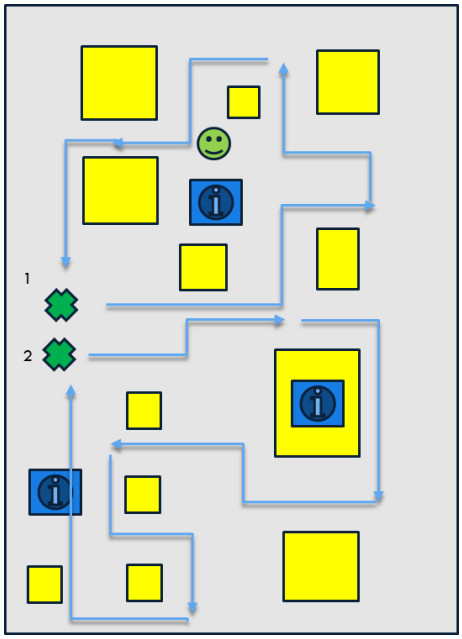

Figure 52. Scenario example of the first phase of the experiment

8.3.4. Phase 2: Multi-Modal Cooperative Target Engagement

The second experimental phase (see Figure 53) introduces cooperative behavior between aerial and terrestrial platforms while incorporating thermal signature detection capabilities. This phase employs standby aerial platforms while the terrestrial robot conducts autonomous search protocols for thermally-active targets, demonstrating multi-modal sensor fusion and cooperative task allocation.

The experimental procedure begins with aerial platforms maintaining standby positions while the terrestrial robot initiates autonomous search for targets exhibiting thermal signatures, like a mannequin dressed in vividly colored dress to make the recognition easier. Upon thermal target acquisition, precise position determination enables coordinated aerial platform engagement.

The second phase of the experiment demonstrates real-time information sharing between heterogeneous platforms and validates cooperative decision-making algorithms under multi-modal sensor conditions.

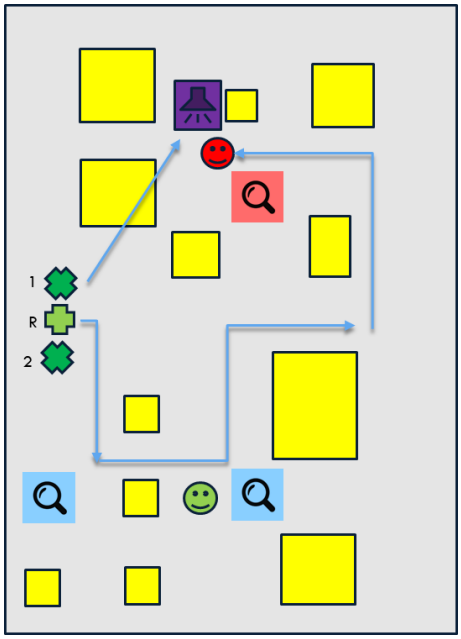

Figure 53. Scenario example of the second phase of the experiment.

8.3.5. Phase 3: Dynamic Target Interception

The final experimental phase (see Figure 54) addresses the most challenging operational scenario through dynamic aerial target interception. This phase validates system adaptability and real-time response capabilities using mobile target insertion scenarios that simulate realistic operational conditions.

The experimental protocol begins with aerial platforms conducting patrol operations over the designated scenario area. The dynamic target, the APR platform, creates unpredictable target engagement conditions that require immediate system response and adaptation.

The interception procedure requires both aerial platforms to autonomously identify and engage the incoming APR target, establishing formation flight and escort protocols. The system demonstrates real-time target tracking, formation maintenance, and escort procedures throughout the APR landing sequence. This phase validates the complete operational capability from initial target detection through final target ground contact.

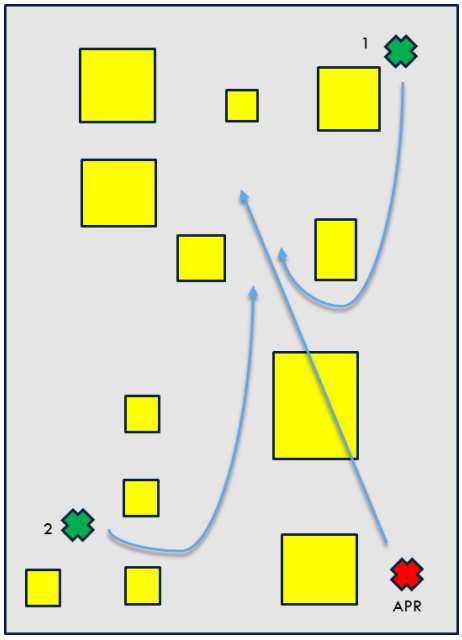

Figure 54. Scenario example of the third phase of the experiment.

8.4. Final Consideration

The S.APR.AI project successfully validated cooperative multi-agent systems for autonomous target detection in semi-structured urban environments. The three-phase experimental protocol demonstrated progressive system capabilities from basic exploration to dynamic target interception, with all thirteen work packages completed within timeline across three institutional partners.

Key achievements include successful integration of electro-optical and infrared sensing across heterogeneous platforms, autonomous library generation algorithms, and real-time cooperative behavior protocols. The system maintained consistent performance under the thirty-minute operational constraint while demonstrating operational readiness through public demonstration.

The methodology establishes a scalable framework for multi-agent system development, with systematic approaches to datalink communication and sensor fusion providing valuable insights for future applications. The successful validation of autonomous target library generation represents a significant advancement for adaptive surveillance systems in dynamic environments.

The progressive complexity approach provides a robust validation framework applicable to future autonomous system projects, effectively balancing technical evaluation with operational readiness assessment for real-world deployment scenarios.

9. Case Study: Surveillance-Dependent Operations in Campi Flegrei Area

This chapter emphasizes the essential role of advanced aerial surveillance in the management of urban infrastructure, particularly in territories exposed to significant natural hazards. It introduces a structured methodology for rapid and extensive building facade inspection, developed through the integration of commercial UAVs and photogrammetric techniques. The contribution is of particular novelty as it represents the first applied case study explicitly framed within the context of surveillance dependence, thereby demonstrating how the reliability of urban risk management increasingly hinges upon the operational performance of such technologies.

The methodology is validated through the structural vulnerability assessment of approximately 10 km of more than 500 building facades situated along critical evacuation routes in the Campi Flegrei bradyseismic area, Italy. Each analysis is conducted within the framework of Italian Low 183/2023 for vulnerability analysis in bradysesmic zones. This application illustrates the scalability and operational efficiency of UAV-based surveillance in densely built environments while also revealing the technical and infrastructural dependencies associated with its deployment.

A central technical challenge addressed in the chapter concerns the degradation of satellite-based navigation signals in complex urban settings, often referred to as “urban canyons.” To this end, a complementary study is presented, focusing on the estimation of UAV positioning errors through the comparison of photogrammetrically derived positions with GNSS telemetry. This analysis provides both methodological guidance and operational insights for enhancing mission planning and risk assessment under GNSS-degraded conditions.

Overall, the chapter contributes to advancing UAV-based methodologies for structural monitoring in hazard-prone urban contexts while simultaneously positioning this first case application as a reference framework for understanding and managing the inherent dependencies of surveillance-based infrastructures.

9.1. Background and Regulatory Framework

The objective is to operate within the framework of the Extraordinary Plan of Vulnerability Assessment of Bradyseismic Areas, focusing on the rapid survey of building facades along evacuation routes through the acquisition of imagery for photogrammetric processing. The aim was established through an agreement between the university Network of University Laboratories of Seismic and Structural Engineering (ReLUIS) and the University of Naples Federico II, through the CeSMA.

In order to establish an efficient and standardized methodology for the rapid survey of building facades, covering a total extension of approximately 10 km, a four-phase workflow was designed (Figure 55):

i. *Mission planning and regulatory framework analysis*.

Preliminary inspection site inspections to assess the morphology of the facades, the surrounding environment, and the presence of potential hazards or obstacles is required. This evaluation enables the definition of a preliminary flight plan for each building. Furthermore, the classification of the operational environment, which comprises urban areas, critical zones, or proximity to airports and sensitive sites, must be carefully considered.. The national platform d-flight serves as the official reference for dynamic airspace maps and regulatory constraints. Risk assessment procedures allow the application of appropriate mitigation strategies, which, in high-risk contexts (e.g., potential aerial conflicts), may include requesting a NOTAM to temporarily restrict airspace. The choice of flight mode is closely tied to the environmental context. Automated flight planning software enables significant time savings but requires adequate separation from obstacles and reduced speed. Conversely, manual operation ensures greater operator responsiveness in handling unexpected events. In both cases, the acquisition strategy must guarantee sufficient image overlap (minimum 80%), with specific attention to the sensor with the narrower field of view when multiple cameras are employed. Ultimately, the selection of drone, payload,

and flight plan must balance safety requirements with the minimum technical standards for reliable façade survey data.

ii. *Mission execution*.

Mission execution is contingent on favorable weather conditions, particularly wind, precipitation, and visibility. Pre-flight checks include laboratory and on-site verifications, encompassing battery status, sensor functionality, and calibration of the inertial measurement unit and compass. During operations, the remote pilot supervises the mission, ensuring obstacle avoidance and, if necessary, mission interruption in case of emergency. Upon completion, data integrity checks are essential to prevent redundant survey missions.

iii. *Data processing and photogrammetric outputs*.

The acquired imagery must be processed using photogrammetric software tailored to infrastructure reconstruction, as distinct from applications designed for mapping or precision agriculture. The outputs generally consist of point clouds, meshes, and georeferenced orthophotos. These datasets are subsequently integrated into a Geographic Information System (GIS) to monitor progress along the surveyed facades and to support the adaptive planning of future operations.

iv. *Data storage and dissemination.*

Given the sensitivity of the processed datasets, storage must rely on secure platforms with traceable user access. The resulting products are made available not only to the institutional units directly involved in the activities but also to the commissioning entity.

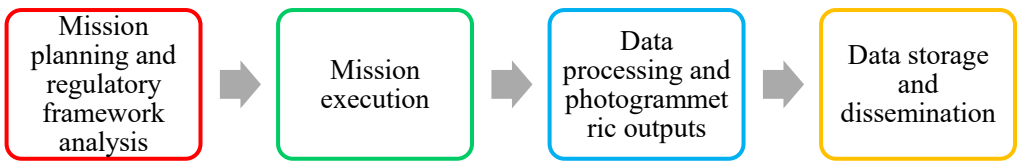

Figure 55. Different phases of process development

9.2. Equipment Configuration

The operational campaign spanned a total of 42 days, encompassing approximately 81 mission hours and 35 actual flight hours. The operations achieved full coverage of the designated target structures, corresponding to a 100% completion rate. The extensive scope and duration of the campaign enabled the collection of a substantial empirical dataset, suitable for methodological validation across diverse urban morphologies.

The survey was conducted using a DJI Mavic 3 Thermal platform [112] shown in Figure 56 equipped with an integrated dual-sensor architecture specifically designed for multi-spectral infrastructure assessment. The RGB system features a 48-megapixel CMOS sensor with a variable aperture (f/2.8–f/11), capable of capturing high-resolution visible-spectrum imagery with enhanced dynamic range. The complementary thermal sensor incorporates a 0.3-megapixel uncooled microbolometer with an 8.7 mm focal length, providing radiometric temperature maps of building facades suitable for the identification of thermal bridges and moisture-related anomalies.

Figure 56. Drone DJI MAVIC 3T and Ground Control Station.

The dual-sensor configuration enabled simultaneous acquisition of geometrically co-registered RGB and thermal datasets, eliminating temporal discrepancies inherent to sequential imaging and maintaining geometric consistency across

spectral domains. This integration facilitated efficient post-processing workflows, ensuring both geometric alignment and radiometric coherence throughout prolonged operational periods.

Mission planning was conducted using UgCS, selected for its capability to generate automated waypoints and configure comprehensive flight parameters or in manual mode. The software optimized flight paths according to the target area geometry, ground sampling distance (GSD), and overlap requirements, while retaining manual override functionality for complex urban environments. The planning workflow incorporated real-time obstacle detection and adaptive path adjustment protocols, enabling seamless transitions between autonomous and manual flight modes. This hybrid approach proved essential in urban settings with dense overhead infrastructure, interference vegetation, and unpredictable pedestrian activity.

Photogrammetric acquisition protocols required a minimum of 80% overlap between consecutive images, with forward and side overlap parameters constrained by the more restrictive field of view of the thermal sensor. This conservative strategy ensured an adequate number of tie points for robust bundle adjustment, maintaining accuracy even in complex morphological contexts. The dual-camera acquisition was synchronized temporally and geometrically, ensuring consistency between datasets. GSD calculations accounted for the specifications of both sensors to ensure sufficient spatial resolution for detailed structural feature identification across both spectral domains.

Flight altitudes were generally maintained at about 25 m above ground level, balancing spatial resolution requirements with urban navigation constraints and GNSS signal availability. Dynamic altitude adjustment protocols ensured consistent GSD across varying terrain elevations while maintaining safe distances from architectural obstacles. Flight mode selection was guided by environmental complexity, with autonomous control prioritized in open areas and manual intervention employed in high-obstacle-density zones. This adaptive strategy optimized operational efficiency while maintaining safety standards.

Overall, the campaign generated approximately 520 GB of UAV-acquired imagery (RGB and thermal), supplemented by an additional 40 GB of tablet-based acquisitions for architectural features requiring specialized access protocols.

The processing of the acquired imagery was aimed at generating the following products for 3D reconstruction of the building façade:

- Point cloud.
- Facade orthophotos.

Several software solutions were evaluated for image processing to obtain these outputs, including Pix4D Mapper, DJI Thermal Analysis Tool, DJI Terra, Zephyr, and Agisoft Metashape. Based on the specific requirements of the missions, Agisoft Metashape was selected as the most suitable software for producing high-quality results. Some examples extracted from the processing are reported below to illustrate the result obtained. In Figure 57-(a) a point cloud of a façade is shown, whereas in (b) the orthophoto.

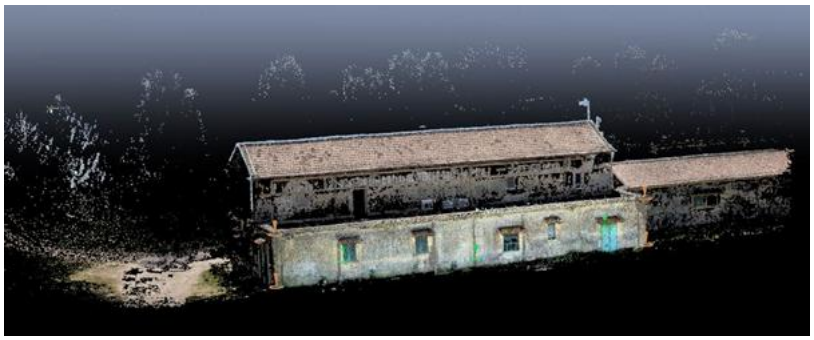

(a)

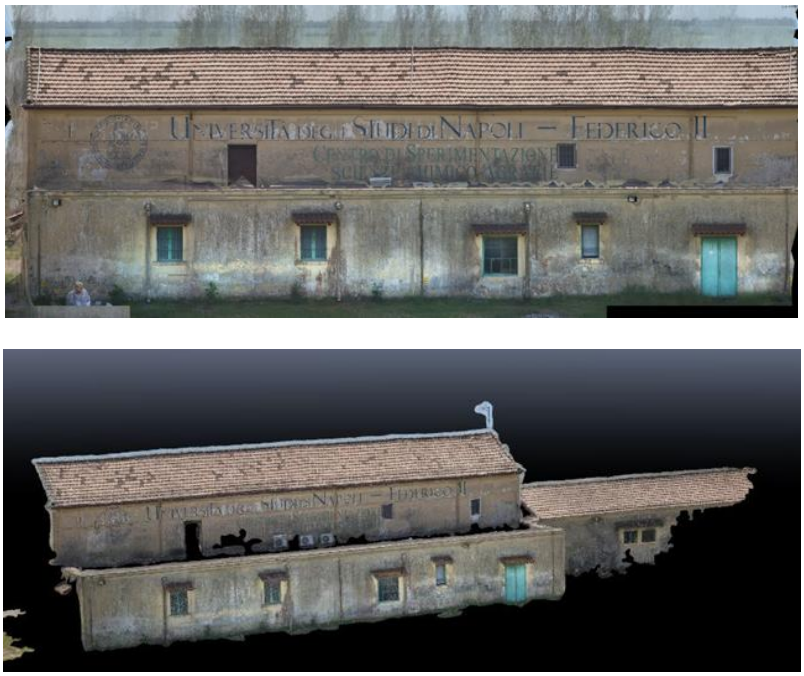

(b)

Figure 57. Example of (a) point cloud of facade (b) orthophoto of the same facade.

9.3. Navigation Challenges in Urban Surveillance Operations

The deployment of UAV-based monitoring systems in densely built urban areas presents a series of critical technical challenges, most notably concerning positioning accuracy and navigation reliability. The Campi Flegrei case study illustrates the extent to which urban canyon effects can undermine the performance

of GNSS-dependent operations, thereby reducing the overall robustness of UAV-assisted infrastructure surveillance.

Throughout the 42-day operational campaign, multiple instances of positioning degradation were documented, particularly during flight operations within narrow streets bordered by multi-storey buildings. These empirical findings are consistent with the theoretical framework outlined in the methodological analysis, which classifies urban environments into nine distinct categories according to building height and street geometry. This correspondence between observed data and the classification system provides further validation of the methodological approach and highlights the necessity of adapting UAV-based survey strategies to the morphological complexity of urban contexts.

9.3.1. GNSS Limitations in Urban Canyon Environments

The so-called urban canyon effect represents one of the most critical challenges for UAV navigation in densely built city environments. Tall and closely spaced buildings obstruct or reflect GNSS signals [113], often resulting in partial signal loss or significant degradation of positioning accuracy. This occurs primarily due to the obstruction of the line-of-sight between the receiver and satellites, which reduces the number of available signals and increases localization errors. In addition, signal reflections from building facades, commonly referred to as the multipath effect [114],further exacerbate positioning inaccuracies. Under such conditions, satellite distribution is typically unfavorable, leading to increased Dilution of Precision (DOP), a fundamental parameter in satellite navigation that quantifies the sensitivity of position estimation accuracy to the geometric configuration of the satellites with respect to the receiver [115].

In recent years, research on autonomous navigation of UASs in urban contexts has gained growing attention. Nonetheless, urban canyon scenarios continue to pose a formidable challenge. Extensive studies have shown that standard GNSS alone is inadequate in these environments, and that integrating GNSS with auxiliary sensors through data fusion techniques can effectively mitigate positioning errors.

For example, the authors in [116] addressed navigation challenges in urban canyons by developing a fuzzy inference system [117]capable of evaluating the reliability of GNSS measurements in real time. The system exploits metadata from GNSS outputs, such as horizontal positioning error estimates, and compares readings from dual GNSS sensors mounted on the UAV. By analyzing discrepancies between expected and actual measurements, unreliable GNSS data can be identified and excluded. Validation was performed using a motion capture system as ground truth reference. The methodology was further enhanced by implementing an adaptive Kalman filter that dynamically adjusted the measurement noise covariance matrix based on the fuzzy system's output [118], thus improving positioning accuracy in GNSS-degraded scenarios.

Other researchers have investigated multi-sensor integration approaches, combining GNSS with IMUs and LiDAR to improve navigation in environments with poor satellite coverage. LiDAR, in particular, enables detailed environmental mapping, allowing correction of errors caused by signal reflection. One study explored tightly coupled GNSS/INS systems and demonstrated that multipath effects and satellite occlusion can be mitigated using adaptive Kalman filters and predictive modeling [119]. Building on this, a tightly coupled architecture integrating GNSS, INS, and LiDAR sensors was proposed, in which the complementary strengths of each system compensate for individual limitations such as GNSS outages or INS drift [120]. Experimental validation in real urban settings confirmed improved positioning accuracy and robustness compared to traditional methods.

Beyond sensor integration, predictive modeling and simulation have also been recognized as essential. Several studies have evaluated satellite visibility in urban environments using three-dimensional building models, showing that flight trajectory planning can be optimized to maintain adequate positioning performance. These methodologies employ geo-referenced 3D models of urban areas to compute available sight distance (ASD) along roadways, integrating data from low-cost mobile mapping systems within GIS and numerical computing environments. Such tools allow the identification of critical areas with poor satellite visibility, enabling

the optimization of UAV flight paths and significantly improving both accuracy and operational safety in dense urban morphologies.

In summary, autonomous UAV navigation in cities requires a combination of advanced hardware, intelligent algorithms, and detailed environmental modeling to overcome the inherent limitations of GNSS in urban canyons. Within this framework, the present study proposes a methodology for estimating UAV positioning errors in standardized urban configurations, enabling the identification of areas where GNSS performance is particularly degraded by morphological constraints. The methodology is validated through an extensive UAV flight campaign, comparing experimental positioning errors recorded during infrastructure inspection missions with the expected performance derived from satellite navigation metrics.

9.3.2. Urban Geometry Classification for Error Analysis

The analysis begins with the classification of urban geometries based on two primary parameters: building height (expressed in terms of the number of floors) and street configuration, defined by the number of sides occupied by buildings. Three building height categories are considered:

i. low-rise structures with up to one floor;

ii. mid-rise structures with up to three floors;

iii. high-rise structures with up to five floors.

Each building is further contextualized within its corresponding street geometry, which can be either unilateral (buildings present on only one side of the street) or bilateral (buildings on both sides of the street). By combining these two parameters, i.e. height class and street configuration, a total of nine standardized urban cases are defined for evaluation.

The identified nine cases are summarized in Table 23. For analytical purposes, the influence of whether the adjacent buildings are positioned on the right or left side

of the street is assumed to be negligible; thus, symmetrical configurations are considered to yield equivalent results.

Table 23. Classification of urban environments considering the number of building floors and the street geometry.

Case ID	**First Street Side**	**Second Street Side**
Case I	Low-rise building	No building
Case II	Low-rise building	Low-rise building
Case III	Low-rise building	Mid-rise building
Case IV	Low-rise building	High-rise building
Case V	Mid-rise building	No building
Case VI	Mid-rise building	Mid-rise building
Case VII	Mid-rise building	High-rise building
Case VIII	High-rise building	No building
Case IX	High-rise building	High-rise building

Following each flight mission, UAV telemetry data were collected in order to reconstruct the executed trajectory in terms of latitude, longitude, and Above Ground Level (AGL) altitude. The acquired imagery was processed using a COTS photogrammetry software, which enabled the generation of key products for infrastructure inspection, namely point clouds, meshes, and orthophotos. During processing, the software utilized image metadata to assign initial calibrated camera positions, and through an iterative image-matching procedure, refined these positions within a local reference frame. In this framework, the geographical coordinates embedded in the image metadata were assumed to correspond to the UAV center of mass position. By imposing a maximum deviation threshold of 10 m for each positional coordinate, the discrepancy between the initial georeferenced

camera positions and the refined positions estimated by the photogrammetric workflow could be quantified.

In parallel, telemetry logs provided acquisition timestamps, which were subsequently employed to retrieve satellite ephemeris data from open-access repositories. A dedicated GNSS simulation tool was developed in the Matlab™ environment, incorporating satellite orbital parameters specific to each flight mission. The simulator enabled the reconstruction of satellite constellations, allowing for the analysis of Line of Sight (LOS) visibility between satellites and the UAV, taking into account the constraining effects of the surrounding urban geometry. Within this framework, DOP values were estimated at varying flight altitudes for each mission.

The simulated DOP metrics were then compared against the positioning errors derived from photogrammetric processing, enabling a systematic assessment of the impact of urban morphological characteristics on GNSS performance. This comparative analysis allowed the derivation of correlations between urban environment typologies, DOP estimations, and positioning errors.

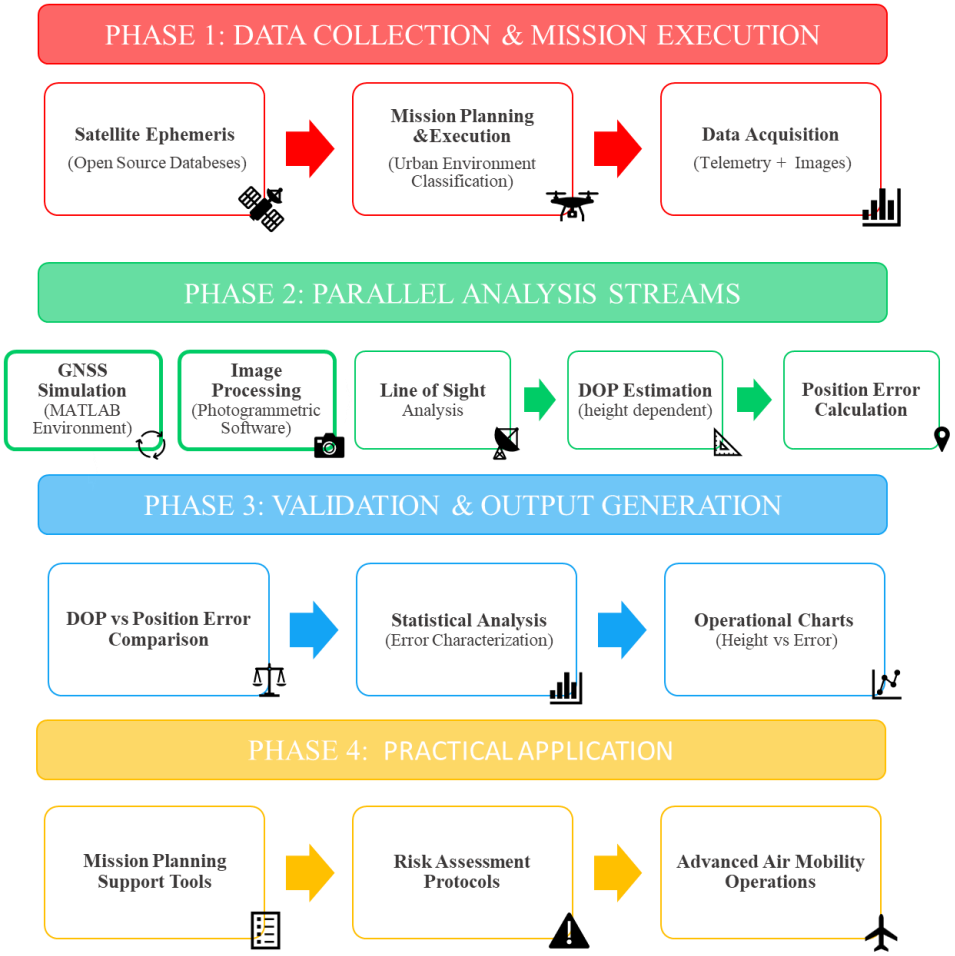

Figure 58. Flow chart of the applied methodology.

9.4. Case Study Analysis: Positioning Accuracy in Case VIII Urban Configuration

The first analyzed case study corresponds to a UAV mission executed within a Case VIII urban configuration, defined as a four-story building located along a wide street with structures present only on one side. During this mission, approximately 100 RGB images were acquired at an automatic acquisition rate of one image every 2 seconds, with a total flight duration of about 4 minutes. The acquired imagery was processed in Agisoft Metashape to generate a three-dimensional reconstruction of the target building. The urban scenario was imported into the simulator using OpenStreetMap data, with the drone trajectory represented by a blue line and the surrounding buildings visualized as orange polygons (Figure 59).

Figure 59. Urban Environment in Case VIII scenario.

The preliminary analysis focused on the GPS constellation, specifically evaluating LOS visibility of 31 satellites within the urban environment. This evaluation was conducted using the Matlab™ Communication Toolbox™ and Antenna Toolbox™. Once the visible satellites were identified for the mission, pseudoranges were computed through the Matlab™ Navigation Toolbox, enabling the estimation of the Horizontal Dilution of Precision (HDOP) values corresponding to the given urban geometry. Variations in HDOP were analyzed at different AGL flight altitudes, and results indicated that HDOP remained nearly constant throughout the mission (Figure 60).

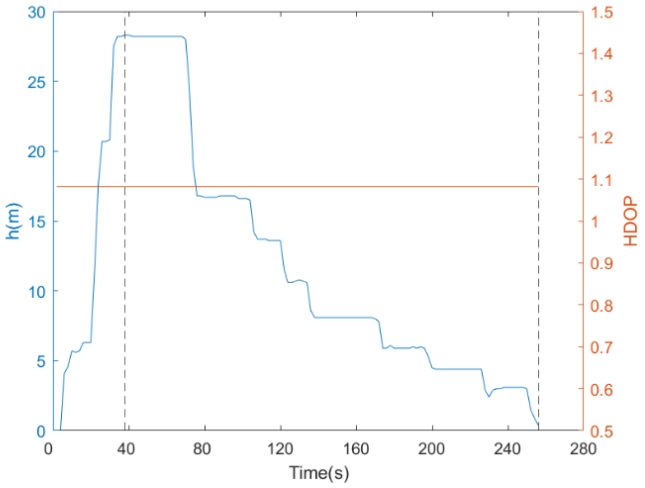

Figure 60. Comparison of HDOP value at different flight height levels.

The photogrammetry software was further employed to estimate the UAV positioning error based on image processing during the 3D reconstruction workflow. Error estimates were only available at acquisition times, i.e., when the UAV had reached its designated altitude and images were captured at the fixed 2-second interval. Figure 61 illustrates the comparison between computed positioning errors in the local reference frame and the variation in flight altitude, with results displayed for the x-axis (Figure 61-a) and y-axis (Figure 61-b). Outside the interval bounded by vertical dashed lines, the error values were initialized to zero due to the absence of image acquisitions.

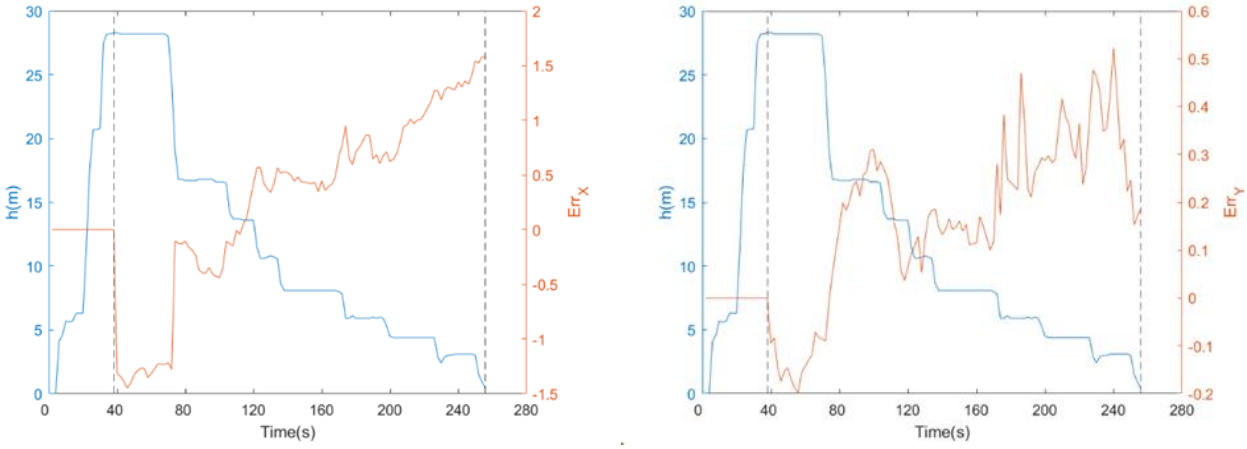

(a) (b)

Figure 61. Comparison between the positioning error in the local reference frame and the flight altitude variation: (a) analysis of the X-axis error component; (b) analysis of the Y-axis error component.

The results indicate the presence of nearly constant error peaks during the initial phase of the mission, followed by a progressive increase in error magnitude during the descending flight segment. This behavior is consistent with the expected impact of building-induced interference in urban canyon environments, where GNSS signal degradation becomes more pronounced at lower altitudes.

In conclusion, the Campi Flegrei case study highlights the critical interdependence between UAV-based infrastructure monitoring and broader surveillance strategies. The operational challenges encountered, particularly GNSS signal degradation in urban canyon environments, highlight the necessity of integrating advanced sensing, photogrammetric, and data-fusion techniques to maintain accurate situational awareness. These findings not only validate the methodological framework employed but also demonstrate that effective urban risk management increasingly relies on the seamless interplay between aerial surveillance technologies and continuous monitoring systems. By bridging structural assessment with real-time data acquisition, this study positions UAV-enabled inspections as a cornerstone for surveillance-dependent operations in hazard-prone urban contexts.

10. Conclusion

This work face the complex challenges associated with enabling safe, efficient, and sustainable UAM and AAM operation, with particular focus on the validation of innovative edge solution. Originally developed for military applications, drones have evolved into versatile platforms deeply integrated within civil, industrial, and societal frameworks, generating unpresented challenges in safety assurance, security protocols, and surveillance infrastructures, architecturally designed for high-altitude and low-density air traffic operations, prove inadequate for the dense, low-altitude operational paradigms anticipated in future urban environment. This paradigmatic shift necessitates the development of innovative, adaptive, and edge-capable surveillance solutions that ensure resilient and sustainable integration of heterogeneous manned and unmanned traffic flows.

Through a combination of theoretical modeling, simulation studies, and experimental campaigns, this research has contributed to both scientific understanding of drone detectability and the practical development of multi-sensor architectures.

The analysis of RCS behavior, encompassing both simulated platforms and real-world UAV measurements, had highlighted the intrinsic limitations of traditional surveillance radars when applied to aircrafts typically almost invisible to the radar such as stealth aircrafts and small UAVs. The exploration of passive and active enhancement techniques, complemented by cooperative multi-agent detection frameworks, demonstrated the feasibility of improving target visibility and resilience in semi-structured urban environments. Moreover, the integration of radar and acoustic sensors in a simulation environment provided evidence of the advantages of hybrid architectures for reducing detection uncertainty.

Beyond purely technical contributions, the dissertation underscored the importance of linking aerospace research with socio-economic innovation. The “Pathways to Innovation and Entrepreneurship” program and the applied case study in the Irpinia DOCG region revealed how UAV technologies, when embedded in broader

innovation ecosystems, can foster territorial development, Strengthen industry-academia collaborations, and promote sustainable practices. The case study on UAV-base monitoring in Campi Flegrei bradyseism area further illustrated the dual role of drone surveillance: as a technological enabler of safety-critical operations and as a regulatory challenge requiring new frameworks for risk management.

Taken together, the findings provide a comprehensive contribution to the advancement of surveillance strategies for AAM. They validate the necessity of multi-layered, cooperative, and edge-enabled approaches, while also demonstrating that technological innovation must be complemented by regulatory foresight and socioeconomic integration.

To summarize, the main findings highlight:

- *Radar cross-section constraints* represent a fundamental limitation for UAV detection, necessitating novel architectures and hybrid sensing approaches.
- *Simulation and experimental validation* confirmed the value of integrating radar and acoustic sensors, as well as cooperative multi-agent systems, to reduce uncertainty in complex urban scenarios.
- *RCS enhancement strategies*, both passive and active, were shown to increase target visibility and provide practical insights into system design trade-offs.
- *Socio-economic perspectives* revealed that surveillance innovation can extend beyond aerospace, fostering territorial development, entrepreneurship, and sustainability when embedded in broader innovation ecosystems.
- *Applied case studies*, including the cooperative multi-agent system for autonomous detection in semi-structured urban environments, and surveillance-dependent operations in the Campi Flegrei volcanic are, demonstrated the dual potential of drone-based surveillance as both a technological enabler and a regulatory challenge across several high-impact domains.

Bibliography

[1] Gundlach, J., and Schetz, J. A., “Designing Unmanned Aircraft Systems A Comprehensive Approach Second Edition AIAA EDUCATION SERIES.”

[2] Grubesic, T. H., Nelson, J. R., and Wei, R., “UAVs for Spatial Modelling and Urban Informatics.”

[3] Nonami, K., “Overview of the Global Drone Industry,” 2025. https://doi.org/10.1109/ICM62621.2025.10934845

[4] Seidaliyeva, U., Ilipbayeva, L., Taissariyeva, K., Smailov, N., and Matson, E. T., “Advances and Challenges in Drone Detection and Classification Techniques: A State-of-the-Art Review,” 2023. https://doi.org/10.3390/s24010125

[5] Tania, L., “Civil and Military Drones. Navigating a Disruptive and Dynamic Ecosystem,” October 2019.

[6] Dalamagkidis, K., “Classification of UAVs,” *Handbook of Unmanned Aerial Vehicles*, Springer Netherlands, Dordrecht, 2015, pp. 83–91. https://doi.org/10.1007/978-90-481-9707-1_94

[7] “Unmanned Aerial Traffic Management System Architecture for U-Space In-Flight Services | Enhanced Reader.” Retrieved 25 September 2025

[8] “REGOLAMENTO DI ESECUZIONE (UE) 2019/ 947 DELLA COMMISSIONE - Del 24 Maggio 2019 - Relativo a Norme e Procedure per l’esercizio Di Aeromobili Senza Equipaggio,” 2019.

[9] “REGOLAMENTO DELEGATO (UE) 2019/ 945 DELLA COMMISSIONE - Del 12 Marzo 2019 - Relativo Ai Sistemi Aeromobili Senza Equipaggio e Agli Op eratori Di Paesi Terzi Di Sistemi Aeromobili Senza Equipaggio,” 2019.

[10] Easa, “Easy Access Rules for Unmanned Aircraft Systems — Revision from September 2022,” 2022.

[11] “COMMISSION IMPLEMENTING REGULATION (EU) 2021/664 of 22 April 2021 on a Regulatory Framework for the U-Space (Text with EEA Relevance).”

[12] “COMMISSION IMPLEMENTING REGULATION (EU) 2021/666 of 22 April 2021 on a Regulatory Framework for the U-Space (Text with EEA Relevance).”

[13] “COMMISSION IMPLEMENTING REGULATION (EU) 2021/665 of 22 April 2021 on a Regulatory Framework for the U-Space (Text with EEA Relevance).”

[14] “CORUS-XUAM - Concept of Operations for European U-Space Services - Extension for Urban Air Mobility | SESAR Joint Undertaking.”

[15] “AURA - ATM U-Space Interface | SESAR Joint Undertaking.” Retrieved 19 September 2023. https://www.sesarju.eu/projects/aura

[16] “AMU-LED - Air Mobility Urban - Large Experimental Demonstrations | SESAR Joint Undertaking.” Retrieved 19 September 2023. https://www.sesarju.eu/projects/AMU-LED

[17] “GOF2.0 - Integrated Urban Airspace VLD | SESAR Joint Undertaking.” Retrieved 19 September 2023. https://www.sesarju.eu/projects/GOF2

[18] “Uspace4UAM | SESAR Joint Undertaking.” Retrieved 19 September 2023. https://www.sesarju.eu/projects/Uspace4UAM

[19] “EUREKA | Sesar Joint Undertaking.” Retrieved 16 September 2025. https://project-eureka.eu/

[20] “OperA | Sesar Joint Undertaking.” Retrieved 16 September 2025. https://project-opera.eu/

[21] “ENSURE Project| SESAR Joint Undertaking.” www.sesarju.eu/projects/ensure

[22] “SPATIO | Sesar Joint Undertaking.” Retrieved 16 September 2025. https://research.dblue.it/spatio/

[23] “SAFIR-Ready | SESAR Joint Undertaking.” Retrieved 16 September 2025. https://safir-ready.eu/

[24] “ImAFUSA | SESAR Joint Undertaking.” Retrieved 16 September 2025. https://www.imafusa-sesar.eu/

[25] “LTAG Report | International Civil Aviation Organization.” Retrieved 16 September 2025. https://www.icao.int/environmental-protection/

[26] “Artificial Intelligence Roadmap 2.0 | European Union Aviation Safety Agency.” Retrieved 16 September 2025. https://www.easa.europa.eu/en/newsroom-and-events/news/easa-artificial-intelligence-roadmap-20-published

[27] “Trajectory Based Operations (TBO) | Federal Aviation Administration.” Retrieved 16 September 2025. https://www.faa.gov/air_traffic/technology/tbo

[28] “Sustainable ATM | SESAR Joint Undertaking.” Retrieved 16 September 2025. https://www.sesarju.eu/sustainability

[29] Gillani, R., Jahan, S., and Majid, I., “A Proposed Communication, Navigation & Surveillance System Architecture to Support Urban Air Traffic Management,” Vols. 2021-October, 2021. https://doi.org/10.1109/DASC52595.2021.9594379

[30] Namuduri, K., Fiebig, U. C., Matolak, D. W., Guvenc, I., Hari, K. V. S., and Maattanen, H. L., “Advanced Air Mobility: Research Directions for Communications, Navigation, and Surveillance,” *IEEE Vehicular Technology Magazine*, Vol. 17, No. 4, 2022, pp. 65–73. https://doi.org/10.1109/MVT.2022.3194277

[31] Ponchak, D. S., Templin, F. L., Sheffield, G., Taboso, P., and Jain, R., “Advancing the Standards for Unmanned Air System Communications, Navigation and Surveillance; Advancing the Standards for Unmanned Air System Communications, Navigation and Surveillance,” 2019.

[32] Stouffer, V. L., Cotton, W. B., Deangelis, R. A., Devasirvatham, D. M., Irvine, T. B., Jennings, R. E., Lehmer, R. D., Nguyen, T. C., and Shaver, M., “Reliable, Secure, and Scalable Communications, Navigation, and Surveillance (CNS) Options for Urban Air Mobility (UAM),” 2020.

[33] “Pathways to Innovation and Entrepreneurship.” Retrieved 16 September 2025. https://www.pathwaystoinnovationentrepreneurship.eu/

[34] Mattei, F., Pallotta, L., Accardo, D., and De Maio, A., “RCS of a F-35 Stealth Aircraft: Statistical Analyses of a POFACETS Model.”

[35] Mattei, F., Accardo, D., and De Maio, A., “POFACETS Simulated RCS Data From an F-35 Aircraft Model and Their Statistical Analysis,” 2025.

[36] Zikidis, K., Skondras, A., Lt, H., and Tokas, C., “Low Observable Principles, Stealth Aircraft and Anti-Stealth Technologies,” Scienpress Ltd, 2014.

[37] Ahmad, H., Tariq, A., Shehzad, A., Faheem, M. S., Shafiq, M., Rashid, I. A., Afzal, A., Munir, A., Riaz, M. T., Haider, H. T., Afzal, A., Qadir, M. B., and Khaliq, Z., "Stealth Technology: Methods and Composite Materials—A Review," *Polymer Composites*, Vol. 40, No. 12, 2019, pp. 4457–4472. https://doi.org/10.1002/pc.25311

[38] Chatzigeorgiadis, "Calhoun: The NPS Institutional Archive DSpace Repository Development of Code for a Physical Optics Radar Cross Section Prediction and Analysis Application," 2006.

[39] Martin, L., "F-35 Lightning II," 2024. Retrieved 11 August 2025. https://www.f35.com/f35/index.html

[40] Kopp, C., "Assessing Joint Strike Fighter Defence Penetration Capabilities Annex A, B, C," 2014. Retrieved 11 August 2025. Assessing Joint Strike Fighter Defence Penetration Capabilities Annex A, B, C,

[41] Touzopoulos, P., Boviatsis, D., and Zikidis, K., "Constructing a 3D Model of a Complex Object from 2D Images, for the Purpose of Estimating Its Radar Cross Section (RCS)," Vol. Vol. 7, 2017, pp. 15–28.

[42] Herda, D. L. , Suryana, J. , and Izzuddin, A. , "Radar Cross Section of F35: Simulation and Measurement," 2020.

[43] Chung, S. M., Chou, Y., and Chuang, Y., "Radar Cross Section Analysis of Stealth Fighter Design: Key Factors and Limitations of Simulation," *International Journal of Electrical Engineering*, Vol. 23, 2016, pp. 201–214.

[44] Mark A. Richards, James A. Scheer, and William A. Holm, "Principles of Modern Radar."

[45] Conte, E., and Maio, A. De, "Statistical Analysis of Real Clutter at Different Range Resolutions."

[46] Rosamilia, M., Aubry, A., Balleri, A., Carotenuto, V., and De Maio, A., "RCS Measurements of UAVs and Their Statistical Analysis." https://doi.org/10.1109/MetroAeroSpace54187.2022.9856394

[47] Forbes, C., Evans, M., Hastings, N., and Peacock, B., "Statistical Distributions," 2011.

[48] D'Agostino, R. B., and Stephens, M. A., "Goodness of Fit Techniques," 1986.

[49] Bahret, W. F., “The Beginnings of Stealth Technology,” *IEEE Transactions on Aerospace and Electronic Systems*, Vol. 29, No. 4, 1993, pp. 1377–1385. https://doi.org/10.1109/7.259548

[50] Xue, M., “Urban Air Mobility Conflict Resolution: Centralized or Decentralized?”

[51] Spalas, K., “Towards the Unmanned Aerial Vehicle Traffic Management Systems (UTMs): Security Risks and Challenges,” 2024.

[52] Dan SImon, “Optimal State Estimation,” New Jersey, 2006.

[53] Hoekstra, J. ;, and Ellerbroek, J., “BlueSky ATC Simulator Project: An Open Data and Open Source Approach,” APA, 2016.

[54] “Operation and Maintenance Manual.”

[55] Seeed Studio, “ReSpeaker Mic Array 2.0 .” Retrieved 21 August 2025. https://wiki.seeedstudio.com/ReSpeaker_Mic_Array_v2.0/

[56] “MAVIC 2 ENTERPRISE SERIE,” 2020.

[57] Marmaroli, P., Falourd, X., and Lissek, H., “A Comparative Study of Time Delay Estimation Techniques for Road Vehicle Tracking,” 2012.

[58] Clemente, C., Fioranelli, F., Colone, F., and Li, G., “Clemente, Carmine, et al. Radar Countermeasures for Unmanned Aerial Vehicles,” *Institution of Engineering and Technology, 2021*, 2021.

[59] Wang, J., Liu, Y., and Song, H., “Counter-Unmanned Aircraft System(s) (C-UAS): State of the Art, Challenges, and Future Trends,” *IEEE Aerospace and Electronic Systems Magazine*, Vol. 36, No. 3, 2021, pp. 4–29. https://doi.org/10.1109/MAES.2020.3015537

[60] “Detection, Tracking, and Interdiction for Amateur Drones.”

[61] Yang, T., De Maio, A., Zheng, J., Su, T., Carotenuto, V., and Aubry, A., “An Adaptive Radar Signal Processor for UAVs Detection with Super-Resolution Capabilities,” *IEEE Sensors Journal*, Vol. 21, No. 18, 2021, pp. 20778–20787. https://doi.org/10.1109/JSEN.2021.3093779

[62] Rosamilia, M., Aubry, A., Balleri, A., Carotenuto, V., and De Maio, A., “Radar Detection Performance via Frequency Agility Using Measured UAVs RCS Data,”

IEEE Sensors Journal, Vol. 23, No. 19, 2023, pp. 23011–23019. https://doi.org/10.1109/JSEN.2023.3306032

[63] Rosamilia, M., Balleri, A., De Maio, A., Aubry, A., and Carotenuto, V., "Radar Detection Performance Prediction Using Measured UAVs RCS Data," *IEEE Transactions on Aerospace and Electronic Systems*, Vol. 59, No. 4, 2023, pp. 3550–3565. https://doi.org/10.1109/TAES.2022.3227224

[64] Patel, J. S., Fioranelli, F., and Anderson, D., "Review of Radar Classification and RCS Characterisation Techniques for Small UAVs or Drones," *IET Radar, Sonar and Navigation*, Vol. 12, No. 9, 2018, pp. 911–919. https://doi.org/10.1049/IET-RSN.2018.0020

[65] Li, C. J., and Ling, H., "An Investigation on the Radar Signatures of Small Consumer Drones," *IEEE ANTENNAS AND WIRELESS PROPAGATION LETTERS*, Vol. 16, 2017. https://doi.org/10.1109/LAWP.2016.2594766

[66] Ezuma, M., Kumar Anjinappa, C., Funderburk, M., and Guvenc, I., "Radar Cross Section Based Statistical Recognition of UAVs at Microwave Frequencies," 2021.

[67] Semkin, V., Haarla, J., Pairon, T., Slezak, C., Rangan, S., Viikari, V., and Oestges, C., "Analyzing Radar Cross Section Signatures of Diverse Drone Models at MmWave Frequencies," *IEEE Access*, Vol. 8, 2020, pp. 48958–48969. https://doi.org/10.1109/ACCESS.2020.2979339

[68] To, L., Bati, A., and Hilliard, D., "Radar Cross Section Measurements of Small Unmanned Air Vehicle Systems in Non-Cooperative Field Environments."

[69] Ochodnický, J., Matoušek, Z., Babjak, M., and Kurty, J., "Drone Detection by Ku-Band Battlefield Radar." Retrieved 1 September 2025

[70] Balleri, A., "Measurements of the Radar Cross Section of a Nano-Drone at K-Band." https://doi.org/10.1109/METROAEROSPACE51421.2021.9511750

[71] Ritchie, M., Fioranelli, F., Griffiths, H., and Torvik, B., "Micro-Drone RCS Analysis," *2015 IEEE Radar Conference - Proceedings*, 2015, pp. 452–456. https://doi.org/10.1109/RADARCONF.2015.7411926

[72] Sedivy, P., and Nemec, O., "Drone RCS Statistical Behaviour."

[73] Speirs, P. J., Murk, A., Renker, M., Wellig, P., Thun, W., and Aulenbacher, S. U., “High-Detail Simulations of Consumer-Grade UAV RCS Signatures, and Comparisons against Measurements.”

[74] Ardoino Elettronica SpA, R., Flagiello, N., Russo, S., Di Gregorio, L., Bagnato, R., and Rossi, V., “Commercial Drones Radar Cross Section Characterisation at 24 GHz with a Frequency Modulated Continuous Wave Radar.”

[75] Franzese, M., Carotenuto, V., Mattei, F., Conte, C., Rufino, G., Accardo, D., Berardino, P., Di Vincenzo, A., Esposito, C., Natale, A., Palmese, G., Perna, S., Lanari, R., and De Maio, A., “In-Flight UAVs Polarimetric Radar Cross-Section Measurement and Statistical Analysis at X- and L-Bands,” *IEEE Sensors Journal*, 2025. https://doi.org/10.1109/JSEN.2025.3598584

[76] Franzese, M., Carotenuto, V., Mattei, F., Conte, C., Rufino, G., Accardo, D., De Luca, C., Berardino, P., Di, A., †‖ V., Esposito, C., Natale, A., Palmese, G., Perna, S., Lanari, R., and De Maio, A., “Radar Cross-Section Analysis of In-Flight UAVs in X-and L-Band.”

[77] “User Manual MATRICE 300 RTK 2 Using This Manual Legends Warning Important Hints and Tips Reference Before Flight,” 2020.

[78] Mattei, F., Carotenuto, V., Conte, C., Rufino, G., Accardo, D., Di Vincenzo, A., Esposito, C., Natale, A., Berardino, P., Palmese, G., Perna, S., Lanari, R., and De Maio, A., “Exploring the RCS of In-Flight UAVs.”

[79] Esposito, C., Natale, A., Lanari, R., Berardino, P., and Perna, S., “On the Capabilities of the IREA-CNR Airborne SAR Infrastructure,” *Remote Sensing*, Vol. 16, No. 19, 2024. https://doi.org/10.3390/rs16193704

[80] Natale, A., Berardino, P., Esposito, C., Palmese, G., Lanari, R., and Perna, S., “THE NEW ITALIAN AIRBORNE MULTIBAND INTERFEROMETRIC AND POLARIMETRIC SAR (MIPS) SYSTEM: FIRST FLIGHT TEST RESULTS.” https://doi.org/10.1109/IGARSS46834.2022.9884189

[81] Esposito, C., Natale, A., Palmese, G., Berardino, P., Lanari, R., and Perna, S., “On the Capabilities of the Italian Airborne FMCW AXIS InSAR System.” https://doi.org/10.3390/rs12030539

[82] Markow, J., Balleri, A., and Catherall, A., “Statistical Analysis of In-Flight Drone Signatures,” 2022. https://doi.org/10.1049/rsn2.12293

[83] Drozdowicz, J., Wielgo, M., Samczynski, P., Kulpa, K., Krzonkalla, J., Mordzonek, M., Bryl, M., and Jakielaszek, Z., "35 GHz FMCW Drone Detection System."

[84] Klare, J., and Fhr, F., "Detection of UAVs Using the MIMO Radar MIRA-CLE Ka."

[85] Duque De Quevedo, Á., Ibañez Urzaiz, F., Menoyo, J. G., and Asensio López, A., "Drone Detection and Radar-Cross-Section Measurements by RAD-DAR," 2019. https://doi.org/10.1049/iet-rsn.2018.5646

[86] Hoffmann, F., Ritchie, M., Fioranelli, F., Charlish, A., and Griffiths, H., "Micro-Doppler Based Detection and Tracking of UAVs with Multistatic Radar," *2016 IEEE Radar Conference, RadarConf 2016*, 2016. https://doi.org/10.1109/RADAR.2016.7485236

[87] Park, S., and Park, S. O., "Configuration of an X-Band FMCW Radar Targeted for Drone Detection," *2017 International Symposium on Antennas and Propagation, ISAP 2017*, Vols. 2017-January, 2017, pp. 1–2. https://doi.org/10.1109/ISANP.2017.8228912

[88] Caris, M., Johannes, W., Sieger, S., Port, V., and Stanko, S., "Detection of Small UAS with W-Band Radar," *Proceedings International Radar Symposium*, 2017. https://doi.org/10.23919/IRS.2017.8008143

[89] Rahman, S., and Robertson, D. A., "In-Flight RCS Measurements of Drones and Birds at K-Band and W-Band," *IET Radar, Sonar & Navigation*, Vol. 13, No. 2, 2019, pp. 300–309. https://doi.org/10.1049/IET-RSN.2018.5122

[90] Hao, W., Chen, G., Li, Y., and Hou, Y., "Analysis of RCS Characteristics in Dynamic Flight of Stealth UAV." https://doi.org/10.1109/ICETCI57876.2023.10176877

[91] Persson, Björn., "Radar Target Modeling Using In-Flight Radar Cross-Section Measurements," *Journal of Aircraft, 54(1)*, 2017.

[92] Rao, S., and Instruments, T., "Introduction to Mmwave Sensing: FMCW Radars."

[93] Melvin, W. L., and Scheer, J. A., "Principles of Modern Radar: Volume 3: Radar Applications," 2013.

[94] Mattei, F., De Alteriis, G., Conte, C., Mele, A., Carotenuto, V., Rufino, G., De Maio, A., and Accardo, D., “Improving Radar Detection of Drones and Air Mobility Systems in Urban Areas.”

[95] Manual, U., “MATRICE 600 PRO,” 2017. Retrieved 7 February 2023. http://www.dji.com/matrice600-pro/info#downloads

[96] “IEEE Guide for Developing System Requirements Specifications,” 1996. https://doi.org/10.1109/IEEESTD.1996.81000

[97] Great Scott Gadgets, “HackRF,” 2023. Retrieved 7 February 2023

[98] Rev, “SDR SYSTEM EVALUATION KIT USER MANUAL.” Retrieved 7 February 2023. www.ancortek.com.

[99] “GNU Radio Manual and C++ API Reference: Main Page.” Retrieved 8 February 2023. https://www.gnuradio.org/doc/doxygen/

[100] Hill, M. M., “Developing a Generic Software-Defined Radar Transmitter Using GNU Radio.,” 2012. Retrieved 8 February 2023. https://digital.library.adelaide.edu.au/dspace/handle/2440/77826

[101] Santos, D., Sebastiao, P., and Souto, N., “Low-Cost SDR Based FMCW Radar for UAV Localization,” *International Symposium on Wireless Personal Multimedia Communications, WPMC*, Vols. 2019-November, 2019. https://doi.org/10.1109/WPMC48795.2019.9096117

[102] RF Wireless World, “What Are the Advantages of Software Defined Radio?,” 2002. Retrieved 7 February 2023

[103] “IEEE Xplore Full-Text PDF:” Retrieved 14 June 2023. https://ieeexplore.ieee.org/stamp/stamp.jsp?tp=&arnumber=9849444

[104] “RF Wireless Vendors and Resources | RF Wireless World.” Retrieved 7 February 2023. https://www.rfwireless-world.com/

[105] Skorobogatov, G., Barrado, C., and Salamí, E., “Multiple UAV Systems: A Survey,” *Unmanned Systems*, Vol. 8, No. 2, 2020, pp. 149–169. https://doi.org/10.1142/S2301385020500090

[106] Zieliński, T., “Factors Determining a Drone Swarm Employment in Military Operations.” https://doi.org/10.37105/sd.112

[107] Shang, B., Shafin, R., and Liu, L., “UAV Swarm-Enabled Aerial Reconfigurable Intelligent Surface,” 2021. http://arxiv.org/abs/2103.06361

[108] Conte, C., Supplizi, S. V., de Alteriis, G., Mele, A., Rufino, G., and Accardo, D., “Using Drone Swarms as a Countermeasure of Radar Detection,” *Journal of Aerospace Information Systems*, Vol. 20, No. 2, 2023, pp. 70–80. https://doi.org/10.2514/1.I011131

[109] Hayat Adnan, W., and Fadly Khamis, M., “Drone Use in Military and Civilian Application: Risk to National Security,” 2022.

[110] Stereolabs, “ZED 2i Datasheet,” 2022.

[111] Optris, “PI 640i Datasheet,” 2021.

[112] “Mavic 3 Thermal D R O N E S &Technologies Pvt.Ltd.”

[113] Humphreys, T. E., Murrian, M. J., and Narula, L., “Deep-Urban Unaided Precise Global Navigation Satellite System Vehicle Positioning,” *IEEE Intelligent Transportation Systems Magazine*, Vol. 12, No. 3, 2020, pp. 109–122. https://doi.org/10.1109/MITS.2020.2994121

[114] Egea-Roca, D., Arizabaleta-Diez, M., Pany, T., Antreich, F., Lopez-Salcedo, J. A., Paonni, M., and Seco-Granados, G., “GNSS User Technology: State-of-the-Art and Future Trends,” *IEEE Access*, Vol. 10, 2022, pp. 39939–39968. https://doi.org/10.1109/ACCESS.2022.3165594

[115] Isik, O. K., Hong, J., Petrunin, I., and Tsourdos, A., “Integrity Analysis for GPS-Based Navigation of UAVs in Urban Environment,” *Robotics*, Vol. 9, No. 3, 2020. https://doi.org/10.3390/ROBOTICS9030066

[116] Wessels, A., and Cohen, K., “Urban Canyon Localization, Testing, and Validation,” 2023. https://doi.org/10.2514/6.2023-72396

[117] D, S. A., Ramalingam, M., and Anuradha, B., “A Comprehensive Study on Fuzzy Inference System and Its Application in the Field of Engineering,” *International Journal of Engineering Trends and Technology*, Vol. 54, 2017. http://www.ijettjournal.org

[118] Wessels, A. M., “Fuzzy Inference System to Detect GPS Health in the Urban Environment,” 2023.

[119] Zhang, S., Tu, R., Gao, Z., Zou, D., Wang, S., and Lu, X., “LEO-Enhanced GNSS/INS Tightly Coupled Integration Based on Factor Graph Optimization in the Urban Environment,” *Remote Sensing*, Vol. 16, No. 10, 2024. https://doi.org/10.3390/rs16101782

[120] Budiyono, A., “Principles of GNSS, Inertial, and Multi-Sensor Integrated Navigation Systems,” *Industrial Robot: An International Journal*, Vol. 39, No. 3, 2012, p. ir.2012.04939caa.011. https://doi.org/10.1108/ir.2012.04939caa.011

Glossary of Acronyms

AAM
: Advanced Air Mobility; 17

ADC
: Analog-to-Digital Converter; 106; 150

AGL
: Above Ground Level; 177

AI
: Artificial Intelligence; 26

ASD
: Available Sight Distance; 175

ATC
: Air Traffic Control; 71

ATM
: Air Traffic Management; 78

CAD
: Computer Aided Design; 53

CAGR
: Computational Annual Growth Rate; 17

CDF
: Cumulative Distribution Function; 59

CNR
: National Italian Research Council; 107

CNS
: Communication, Navigation, Surveillance; 18

COTS
: Commercial-Off-The-Shelft; 110

CUAS
: Counter-Unmanned Aircraft Systems; 156

CVM
: Cramér-von Mises; 49

DAQ
: a Data Acquisition System; 146

DOA
: Direction of Arrival; 80

DOP
: Dilution of Precision; 174

DSP
: Digital Signal Processor; 150

EASA
European Union Aviation Safety Agency; 23
ECDF
Empirical Cumulative Distribution Function; 59
ECEF
Earth-Centered Earth-Fixed; 96
EKF
Extended Kalman Filter; 75
EM
Electromagnetic; 18
ENU
East-North-Up; 96
EO
Electro-Optical; 157
FEC
forward error correction; 150
FFT
Fast Fourier Transform; 96
FIMS
Flight Information Management System; 134
FMCW
Frequency-Modulated Continuous-Wave; 101
FPGA
Field-Programmable Gate Array; 150
GCC-PHAT
PHAT weighting Cross Correlation Algorithm; 96
GCS
Ground Control System; 134
GIS
Geographic Information System; 169
GN&C
Guidance, Navigation & Control; 26
GPP
General-Purpose Processor; 150
GUI
Graphical User Interface; 78
HDOP
Horizontal Diluition of Precision; 180
IC
Integrated Circuit; 80
IEEE

Institute of Electrical and Institute of Elecetricalo and Electronics Engineering; 32

IF

Intermediate Frequency; 106

IMU

Inertial Measurement Unit; 133

IoT

Internet of Things; 17

IQR

Interquartile Range; 115

IR

Infrared; 49

IREA

Electromagnetic Sensing of the Environment; 107

KF

Kalman Filter; 75

LOS

Line-of-Sight; 178

LR

Long Range; 48

LSTM

Long Short-Term Memory; 43

MEMS

Micro Electro-Mechanical Systems; 26

MIPS

Multiband Interferometric and Polarimetric Synthetic Aperture Radar; 102

MLE

Maximum Likelihood Estimation; 121

MR

Medium Range; 48

MTOM

Maximum Take-Off Mass; 110

NED

North-East-Down; 84

OTHR

Over-The-Horizon Radars; 50

PHAT

Phase Transform; 96

PO

Physical Optics; 52

RAM

Radar Absorbing Materials; 49

RF
Radio Frequency; 49
RFE
Radio Front-End; 150
RNN
Recurrent Neural Networks; 43
RPAS
Remote Piloted Aircraft System; 31
RX
Receive; 106
SAM
Sustainable Air Mobility; 17
SAR
Synthetic Aperture Radar; 107
SD
Standard Deviation; 115
SDR
Software Defined Radio; 132
SESAR
Single European Sky ATM Research Program; 24
SME
Small and Medium-sized Enterprises; 34
SNR
Signal-to-Noise Ratio; 18
SR
Short Range; 48
SS
Surveillance Systems; 28
SSR
Secondary Surveillance Radar; 29
ST
Stealth Technology; 49
TDOA
Time Direction Of Arrival; 96
TM
Transverse Mode; 54
TX
Transmit; 105
UAM
Urban Air Mobility; 17
UAS

Unmanned Aircraft Systems; 17

UAV

Unmanned Aircraft Vehicle; 17

UI

User Interface; 79

USS

UAS Service Supplier; 134

UTM

Unmanned Traffic Management; 22

VLO

Very Low Observable; 53

WP

Work-Packsges; 160